FAA-79-4

REPORT NO. FAA-RD-79-10

INVESTIGATION OF STABLE ATMOSPHERIC STRATIFICATION EFFECT ON THE DYNAMICS OF DESCENDING VORTEX PAIRS

A.M. Hecht, A.J. Bilanin, J.E. Hirsh,
and R.S. Snedeker

AERONAUTICAL RESEARCH ASSOCIATES OF PRINCETON, INC.
50 Washington Road, P.O. Box 2229
Princeton NJ 08540

FEBRUARY 1979
FINAL REPORT

Prepared for

U.S. DEPARTMENT OF TRANSPORTATION
FEDERAL AVIATION ADMINISTRATION
Systems Research and Development Service
Washington DC 20591

Technical Report Documentation Page

1. Report No.	2. Government Accession No.	3. Recipient's Catalog No.
FAA-RD-79-10		

4. Title and Subtitle	5. Report Date
INVESTIGATION OF STABLE ATMOSPHERIC STRATIFICATION EFFECT ON THE DYNAMICS OF DESCENDING VORTEX PAIRS	February 1979
	6. Performing Organization Code

7. Author(s)	8. Performing Organization Report No.
A.M. Hecht, A.J. Bilanin, J.E. Hirsh, and R.S. Snedeker	DOT-TSC-FAA-79-4 A.R.A.P. Report No. 372

9. Performing Organization Name and Address	10. Work Unit No. (TRAIS)
Aeronautical Research Associates of Princeton, Inc.* 50 Washington Road P.O. Box 2229 Princeton NJ 08540	FA905/R9111
	11. Contract or Grant No. DOT-TSC-1488
	13. Type of Report and Period Covered: Final Report, Dec. 1977 - Oct. 1978

12. Sponsoring Agency Name and Address	14. Sponsoring Agency Code
U.S. Department of Transportation Federal Aviation Administration Systems Research and Development Service Washington DC 20591	

15. Supplementary Notes

*Under contract to: U.S. Department of Transportation
Research and Special Programs Administration
Transportation Systems Center
Cambridge MA 02142

16. Abstract

The physics of vortex flows in stratified fluids is studied with the objective of determining the influence of stable stratification on the descent of aircraft vortex pairs. Vortex rings descending into linear and discontinuous density stratifications are investigated experimentally and simulated numerically. The computer code used for this is based on a second-order closure turbulence model of the Reynolds stress equations in axisymmetric coordinates. Verification of the code is provided by the agreement found between the measured and calculated results. The two-dimensional version of the code is then used to simulate a measured Boeing-747 vortex descending in stable stratification. The strength and tightness of the measured vortex cores have necessitated development of a new method of numerically calculating strong vortex flows. The comparison of measured with calculated descent velocity, descent distance, swirl velocity, and circulation in the vortex is in agreement. It is concluded that turbulence effects must be accounted for in the study of aircraft vortex behavior. It is found that unalleviated vortices remain strong during descent, that the vortices stop descending due to a diffuse region of countersign vorticity outboard and above the cores, and that core separation does not primarily control descent.

17. Key Words	18. Distribution Statement
Aircraft Trailing Vortices Vortex Behavior Stratified Atmosphere Vortices	DOCUMENT IS AVAILABLE TO THE PUBLIC THROUGH THE NATIONAL TECHNICAL INFORMATION SERVICE, SPRINGFIELD, VIRGINIA 22161

19. Security Classif. (of this report)	20. Security Classif. (of this page)	21. No. of Pages	22. Price
Unclassified	Unclassified	134	

Form DOT F 1700.7 (8-72) Reproduction of completed page authorized

PREFACE

The hazard posed by trailing vortex wakes of large aircraft has been of increasing concern due to its effects on flight safety and because of the economic impact of the required increase in aircraft separation during takeoff and landing. Investigations of vortex wake behavior, both experimental and analytical, are being employed to set guidelines for avoidance procedures and to determine methods of alleviation. Purely analytical methods have had difficulty achieving agreement with measured vortex behavior due to the complex flow processes, such as turbulence, occurring within and about the vortex. Since vortex descent within the atmosphere introduces the added complexity of density stratification, numerical methods must be used to obtain any hope of including the important physics of the problem.

This investigation of vortex descent has been undertaken to clarify the results of various analytical studies which have been made by numerous investigators and which have led to contradictory predictions of vortex-pair behavior in a stratified atmosphere. The calculations which are reported here are based on the solution of the mean momentum and Reynolds stress equations of turbulence based on a second-order closure model. The computer code which provodes this solution has been given the designation WAKE . To provide verification of this code for the purpose of this study, vortex rings descending in a stratified fluid are measured experimentally, and comparisons are made between results of the axisymmetric version of the code and data for the conditions of the tests.

The flight data selected for comparison and analysis are the measured vortex descent generated by a Boeing 747 in landing configuration, but in level flight. The code is run using an initial vortex rotational velocity profile which is close to the actual data. Because the initial vortex is so strong and tight,

a new method has been devised for calculating the vortex behavior based on perturbation about the initial condition.

The results to be presented here are built upon past efforts performed for several agencies which deserve mention and acknowledgment. Development of the turbulent model has been supported in large part by the Environmental Protection Agency, under Contracts 68-02-0014 and 68-02-1310. The WAKE computer code has been developed in its two-dimensional form through funding from these contracts and through support by the Defense Advanced Research Projects Agency, as monitored by the Office of Naval Research under Contract N00014-72-C-0413. The axisymmetric version has been developed primarily through efforts performed for NASA Ames on Contract NAS2-9037 and for the Nuclear Regulatory Agency under Contract AT(49-24)-0218. The influence of stratification on vortex-pair behavior has been studied with the code under contract to NASA Langley under Contract NAS1-14707.

The tank and much of the apparatus required to perform the vortex ring experiment have been fabricated under funding from the John Hopkins Applied Physics Laboratory, Contract APL-600646.

The contract monitor for this investigation is James N. Hallock. The authors gratefully acknowledge his help and that of David C. Burnham for providing sources of flight data during the data selection process of this effort.

TABLE OF CONTENTS

TABLE OF CONTENTS

LIST OF ILLUSTRATIONS

LIST OF TABLES

SYMBOLS AND ABBREVIATIONS

Nomenclature

A	core kinetic energy parameter defined by Eq. (1.3)
a	vortex-ring oval semi-major axis
b	vortex-ring oval semi-minor axis; vortex-pair core separation
D	vortex-ring diameter
E(k)	complete elliptic integral of the second kind
Fr_1	$V_o/R_o \left[g\Delta\rho/(\rho_o R_o)\right]^{\frac{1}{2}}$
Fr_2	V_o/NR_o
Fr_3	$\Gamma_o/2\pi s^2 N$
g	acceleration of gravity (9.81 m/sec^2)
J,K	maximum number of grid points in r, z directions
K(k)	complete elliptic integral of the first kind
k	argument of the elliptic integrals defined by Eq. (3.7)
ℓ_s	density discontinuity spread parameter
m,n	indices of stream function boundary condition summation, Eq. (B.4)
N	Brunt-Väisälä frequency, $\left[-\left(g/\rho_o\right) d\rho_o/dz\right]^{\frac{1}{2}}$, $\left[\left(g/T_o\right) dT_o/dz\right]^{\frac{1}{2}}$
P	impulse
q	root mean square of the turbulent kinetic energy
R	vortex-ring radius
R_s	$\left[r^2 + z^2\right]^{\frac{1}{2}}$
r	radial coordinate measured from center of vortex-pair core
r_c	spread of core vorticity
s	vortex-pair semi-separation distance

T	kinetic energy
t	time
V	vortex-ring or-pair descent velocity
w	core swirl velocity
z_{max}	maximum descent distance of vortex ring
Γ	vortex-ring or-pair circulation
ε	atmospheric dissipation rate
ζ	vorticity
η	radial coordinate measured form center of vortex ring core
Θ	mean temperature
θ	fluctuating temperature
Λ	turbulent macroscale parameter
λ	turbulent microscale parameter
ν	kinematic viscosity
ρ	density
ψ	stream function.

Superscripts

(~)	quantity normalized by r.

Subscripts

avg	average
c	countersign
max	maximum value
o	initial value
p	refers to principal vortex.

Special

<>	ensemble averaged.

Coordinate System

Cartesian Coordinates

u,v,w	velocities parallel to x,y, and z coordinates, respectively.
x,y,z	coordinates parallel to vortex pair cores, horizontal, and vertical, respectively.

Circular Cylindrical Coordinates

r,θ,z	coordinates in radial (horizontal), azimuthal, and vertical directions, respectively
u,v,w	velocities in the r,θ, and z directions, respectively.

METRIC CONVERSION FACTORS

Approximate Conversions to Metric Measures

Symbol	When You Know	Multiply by	To Find	Symbol
	LENGTH			
in	inches	2.5	centimeters	cm
ft	feet	30	centimeters	cm
yd	yards	0.9	meters	m
mi	miles	1.6	kilometers	km
	AREA			
in^2	square inches	6.5	square centimeters	cm^2
ft^2	square feet	0.09	square meters	m^2
yd^2	square yards	0.8	square meters	m^2
mi^2	square miles	2.6	square kilometers	km^2
	acres	0.4	hectares	ha
	MASS (weight)			
oz	ounces	28	grams	g
lb	pounds	0.45	kilograms	kg
	short tons (2000 lb)	0.9	tonnes	t
	VOLUME			
tsp	teaspoons	5	milliliters	ml
Tbsp	tablespoons	15	milliliters	ml
fl oz	fluid ounces	30	milliliters	ml
c	cups	0.24	liters	l
pt	pints	0.47	liters	l
qt	quarts	0.96	liters	l
gal	gallons	3.8	liters	l
ft^3	cubic feet	0.03	cubic meters	m^3
yd^3	cubic yards	0.76	cubic meters	m^3
	TEMPERATURE (exact)			
°F	Fahrenheit temperature	5/9 (after subtracting 32)	Celsius temperature	°C

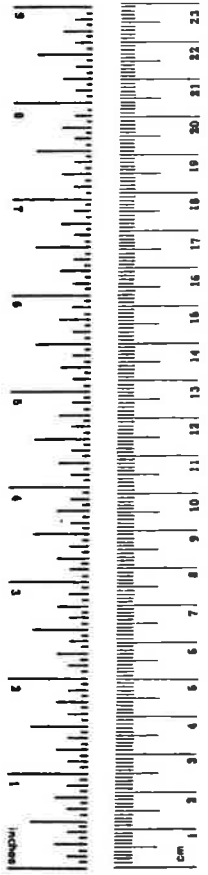

Approximate Conversions from Metric Measures

Symbol	When You Know	Multiply by	To Find	Symbol
	LENGTH			
mm	millimeters	0.04	inches	in
cm	centimeters	0.4	inches	in
m	meters	3.3	feet	ft
m	meters	1.1	yards	yd
km	kilometers	0.6	miles	mi
	AREA			
cm^2	square centimeters	0.16	square inches	in^2
m^2	square meters	1.2	square yards	yd^2
km^2	square kilometers	0.4	square miles	mi^2
ha	hectares (10,000 m^2)	2.5	acres	
	MASS (weight)			
g	grams	0.035	ounces	oz
kg	kilograms	2.2	pounds	lb
t	tonnes (1000 kg)	1.1	short tons	
	VOLUME			
ml	milliliters	0.03	fluid ounces	fl oz
l	liters	2.1	pints	pt
l	liters	1.06	quarts	qt
l	liters	0.26	gallons	gal
m^3	cubic meters	35	cubic feet	ft^3
m^3	cubic meters	1.3	cubic yards	yd^3
	TEMPERATURE (exact)			
°C	Celsius temperature	9/5 (then add 32)	Fahrenheit temperature	°F

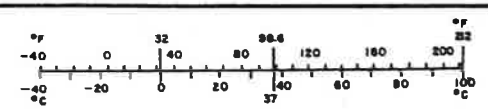

1. INTRODUCTION

1.1 VORTICES IN AN INVISCID FLUID

The hazard created by aircraft trailing vortices has generated renewed interest and research into the physics of vortex flows. In an ideal fluid without external influences, vortex pairs and vortex rings will persist indefinitely. For a ring with uniform concentrated vorticity, the speed of translation has been known for over a century. Kelvin, in 1867, gave the translation velocity for a vortex ring in an ideal fluid

$$V = \frac{\Gamma}{4\pi R}\left[\ell n\left(\frac{8R}{r_c}\right) - \frac{1}{4}\right] \quad , \tag{1.1}$$

where R is the ring radius, and r_c is the core radius within which the vorticity is uniform. The self-induced velocity of translation of vortex rings with arbitrary distribution of vorticity in the core was determined independently by three investigators only recently: Bliss, Ref. 1, Saffman, Ref. 2, and Fraenkel, Ref. 3. The velocity of translation was found to be

$$V = \frac{\Gamma}{4\pi R}\left[\ell n\left(\frac{8R}{r_c}\right) + A - \frac{1}{2}\right] \quad , \tag{1.2}$$

where A is defined by

$$A = \lim_{\eta/r_c \to \infty}\left[\int_0^{\eta/r_c} \bar{v}^2 \left(\frac{\eta}{r_c}\right) d\left(\frac{\eta}{r_c}\right)\right] - \ell n\left(\frac{\eta}{r_c}\right) , \tag{1.3}$$

and $\bar{v}$ is the swirl velocity non-dimensionalized by $\Gamma/4\pi R$, and η is a radius measured from the center of the core (see Fig. 1-1a). For the case of a core with uniform vorticity, $A = \frac{1}{4}$ for $r_c/R \ll 1$, recovering Eq. (1.1).

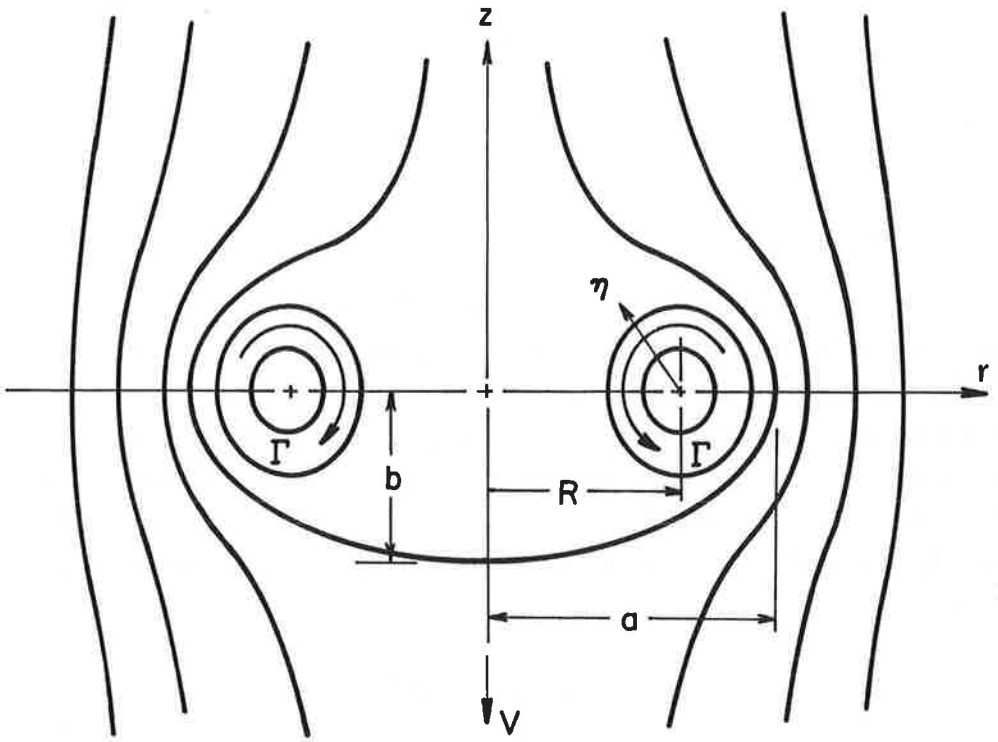

Figure 1-1a. Vortex-ring coordinates and parameters.

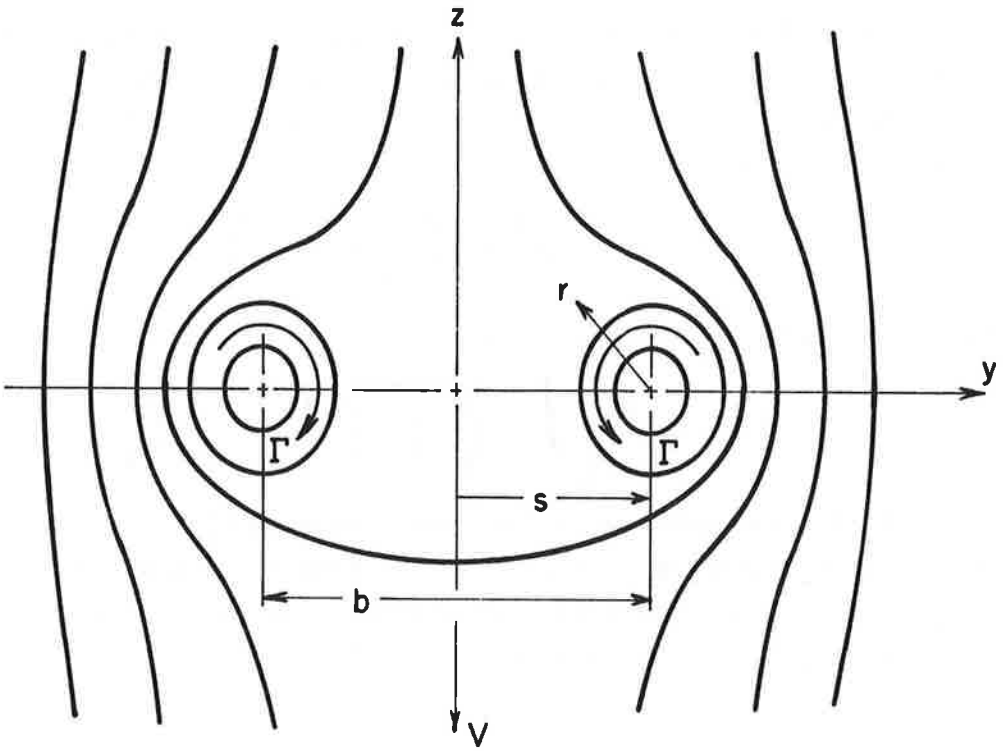

Figure 1-1b. Vortex-pair coordinates and parameters.

For a vortex pair with concentrated vorticity, the speed of translation is not critically dependent upon the distribution of vorticity within the core. For a vortex pair with concentrated vorticity in the cores with spread r_c, the velocity for core separation b is

$$V = \frac{\Gamma}{2\pi b} + \mathcal{O}(r_c/b)^2 \qquad (1.4)$$

The coordinates for a vortex pair are shown Figure (1-1b).

1.2 VORTICES IN REAL FLUIDS

1.2.1. Vortex Pairs

In the presence of buoyancy, shear, or three-dimensional instabilities, the life time of vortex pairs or vortex rings will be limited by one or more of these effects, and the velocity of translation will no longer obey Eqs. (1.2) or (1.4). In a real fluid, the action of viscosity and turbulence will restrict the distance vortices attained during descent to finite values. The study of aircraft trailing vortices must, therefore, include the influence of all of these effects, which occur, or may occur, during the descent of vortices in the real atmosphere.

The role of atmospheric stratification and buoyancy in influencing the behavior of trailing aircraft vortices has been the focus of considerable attention in the recent past. Table 1-1, adapted from Widnall, Ref. 4, presents a summarized comparison of the predicted behavior of vortex pairs in a stably stratified environment, Refs. 5-12. Appended to Widnall's comparison is the recent work of Bilanin et al., Ref. 13. There is clearly no consensus regarding vortex spacing, descent velocity, and the effect of buoyancy-generated vorticity. All investigators, except the last, disregard the effects of viscosity and tur-

TABLE 1-1. COMPARISON OF THEORETICAL MODELS FOR THE DESCENT OF A VORTEX WAKE IN A STABLY STRATIFIED ATMOSPHERE

Author (Ref.)	Vortex Spacing	Descent Speed	Buoyancy-Generated Vorticity
Costen (5)*			
Weak stability	Decreases	Increases	No effect
Strong stability	Increases	Stops	
Kuhn & Nielsen (6)	Decreases	Increases	Partly entrained
Saffman (7)	Increases	Stops	Entrained
Scorer & Davenport (8)	Decreases	Increases	Detrained
Tombach (9)			
Strong stability	Increases	Stops	Entrained
Weak stability	Decreases	Increases	Entrained
Tulin & Shwartz (10)	Increases	Stops	Entrained and annihilated
Crow (11)	Decreases	Increases	Created in wake and interface
Narain & Uberoi (12)	Decreases	Decreases	Entrained
Bilanin et al. (13)	Approx. constant	Decreases	Complex interaction

*Costen's model is a buoyant-core model; all others are buoyant-oval models

bulent transport in their analytic model although all appear to agree on the importance of these effects. There is no dispute regarding the importance of viscosity and turbulent transport in controlling the behavior of descending vortex pairs, but only in how they enter into the physics of the flow and if any proposed predictive model accounts for the physics correctly.

1.2.2 Vortex Rings

In recent years, there has been considerable effort applied to the understanding of vortex rings although much of it has not been concerned with vortex-ring behavior in a stratified fluid. Turner, Ref. 14, presented a theoretical study of the comparison between buoyant vortex rings and vortex pairs. Linden, Ref. 15, conducted experiments and proposed a theoretical model for the interaction of a vortex ring with a sharp density interface. Linden's experiments were conducted in the low Froude number regime and instead of penetrating completely into the high-density region, the rings rebounded at the density interface.

Recently, Maxworthy, Ref. 16, discussed results of stratified vortex ring experiments. The experiments were carried out in a linearly stratified environment, and the vortex-ring radii were observed to decrease with increased penetration into the stratification. Maxworthy discussed the experimental behavior within the context of a broader model of vortex ring behavior developed in Refs. 16-18. However, as noted by Maxworthy, the complex interactions occurring among the ring dynamics, buoyancy, and turbulent transport cannot be fully accounted for by a simple model. It, therefore, seems clear that we must resort to numerical calculations which contain a more complete description of these interactions.

1.3 VALIDATION OF THE PREDICTIVE MODEL

The test of any proposed model is whether it predicts the observed behavior accurately. There are full-scale data available, but little data exist which have either been taken under controlled conditions, contain the relevant measurements sufficiently to validate predictive models, or are without ground interference effects. Although laboratory experiments seem to offer the logical alternative to obtain experimental verification of theory, it is difficult if not impossible to study in the laboratory a vortex pair free of end effects (e.g., wall scrubbing) which influence their behavior.

The study of vortex dynamics in the laboratory is most easily accomplished by observing the behavior of vortex rings. This approach, therefore, offers an alternative in predictive model evaluations and in increasing our understanding of vortex behavior.

The following three sections of this report contain the results of such an experiment, and present a comparison between data and the results of calculations made with an axisymmetric stratified code. This code incorporates the effects of turbulence based upon second-order closure of the Reynolds stress equations, using an invariant model of turbulent transport (summarized by Donaldson, Ref. 19; Lewellen, Ref. 20; and Lewellen, Teske, and Donaldson, Ref. 21). The model has been incorporated into both two-dimensional and axisymmetric computer codes which have been used with considerable success in the study of a variety of stratified wake, aircraft trailing vortex, and meteorological phenomena, see Refs. 13 and 22-25. These codes are described more fully later in this report.

The vortex ring experiment and apparatus are described in Section 2. In Section 3, the axisymmetric WAKE code is described, and the vortex ring experiment initial conditions are discussed. Section 4 presents comparisons between the vortex ring data and numerical calculations. The two-dimensional WAKE code is briefly described in Section 5, the vortex pair flight data selection is

described and comparisons between numerical and flight test results are made. Conclusions are drawn and discussed in Section 6.

2. DESCRIPTION OF THE VORTEX RING EXPERIMENT

2.1 EXPERIMENTAL APPARATUS

The apparatus used to perform the vortex-ring experiments in a stratified fluid consisted of a transparent test tank, a nozzle-type vortex-ring generator, and the necessary mixture tanks, pumps, and piping required to produce a density stratified fluid. A sodium chloride/water brine solution constituted the test medium.

2.1.1 Test Tank

The tank was constructed to permit observation of the ring formation and descent and the use of quantitative flow visualization techniques. A schematic of the tank is shown in Figure 2-1. The tank had inside dimensions of 142 cm in depth and was square with sides of 61 cm. Two opposite sides and the bottom of the tank were made of plywood and covered by a white vinyl liner. The remaining sides were of 1.9 cm acrylic sheet. A combination fill-drain fitting was installed at the center of the bottom. To reduce concentrated disturbances caused by the filling process, a screen diffuser was mounted 2 cm above the bottom. Filled to within 7 cm of the top, the tank held 500 liters, or about 410 kg of fresh water.

2.1.2 Water Feed System

The system used to produce the stratified brine solution is shown schematically in Figure 2-2. As described by Oster, Ref.26, a linear gradient is produced by setting the rate of flow of the brine supply at one-half of the rate of flow of the mixture out of the mixing tank, which initially holds fresh water. The initial volume of fresh water is specified by the requirement that the mixture tank run dry at the desired fill level of the test tank. The mixture tank is fitted with paddles to insure uniform mixture concentration. Volume flow rate of brine and mixture are measured

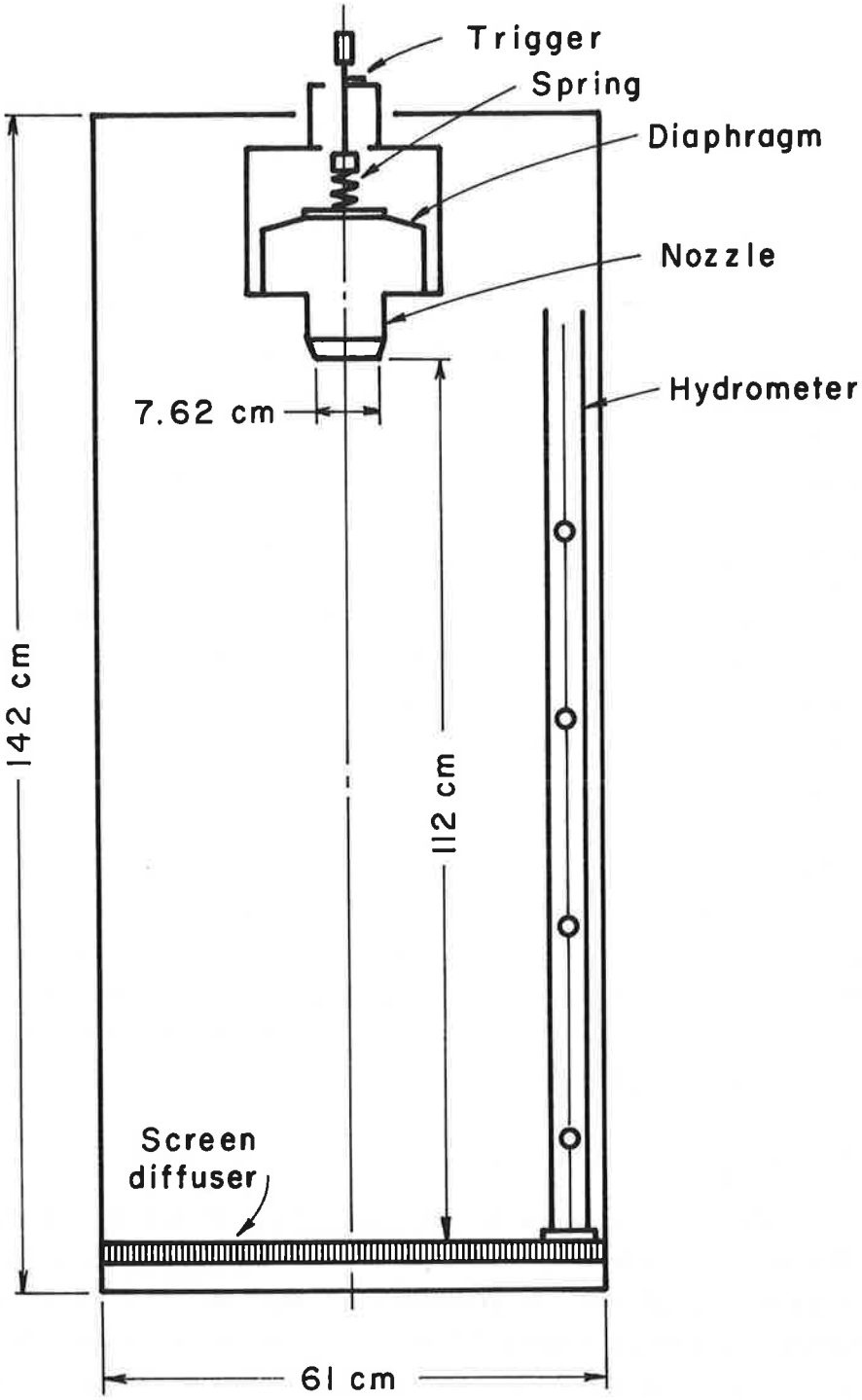

Figure 2-1. Vortex-ring experimental tank.

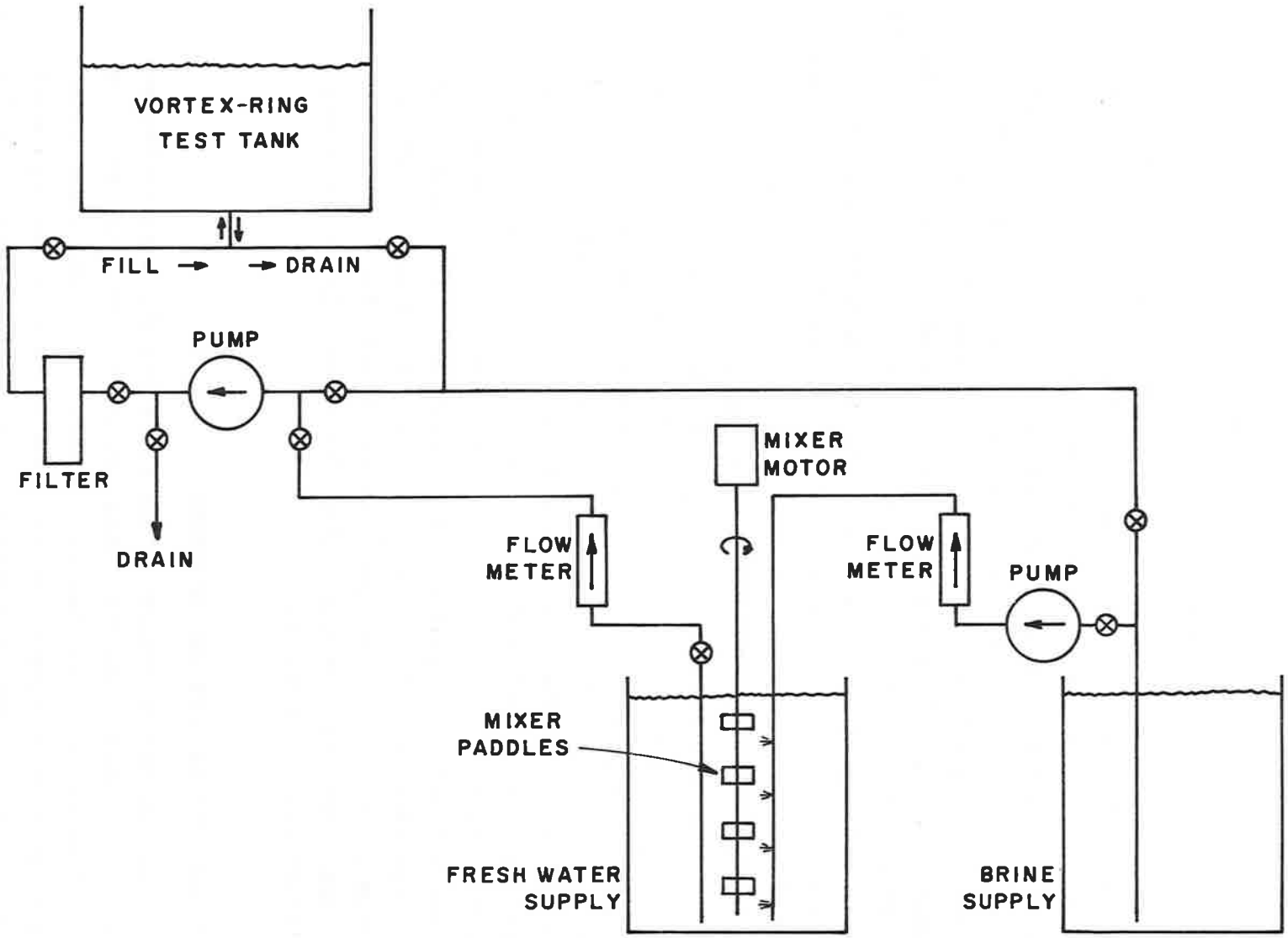

Figure 2-2. Water feed system for producing desired density stratification.

by a pair of calibrated flow meters.

2.1.3 Vortex Ring Generator

The device used to produce vortex rings is shown in cross section in Figure 2-3. Three adjustments were employed to produce a wide variety of ring starting conditions. The length of the stroke was controlled by the positions of the travel stop nut and the trigger setting (pull back) nuts. The speed of the stroke was controlled by the main spring tension and also by the trigger setting. Once a particular set of adjustments was made, the ring generator produced identical rings repeatedly. The acrylic nozzle had a diameter of 7.62 cm. Dye was injected prior to each run for flow visualization through a manifold which had 24 equally spaced holes.

By tripping the trigger, a cylindrical slug of fluid is ejected from the end of the nozzle. As the fluid emerges from the nozzle, there are two effects which influence the ultimate characteristics of the ring. First, there is the weak ring of vorticity of opposite sign which forms due to entrainment of the fluid external to the nozzle (see Maxworthy, Ref 16). Second, there is a "stopping" effect as the diaphragm of the ring maker comes to rest. It was noted during the test that there was a slight rebound which pulled a small portion of the ejected slug of fluid back into the nozzle. Neither effect was a serious problem, since rings were produced which were free of such "starting" effects within about one-half to one nozzle diameter away from the exit.

2.2 FLOW VISUALIZATION TECHNIQUE

Two methods of observing and recording the vortex-ring behavior were used. The first made use of the injected dye as a streamline tracer. In this case, a sheet of ground glass with a reference grid drawn on it was mounted outside the rear wall of the tank to serve as a diffuser. Photoflood lamps were directed at a white reflecting panel behind the ground glass so as to

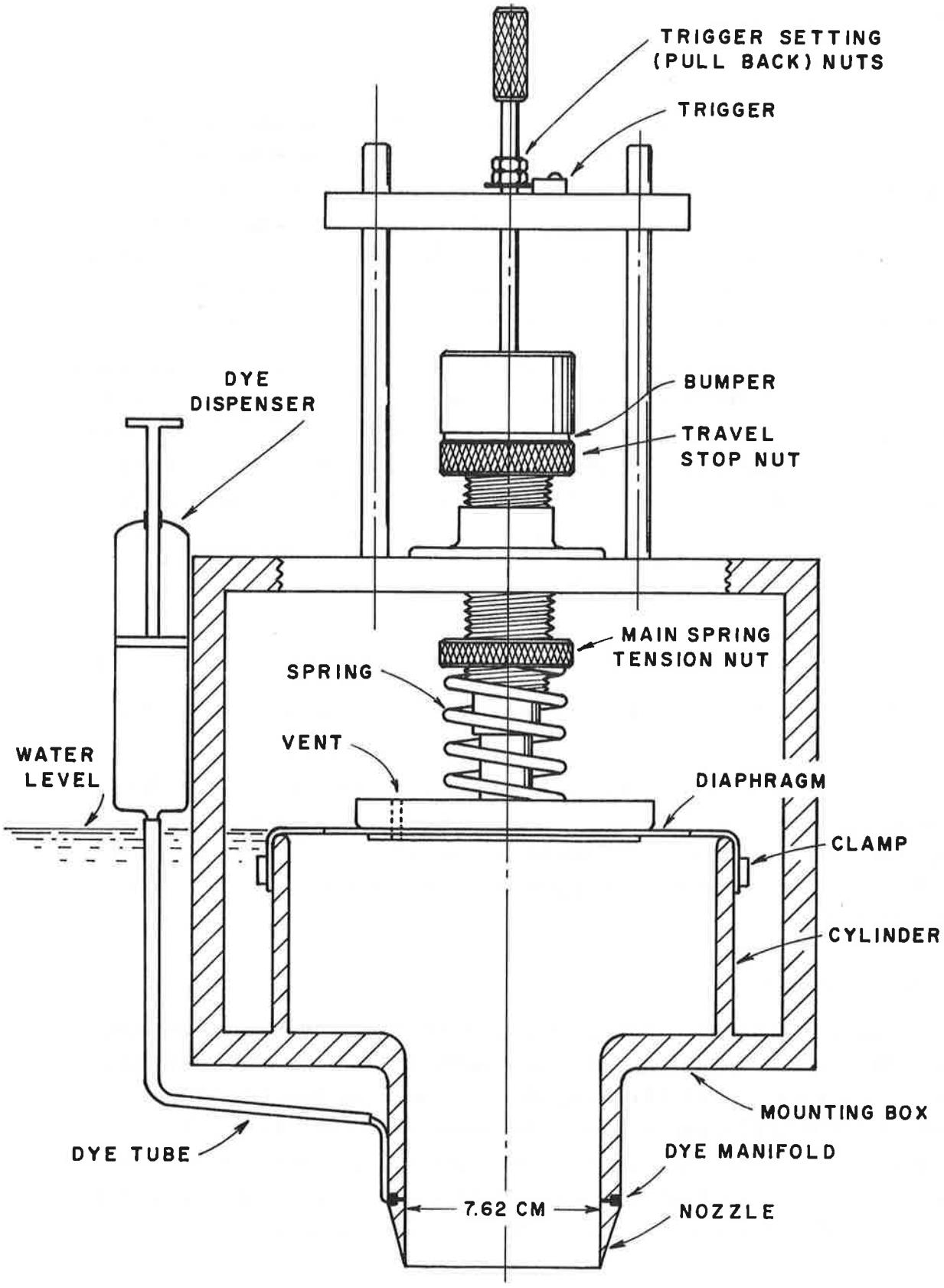

Figure 2-3. Ring generator.

achieve uniform illumination. With this illumination, the ring streamlines could be visualized against the uniform background. Since there was considerable scattering of light within the tank, all sides of the ring were also illuminated, creating an enhanced three-dimensional effect. This technique was particularly useful for observing the details of the ring structure, since the dye tended to concentrate in certain regions more than others.

A second technique which was assessed, but which was not used during the present test data reduction, was the shadowgraph technique. In this case, the ground glass was moved to the front wall of the tank and the collimated beam of light projected from the rear. Indications are that this technique would be quite useful in studying the ring flow field as it descends in the tank. Of particular interest is visualization of the turbulent structure.

2.3 PHOTOGRAPHY

The behavior of the rings was recorded by means of a Bolex® 16-mm motion picture camera. Sequences were taken in slow motion (64 frames per second).

All measurements were scaled using the nozzle orifice diameter as the reference length. The amount of refraction produced by the vertical density gradient was found to be negligible for all conditions except during passage through the sharp density discontinuity.

2.4 CALIBRATION

To determine the range of performance of the ring generator, a series of calibration runs were carried out with the tank full of fresh water. For this purpose, the main spring tension was set at four different values. For each of these values, the trigger adjustment (pull back) was also set at four values. Thus, a basic set of 16 conditions was established. For each condition, five trials were made in which the ring descent was timed from a

few cm below the nozzle to within a few cm above the tank bottom. The total ring travel during timing was 91 cm. A plot of the calibrations in terms of average descent velocity versus trigger setting for each main spring tension is given in Figure 2-4. It is seen that the velocity is approximately linear with spring tension and that a range of velocities from about 6 to 37 cm/sec could be achieved.

2.5 STRATIFICATION MEASUREMENT

For the linear gradient tests, a hydrometer consisting of a set of balls of known specific gravity, in an open triangular cage, was used inside the tank to assess the accuracy of the density gradient produced. As shown in Figure 2-5, the stratification achieved was very nearly linear.

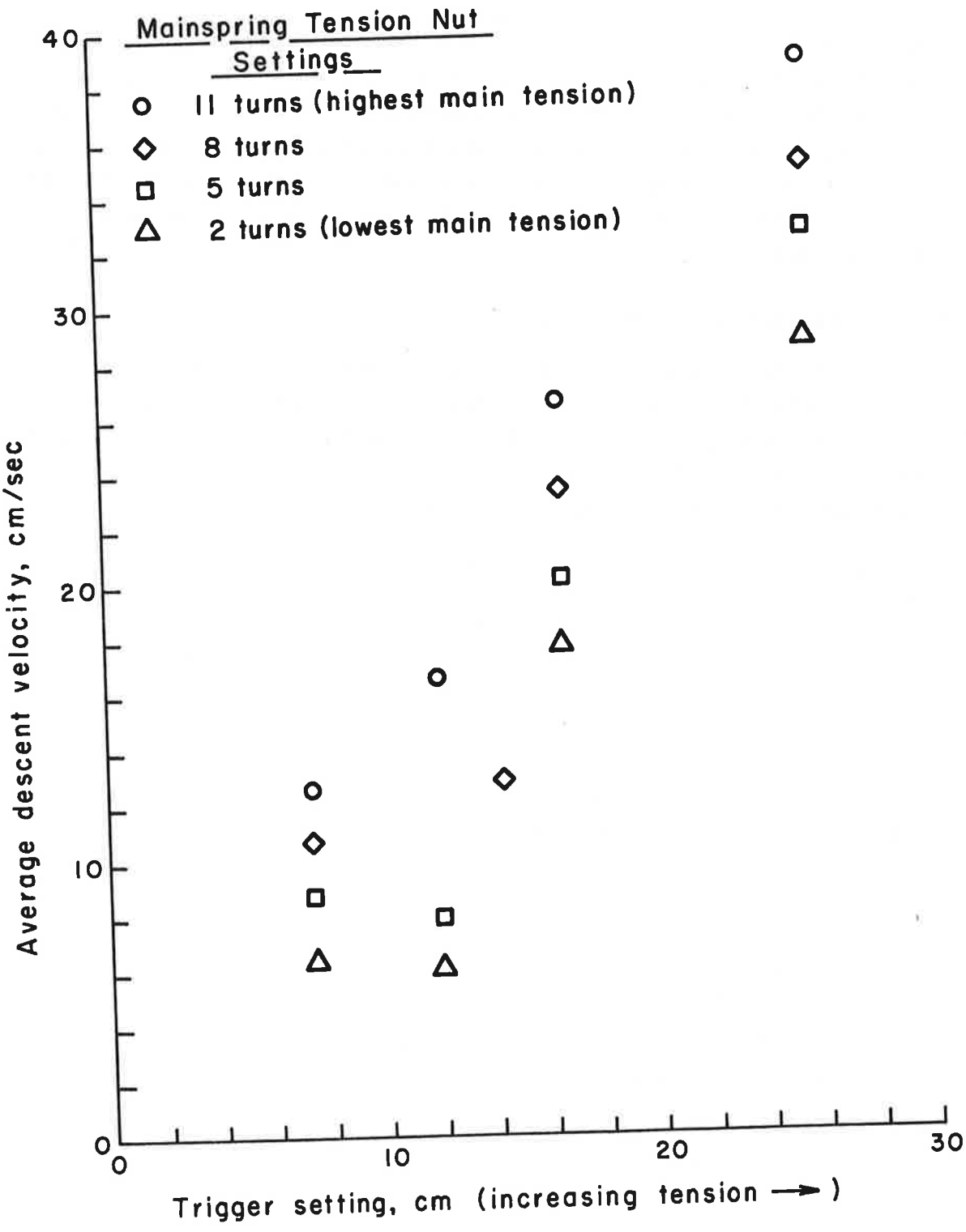

Figure 2-4. Calibration of ring generator.

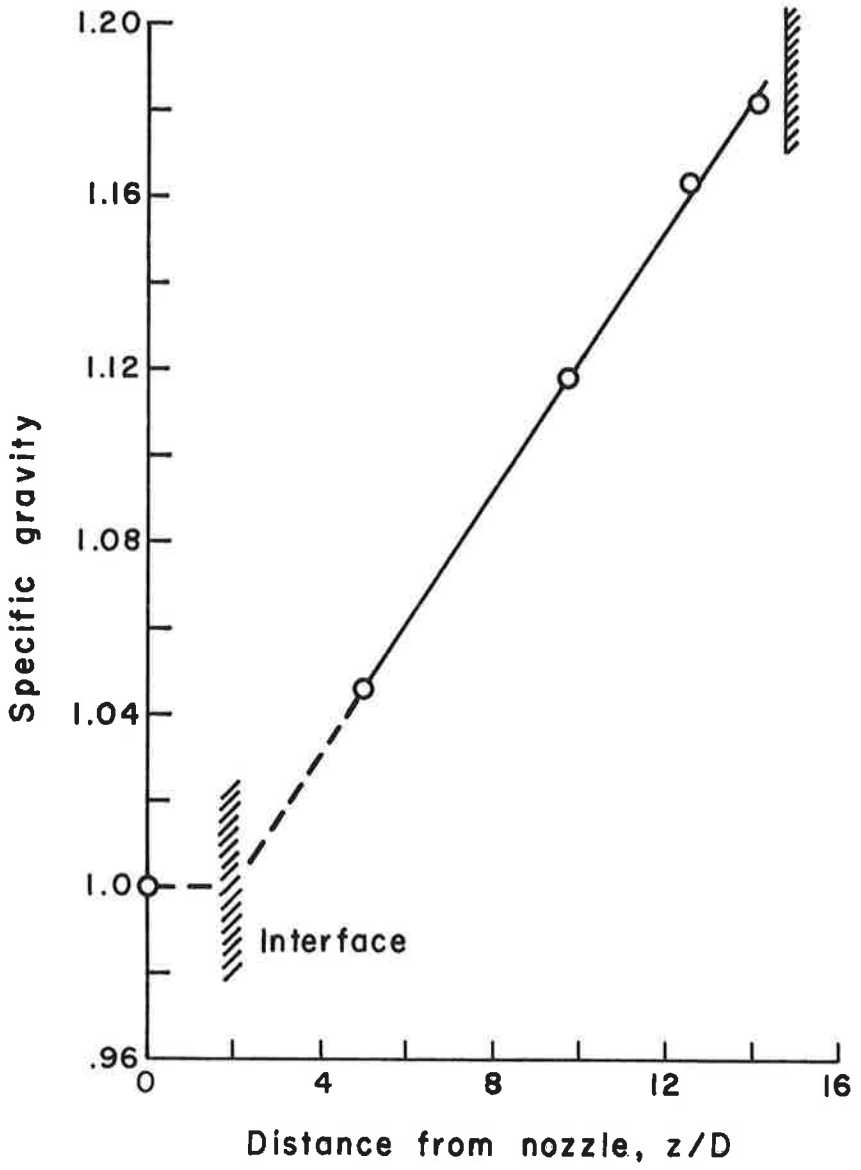

Figure 2-5. Measured stratified density (o Measurement; — nominal linear gradient).

3. VORTEX-RING NUMERICAL CALCULATION TECHNIQUE

3.1 DESCRIPTION OF THE AXISYMMETRIC WAKE CODE

The equations governing the mean variables and the turbulent second-order correlations, in modeled form, and based on the Boussinesq approximation, are given in Appendix A (in an axisymmetric coordinate system). A derivation of the Reynolds equations for the second-order turbulent correlations and a discussion of the model development and constant evaluation may be found in Ref. 20. The equations are finite differenced on a nonuniformly spaced grid and, with the exception of the equation governing the mean density, solved using a modified alternating-direction-implicit scheme. The mean density is solved for using a flux-corrected transport technique developed by Boris and Book, Ref. 26. This is done to improve resolution of the sharp density gradient between the descending oval and the ambient fluid. This gradient increases with time as the ring penetrates progressively farther into the stratified environment.

The Poisson equation governing the stream function from which the velocities are obtained is evaluated using a fast elliptic solver developed by Swartztrauber and Sweet, Ref. 28. A J6 representation of the convective operator (Arakawa, Ref. 29), in which the conservative and nonconservative operators are averaged, is used to improve simulation of the convective nature of the vortex-flow problem.

To keep the vortex ring inthe computational domain, an upwash velocity is added. Tracking the centroid of the square of the vorticity is a technique which centers the ring in the domain until the very final stages of the total descent.

The computations were initialized by positioning a Gaussian of vorticity of the form ,

$$\frac{\zeta_o R_o}{V_o} = \left(\frac{\zeta_{o_{max}} R_o}{V_o}\right) \exp\left[-(\eta/R_o)^2/(r_c/R_o)^2\right], \qquad (3.1)$$

in the azimuthal plane at a point r_o/R_o and z_o/R_o , which normally would be at 1.0 and 0.0, respectively. However, $r_o/R_o = 0.95$ was used here for reasons which will be described later. The coordinate η is measured radially outward from the vortex core center, and r_c is the vortex spread. An isotropic Gaussian spot of turbulence was positioned in the center of the vortex core with strength $q_o^2/V_o^2 = 0.01$ such that

$$\langle uu\rangle = \langle vv\rangle = \langle ww\rangle = (q_o^2/3)\exp\left[-(\eta/R_o)^2/(r_c/R_o)^2\right]. \qquad (3.2)$$

The initial conditions are shown schematically in Figure 3-1.

At the edges of the computational domain, except at $r = 0$, the stream function is evaluated by a moment expansion of the Biot-Savart law as described in Appendix B. At the inflow boundary at z_- , the density is convected in at the appropriate value for the type of stratification considered and the descent which has occurred. For a linear stratification, the density is non-dimensionalized by the product of the background gradient and R_o , so that $\partial\rho/\partial z = -1$ in non-dimensional form. For the case of the sharp density discontinuity, the total non-dimensional density difference across the discontinuity is taken as unity, with a parameter ℓ_s used to specify the vertical spread of the density interface. The full expression used for the nondimensional density is

$$\rho = -0.5\,\frac{|z|}{z}\,\mathrm{erf}(|z|/\ell_s) \qquad (3.3)$$

It was found that $\ell_s = 0.6$ provided a density profile which was satisfactory in simulating the actual thickness of the density interface in the experiment.

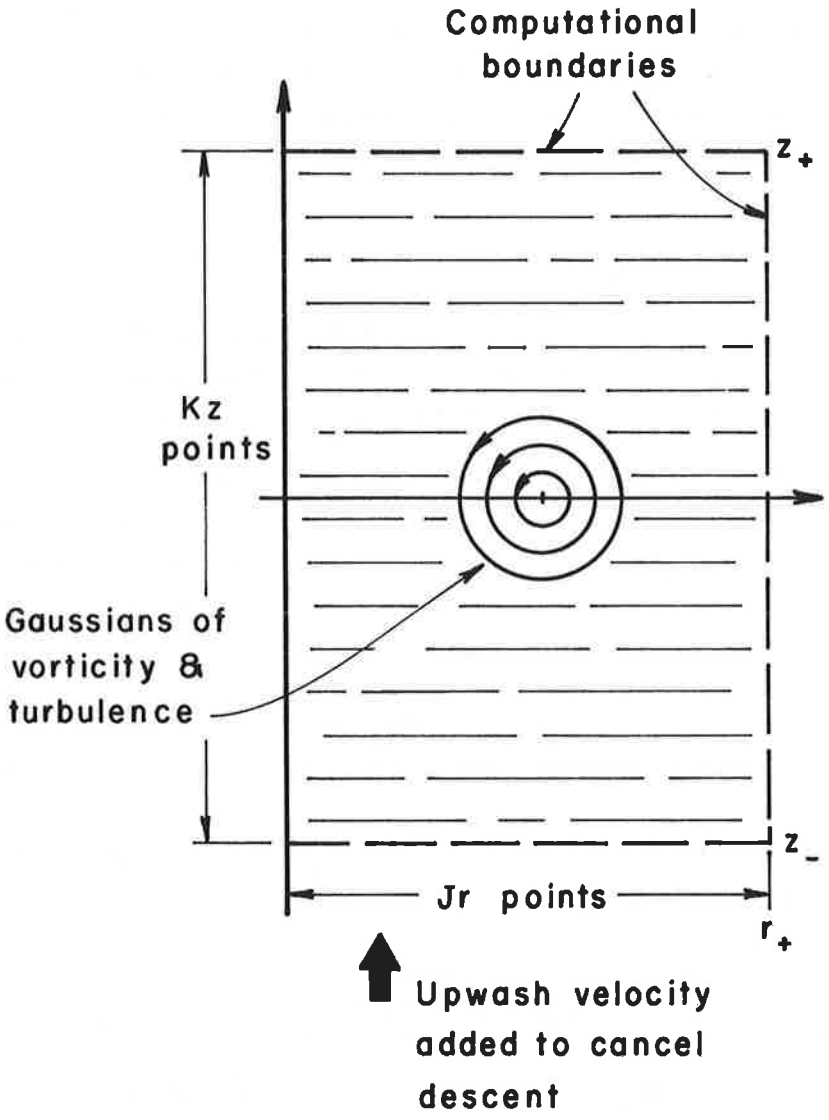

Figure 3-1. Axisymmetric stratified code initial conditions.

At the outflow boundary at z_+, an advection condition was used to sweep the flow through the boundary. The turbulence and vorticity inflow values were set equal to zero. Because of the relatively high upwash velocity, no wave interaction problems were encountered at the r_+ boundary since they were advected out of the domain before they could reflect back into the computation.

3.2 INITIAL VORTICITY PROFILE

Because it was not possible to resolve the swirl velocity in and around the core, another method was devised to obtain the appropriate initial maximum vorticity $\zeta_{o_{max}}$ and spread r_c. This was done by utilizing the measurement of the oval semi-axis a as follows. The descent velocity V of a vortex ring with arbitrary distribution of vorticity in the core is given by Eq. (1.2). For a Gaussian distribution of vorticity, $A = -0.058$ (Saffman, Ref 2). Now,

$$\frac{\zeta_{o_{max}} R_o}{V_o} = \frac{\Gamma R_o}{\pi r_c^2 V_o} \tag{3.4}$$

for a Gaussian distribution so that the descent velocity non-dimensionalized by V_o is

$$\frac{V}{V_o} = \frac{1}{4}\left(\frac{r_c}{R_o}\right)^2\left(\frac{R_o}{R}\right)\left(\frac{\zeta_{max} R_o}{V_o}\right)\left[\ell n\ \frac{8R}{r_c} - 0.558\right] . \tag{3.5}$$

At $tV_o/R_o = 0.$, $V/V_o = 1.$, $R/R_o = 1.$, so that if r_c/R_o can be defined, we can obtain $\zeta_{o_{max}}$.

The semi-axes a and b are defined by the separation streamline $\psi(a,0) = 0$ and $\psi(0,b) = 0$, respectively, of a vortex ring in steady coordinates. For a circular ring of concentrated vorticity,

$$\psi(r,z) = \frac{\Gamma(Rr)^{\frac{1}{2}}}{2\pi}\left[\left(\frac{2}{k} - k\right) K(k) - \left(\frac{2}{k}\right) E(k)\right] - \frac{1}{2}Vr^2 , \quad (3.6)$$

where $K(k)$ and $E(k)$ are the complete elliptic integrals of the first and second kinds, and where V is given by Eq. (1.2) with $A = 1/4$. k is defined by

$$k^2 = \frac{4Rr}{z^2 + (R + r)^2} . \quad (3.7)$$

Evaluation of Eq. (3.6) for $\psi = 0$ at $(a,0)$ and $(0,b)$ as a function of r_c yields a and b as shown in Figure 3-2. Both are rather weak functions of r_c/R_o. $\zeta_{o_{max}}$, evaluated using Eq. (3.5) for $V/V_o = 1$ is, however, a strong function of r_c/R_o for $r_c/R_o < 0.3$, Figure 3-3. Also shown is the value of $R_o\zeta_{o_{max}}/V_o$ vs. r_c/R_o for a concentrated core of constant vorticity.

Using the experimentally determined values of a/R_o and b/R_o as a guide provided the means of determining the core spread r_c/R_o. This, with the requirement that $V/V_o = 1.0$ initially, gave the maximum vorticity.

As noted earlier, the vortex rings were initialized at $r/R_o = 0.95$, $z/R_o = 0$. This was done to provide closer agreement with the experimentally observed initial radii of most of the runs; there was apparently still some vorticity rollup occurring at the selected initial stations.

The second-order turbulent closure model contained a dynamic equation for the scale Λ. The calculations presented here were made for a constant scale length, and therefore, the scale equation was not employed. A parametric study was carried out for a range of values of Λ/R_o between 0.03 and 0.3. It was found that $\Lambda/R_o = 0.03$ gave closest agreement with data and this value for the scale was used throughout the calculations to be presented here.

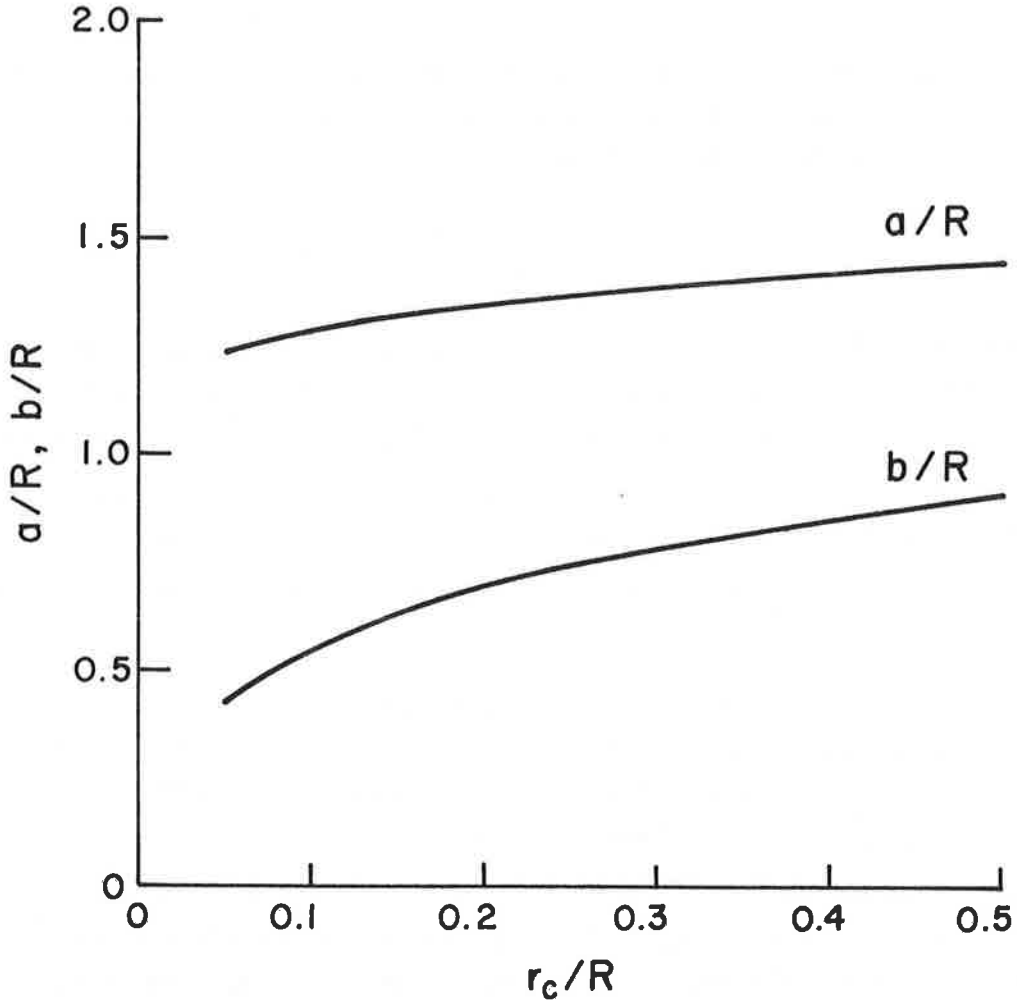

Figure 3-2. Vortex-ring oval major and minor semi-axes versus core spread for constant vorticity core.

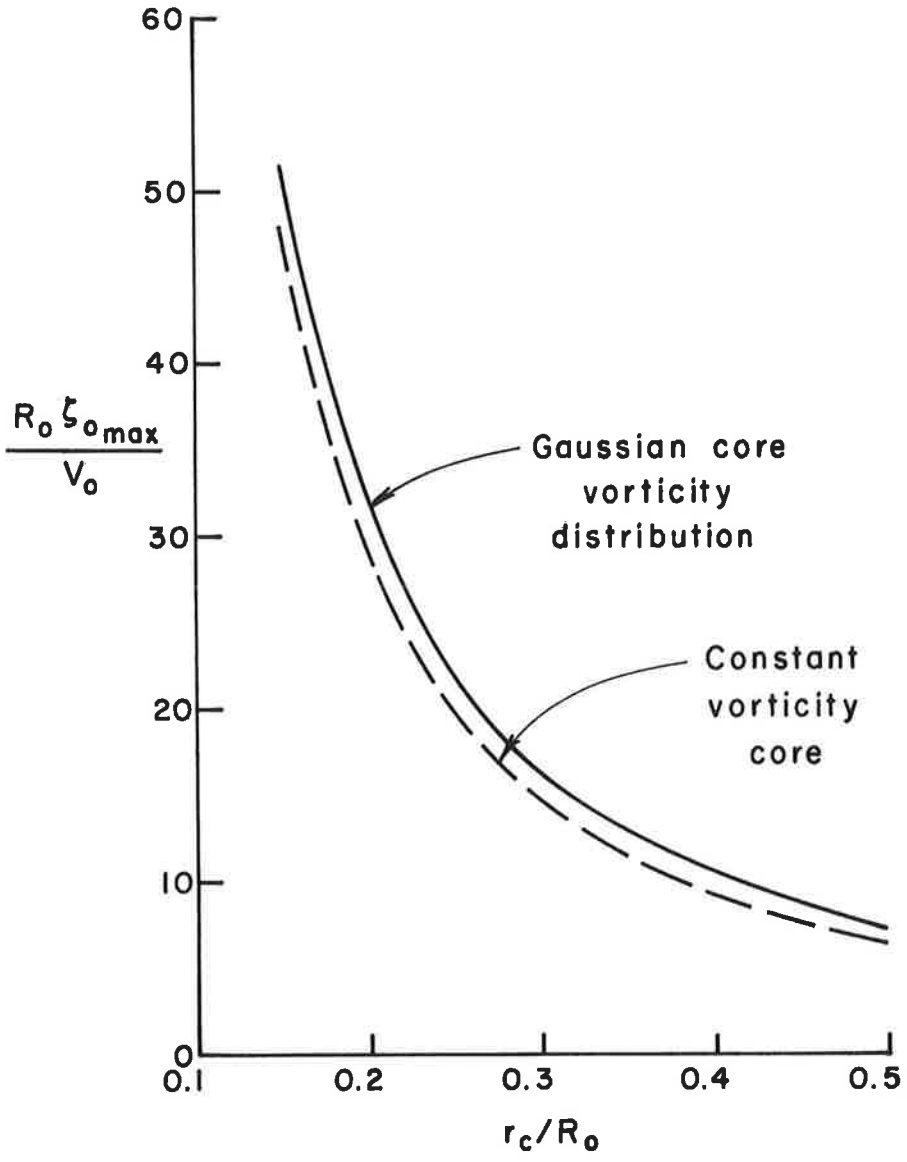

Figure 3-3. Maximum core vorticity versus core spread.

4. COMPARISON OF NUMERICAL RESULTS WITH VORTEX-RING EXPERIMENTAL DATA

4.1 DESCRIPTION OF DATA

Those experimental cases selected for analysis are listed in Table 4-1. Also shown are the core spread and maximum vorticity used in initializing the WAKE code calculations. Case 1 was a non-stratified baseline run; cases 2 and 3 were rings of fresh water of specific gravity 1.0 injected into a brine mixture of specific gravity 1.19. The density discontinuity was located approximately three ring diameters below the nozzle exit. Cases 4 through 6 were conducted in a linearly stratified density fluid. The nozzle was immersed in fresh water, and the linear stratification started at approximately two nozzle diameters below the nozzle exit. This was done to insure that the rings consisted of a known density since some mixing was inevitable during and shortly after each run. The location of the hydrometer balls was noted before, during, and after the test, and showed that vertical mixing during the tests was negligible. The rings were visible continuously during the linearly stratified tests, but the highly refractive interface between fresh water and brine in the density discontinuity tests obscured the ring during its passage through the interface, preventing measurements of ring geometry during this portion of the test.

The vortex-ring vertical descent z, diameter D, and the major and minor semi-axes (a and b, respectively) of the oval of fluid carried along by the ring during its descent were measured from projections of the movie film. It was not possible to observe the core structure or velocity with this method. The vertical descent and ring diameter were relatively easy to measure during the initial portion of each run, but measurement of ring diameter became progressively more difficult during the latter portion of descent. During approximately the last half of each run, the diameter could not be measured due to turbulent detrainment of dye. The oval size was difficult to measure. The oval

TABLE 4-1. VORTEX-RING EXPERIMENTAL AND NUMERICAL PARAMETERS

Case	Stratification	Fr_n	V_o (cm/sec)	R_o (cm)	$z_{max}-z_o$ (cm)	z_o (cm)	$\frac{V_o R_o}{\nu} \times 10^{-4}$	r_c/R_o	$\frac{\zeta_{o_{max}} R_o}{V_o}$
1	nonstratified	∞	40.39	4.55	99.3	12.7	1.81	0.25	22.0
2	discontinuity ($\Delta\rho/\rho_o$ = 1.19)	1.27	35.05	4.06	35.5	14.5	1.41	0.25	22.0
3		1.36	39.15	4.45	~46.7	17.3	1.72	0.25	22.0
4	linear	5.18	23.55	3.23	61.0	12.7	0.75	0.40	10.5
5	↓	6.17	33.15	3.81	73.5	12.7	1.25	0.30	16.3
6		6.57	38.1	4.11	86.3	12.7	1.55	0.30	16.3

n - Froude number for discontinuous stratification defined by Eq.(4.1); for linear stratification by Eq.(4.2).

was measured by assuming that the dye carried along with the ring defined the oval boundaries. This was probably not true in the initial portion of each run, but diffusion of dye during descent appeared to fill the oval sufficiently to provide a meaningful measurement, at least in the middle portion of each test. In the tests carried out with the sharp density discontinuity, refraction of light at the cell boundary after ring penetration of the heavier density fluid provided a very good oval definition in these cases for some time after penetration although the minor axis b was still not as well defined as the major axis.

The Froude number* defined for the density discontinuity and for the linear gradient cases (and given in Table 4-1) differ. For the discontinuity

$$Fr_1 = \frac{V_o}{\left[\frac{g\Delta\rho}{\rho_o R_o}\right]^{1/2} R_o} , \qquad (4.1)$$

where $\Delta\rho/\rho_o = 0.19$ and R_o is the initial ring radius before reaching the discontinuity. For the linear density gradient

$$Fr_2 = \frac{V_o}{NR_o} , \qquad (4.2)$$

where

$$N = \left[-\frac{g}{\rho_o}\frac{d\rho}{dz}\right]^{\frac{1}{2}} \qquad (4.3)$$

is the Brunt-Väisälä frequency, equal to 1.41 rad/sec for the present tests.

Shown in Table 4-1 is the maximum depth of penetration of the rings, $(z_{max}-z_o)$, measured to the center of the cell. z_o is an arbitrarily selected initial point during descent.

*Since three definitions of Froude number have, through necessity, been used in this report, they will be distinguished by the subscripts 1, 2, and 3.

The cell size for the non-stratified cases did not change appreciably during descent, and the ring reached the bottom of the test tank. In the stratified cases, the oval size decreased appreciably, and in all stratified cases, the rings dispersed before reaching the bottom of the tank.

Of particular note was the structure of the ring during descent, which initally appeared very ordered, but which eventually broke down due to an instability which has been observed many times in experimental investigations of this type. See, for instance, Widnall, Ref. 4, for a discussion of this phenomenon. The swirl around the core, which could be seen quite clearly during the initial stages by observing the entrained dye traces, became impossible to see at the latter stages of descent although the core region was still visible. Finally, the structure was completely obscured by refraction produced by the highly turbulent flow of mixed fluid throughout the oval. No core region could be seen at that point, and the ring finally was destroyed in a catastrophic process as described by Maxworthy, Ref. 16.

4.2 COMPARISON OF DATA AND NUMERICAL RESULTS

The comparison of experimental data with the numerical results of the stratified axisymmetric code are included in Figures 4-1 through 4-13. The non-stratified results are also shown in Figures 4-1 and 4-2. Both theory and experiment reveal no dramatic behavior for the non-stratified case and the ring is seen to propagate at nearly constant velocity, Figure 4-1, while increasing in radius only slightly, Figure 4-2. The horizontal oval axis is predicted well, but during the initial portion of the run, the simulation appears poor for the vertical extent of the oval. This is probably because the dye has not yet had time to diffuse through the oval as mentioned previously. Note that the values of a/R_o and b/R_o obtained from the constant core vorticity assumption are plotted as a dashed line in Figure 4.2 for the vorticity spread used in the run.

Figures 4-3a and 4-3b present the calculated stream function for the non-stratified case for non-dimensional times of 2.0 and 10.0. These plots illustrate that little if any change is pre-

dicted in the oval volume for the non-stratified case. This type of plot will be presented later for the stratified cases, where a very noticeable decrease in oval size will be shown. Note that the abscissa in these figures indicates the vertical position measured from the initial position z_o .

The measured and calculated trajectory for the case 3 density discontinuity ring injection is given in Figure 4-4, and the radius and oval parameter histories are shown in Figure 4-5. Again shown in the figures are the values of a/R_o and b/R_o for the value of r_c/R_o used for the calculation. In this case, the measured initial value of a/R_o was misleading since a vorticity spread based on it gave a poor simulation and the case was rerun using the value given in Table 4-1. The discrepancy may again be due to the failure of the dye to define adequately the oval boundary.

Figures 4-6 and 4-7 are the calculated stream function and density isopleths for case 3. At $tV_o/R_o = 2.0$, the ring is approaching the density discontinuity, while at $tV_o/R_o = 6$, it has fully penetrated. The decrease in oval size in this case is quite evident. Note the intensity of the density gradient between the fluid within the oval and the ambient fluid. It is also interesting that there is little predicted difference between the density levels and the shape of their isopleths in the vicinity of the core. The suppression of turbulence in the core region, as a consequence of the high stability of the vortex flow, prevents mixing of the core fluid with entrained ambient fluid in the outer region of the oval.

The linear stratification comparisons are given in Figures 4-8 through 4-13. The ring trajectories for cases 4, 5, and 6 are shown in Figures 4-8, 4-9, and 4-10, respectively. The numerical simulations for these cases are excellent over most of the descent, with the possible exception of the lowest injection velocity, Figure 4-8. It was noted during the tests that, for injection velocities even lower than those analyzed, the rings were not completely formed at initial penetration into the stratification and tended to tilt progressively from the vertical.

The prediction of ring radius and oval parameter history also gives excellent agreement over the measurable portion of descent, Figures 4-11 through 4-13. The poor agreement for b/R_o is again evident in the initial portion of the run.

Figures 4-14a through 4-14d present the calculated stream function for the linear stratification with Froude number 6.57, case 6. Here, the decrease in oval size is very striking at the point where the descent has almost stopped.

Figures 4-15 and 4-16 are plots of the ring radii versus time. Figure 4-15 gives the measured non-dimensional radius for cases 2 and 3, which are ring injections into a density discontinuity. Over the range of time in which the radius could be measured after passing the discontinuity, the radius history exhibits a t^{-1} dependence. Figure 4-16 compares the numerical results of the WAKE code for both the discontinuity and linear stratification. The calculated result for the discontinuity is very close to a t^{-1} dependence. For a linear stratification, the radius decrease approaches a t^{-2} dependence. It was not possible to verify this behavior during the experiment since the radius could not be measured during the latter stages of descent.

Figure 4-17 is a plot of the non-dimensional impluse $P/\rho_o R_o^2$, kinetic energy $T/\rho_o V_o^2 R_o^3$, and circulation $\Gamma/R_o V_o$ for case 6, a linear stratification run. The kinetic energy does not appear to exhibit any particular functional dependence on time, but over the middle portion of the calculation, the impulse behaves as t^{-2} and the circulation as $t^{-\frac{1}{2}}$. These calculations are based on integrations over the entire numerical grid however, and therefore the plotted results include the contribution of the countersign vorticity generated at the oval boundary. It is noted that Saffman, Ref. 7, has shown that the concept of impulse in a stratified fluid is not generally useful unless this countersign vorticity is included and the Boussinesq approximation is made. Both criteria are met here.

The objective of the experimental and numerical simulation comparison reported in this section was to provide verification of the A.R.A.P. second-order closure turbulent model. The agreement between the numerical results based on the model and the experimental data has provided this verification.

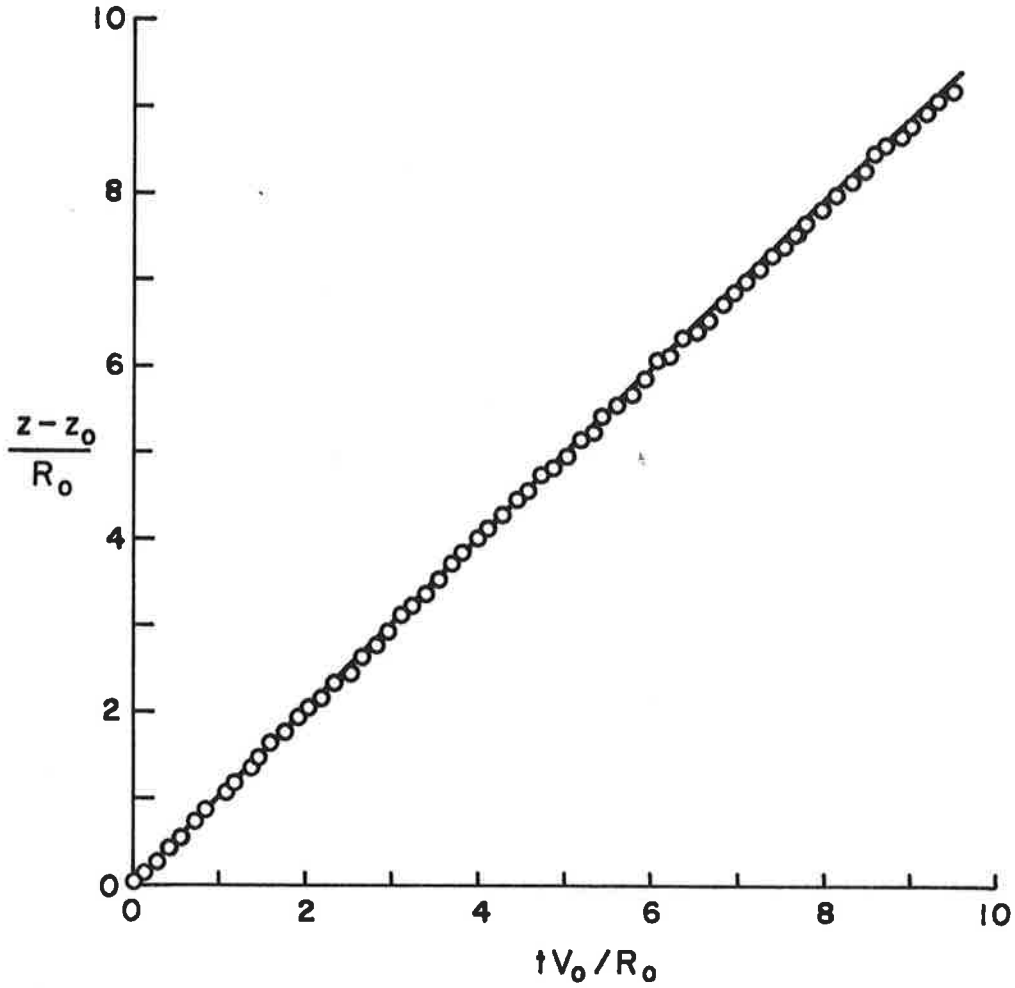

Figure 4-1. Vortex-ring trajectory for non-stratified fluid, case 1. ⊙ Data; —axisymmetric wake code calculation.

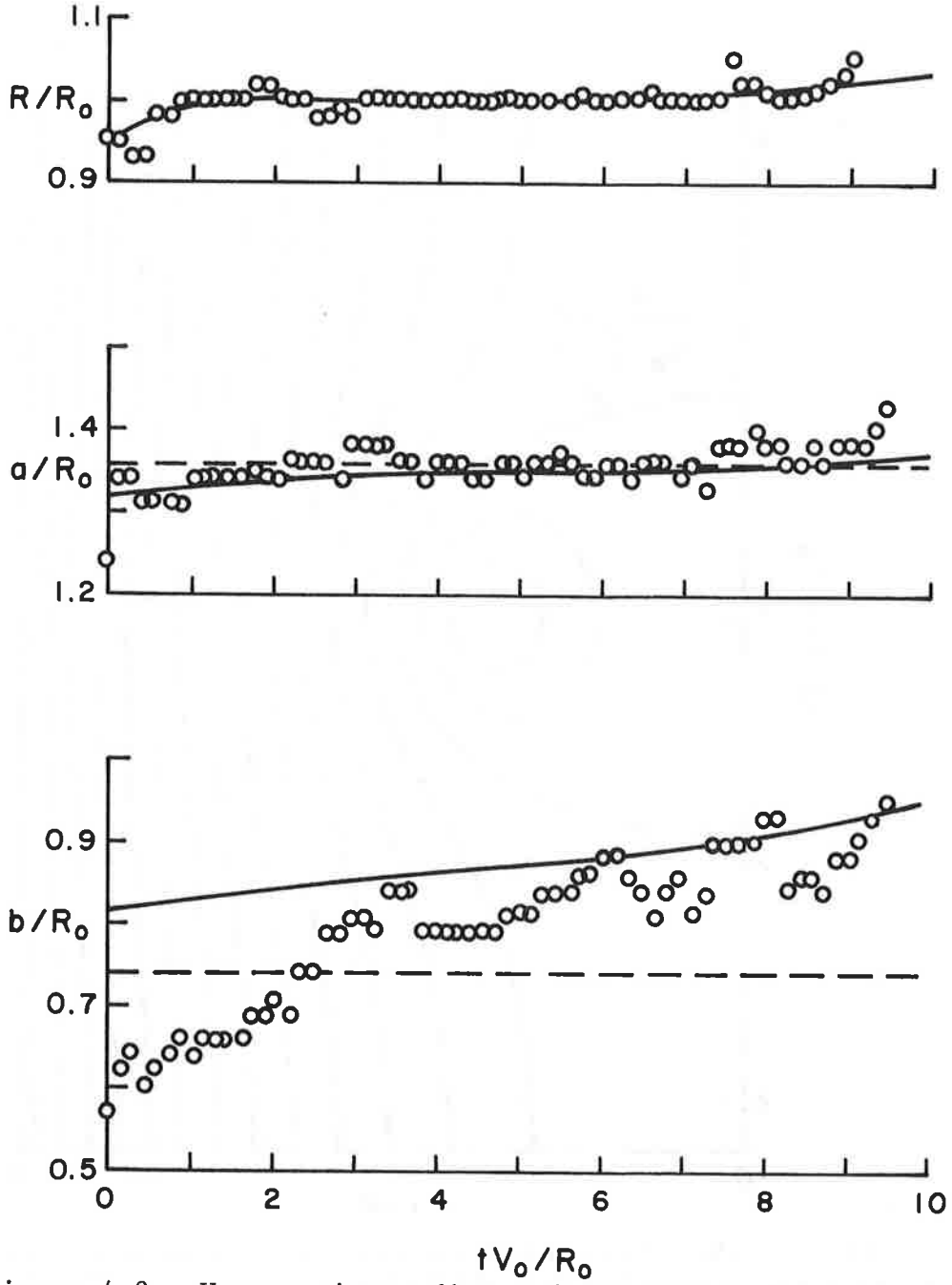

Figure 4-2. Vortex-ring radius and semi-major and semi-minor oval axes for non-stratified fluid, case 1. o Data; — axisymmetric WAKE code calculation; — — — constant core vorticity value.

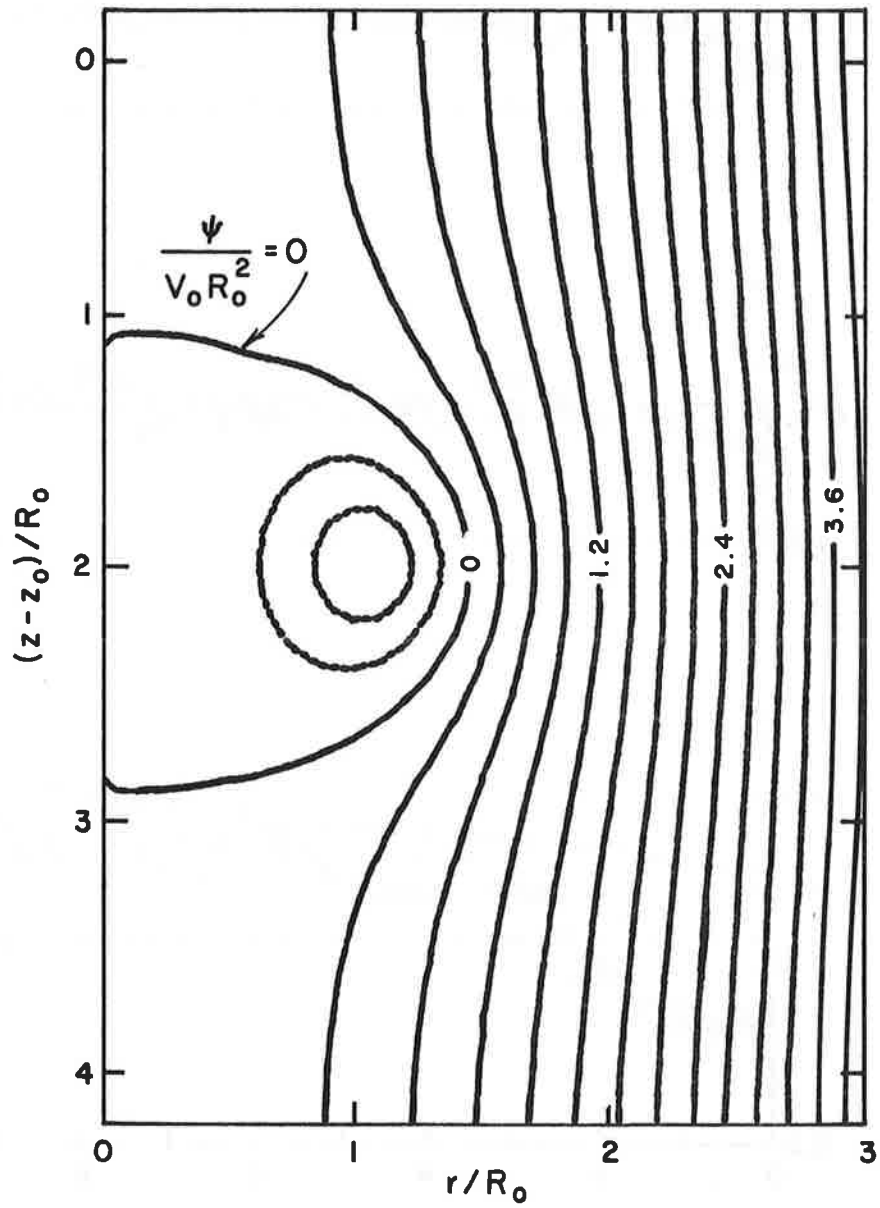

Figure 4-3a. Stream function for a descending vortex ring in a non-stratified fluid, case 1. $(z-z_o) = 2.0$ at $tV_o/R_o = 2.0$. Stream function contours from $\psi = -0.6$ to $+3.9$ at intervals of 0.3

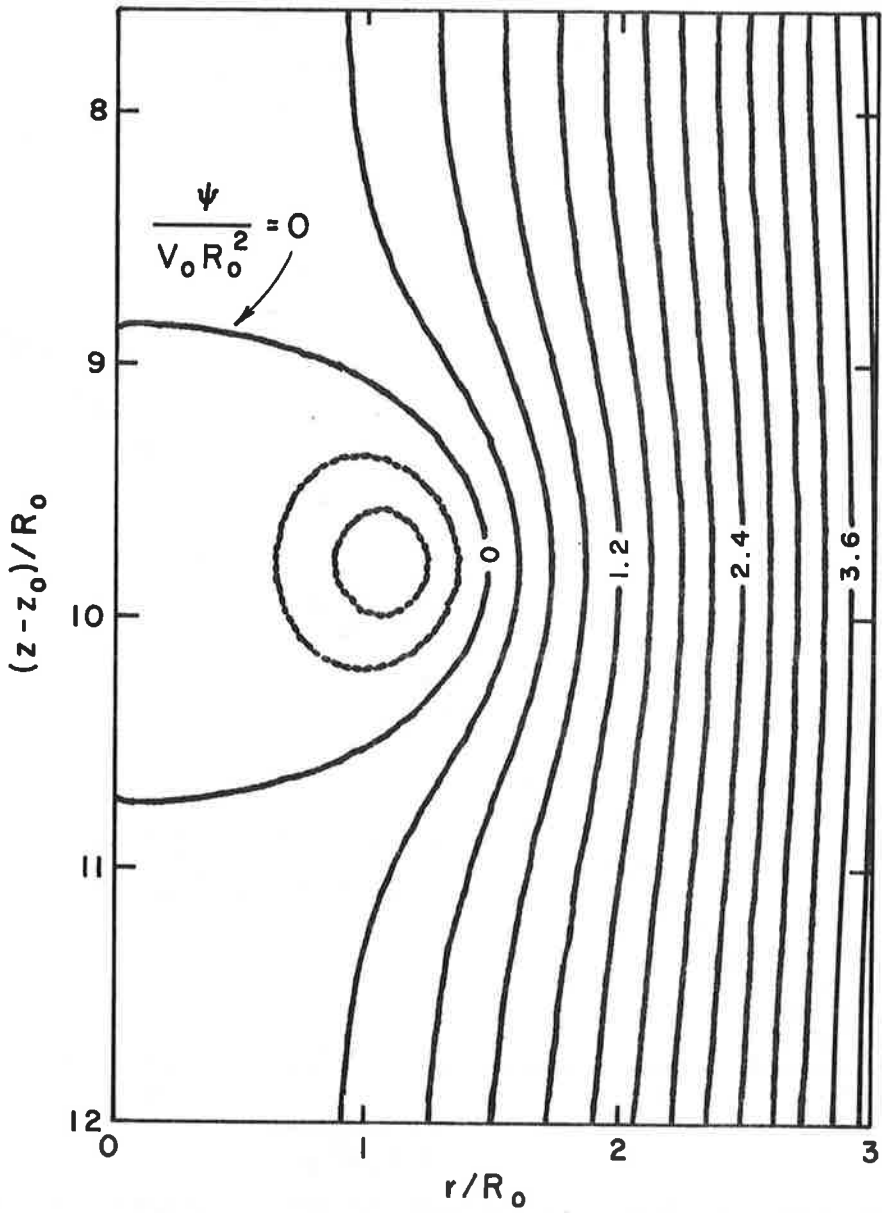

Figure 4-3b. Stream function for case 1 at $tV_oR_o = 10.0$. $(z-z_o)/R_o = 9.8$. Stream function contours from $\psi = -0.6$ to 3.9 at intervals of 0.3.

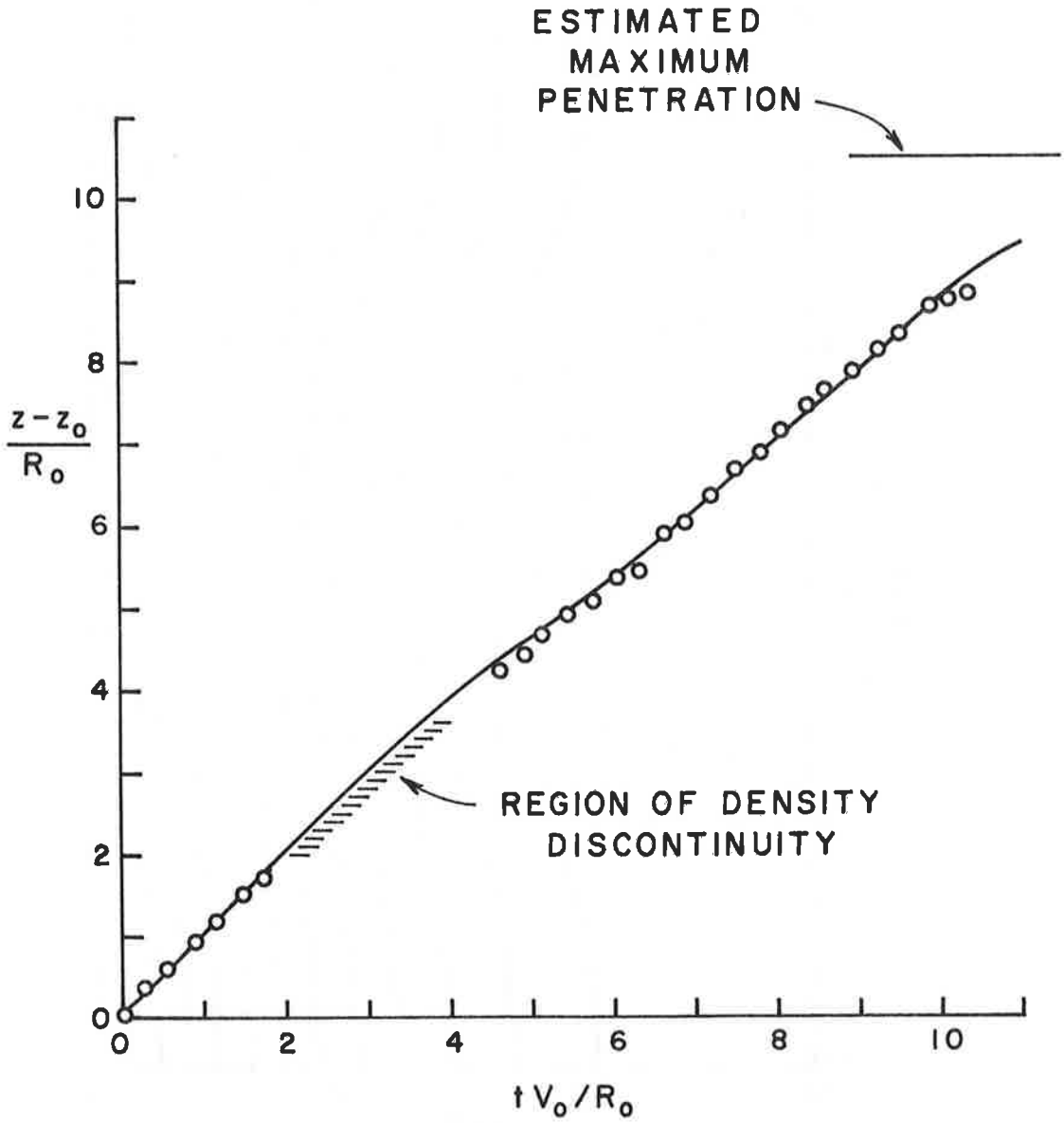

Figure 4-4. Vortex-ring trajectory for penetration of density discontinuity, case 3. ⊙ Data; — axisymmetric stratified WAKE code calculation.

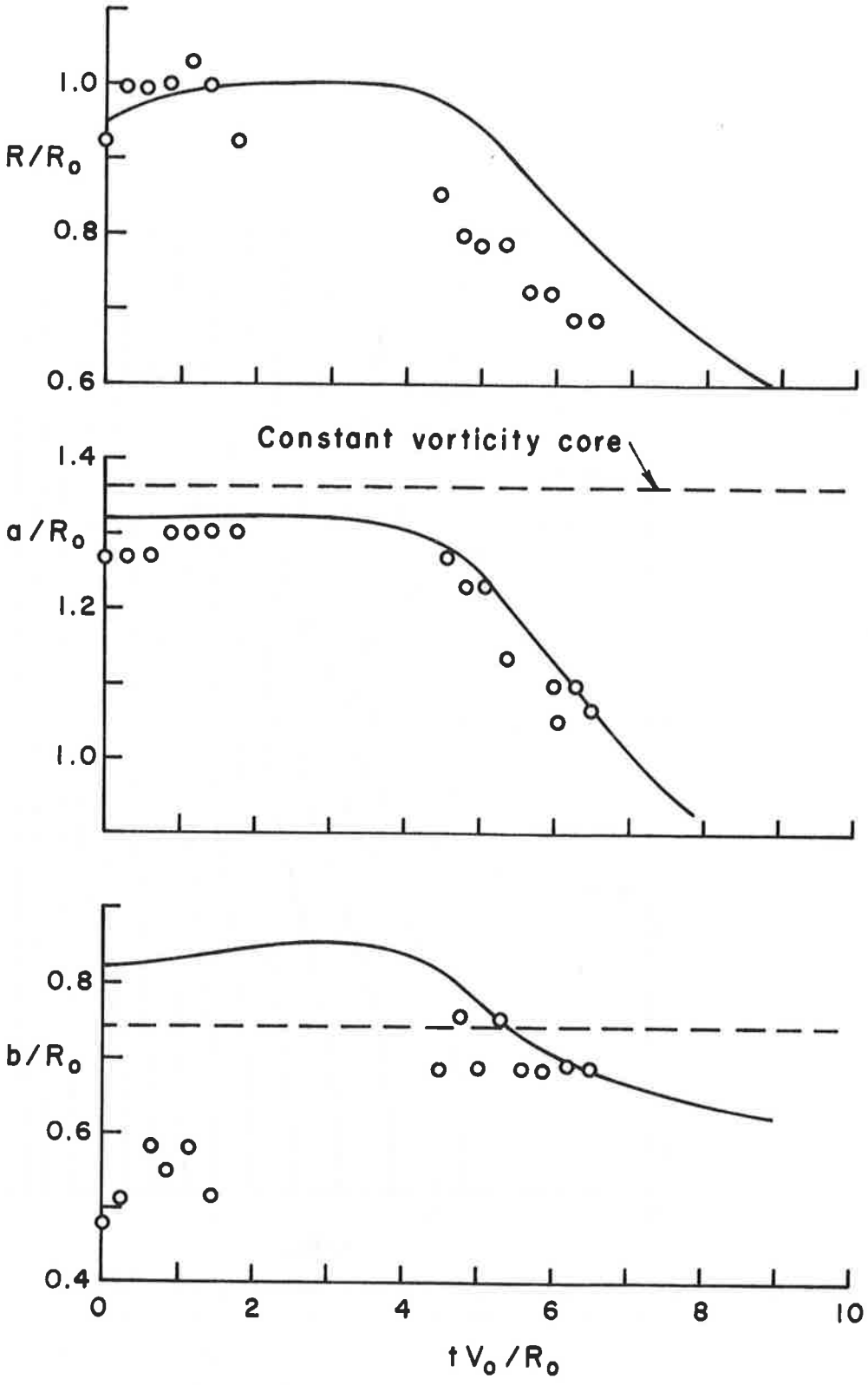

Figure 4-5. Vortex-ring radius and semi-major and semi-minor oval axes for penetration of density discontinuity, case 3. ⊙ Data; — axisymmetric stratified WAKE code calculation; — — — non-stratified, constant core vorticity value.

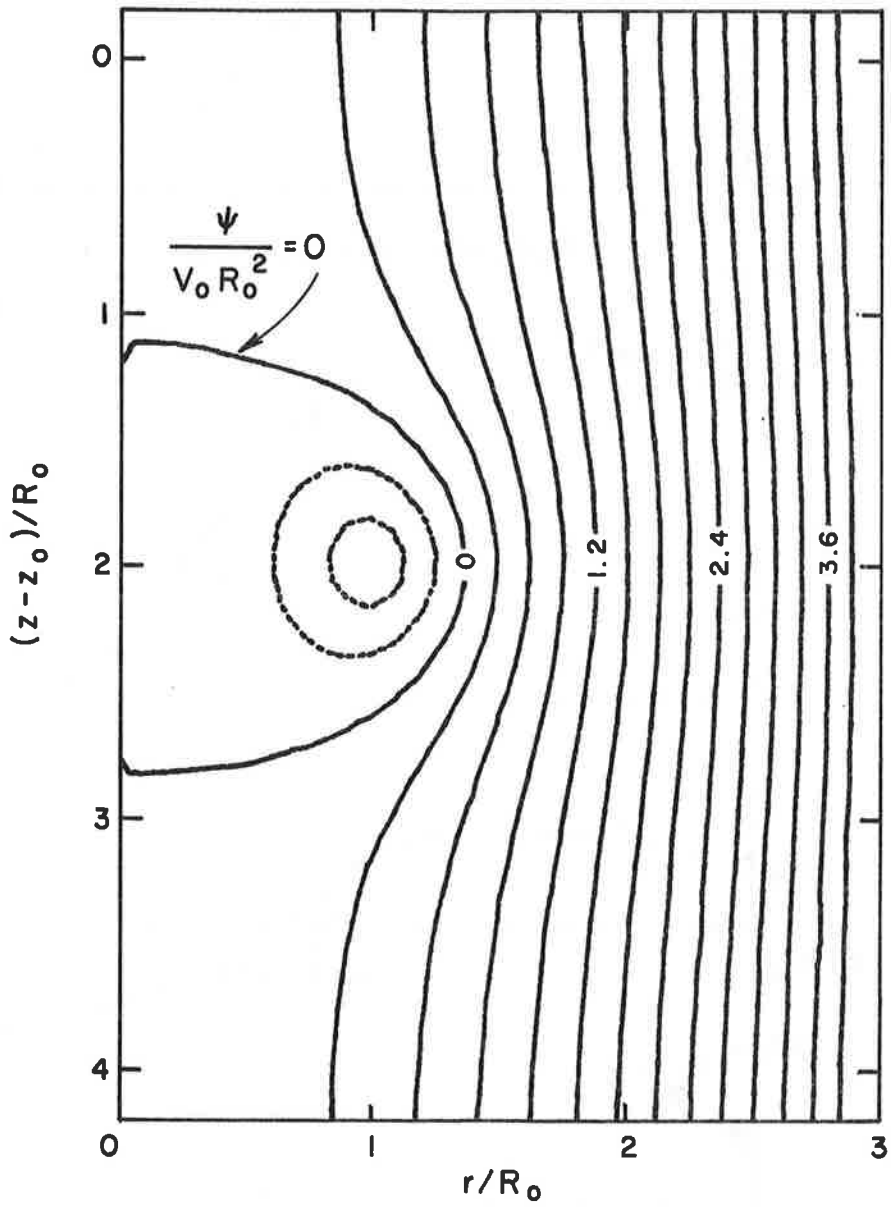

Figure 4-6a. Stream function for vortex ring descending into a density discontinuity, case 3. $(z-z_o)/R_o = 2.0$ at $tV_o/R_o = 2.0$. Stream function contours from $\psi = -0.6$ to 3.9 at intervals of 0.3.

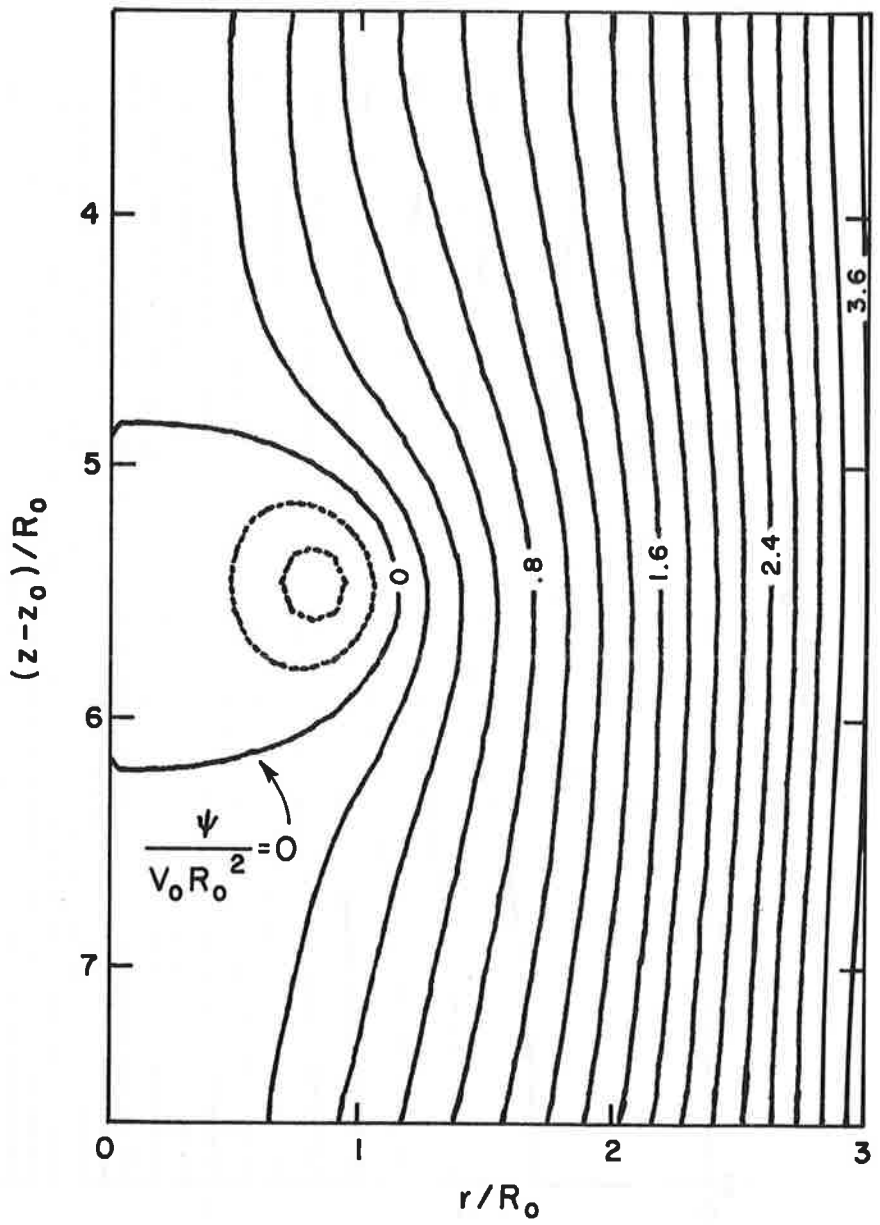

Figure 4-6b. Stream function for case 3. $(z-z_o)/R_o = 5.4$ at $tV_o/R_o = 6.0$. Stream function contours from $\psi = -0.4$ to $+3.2$ at intervals of 0.2.

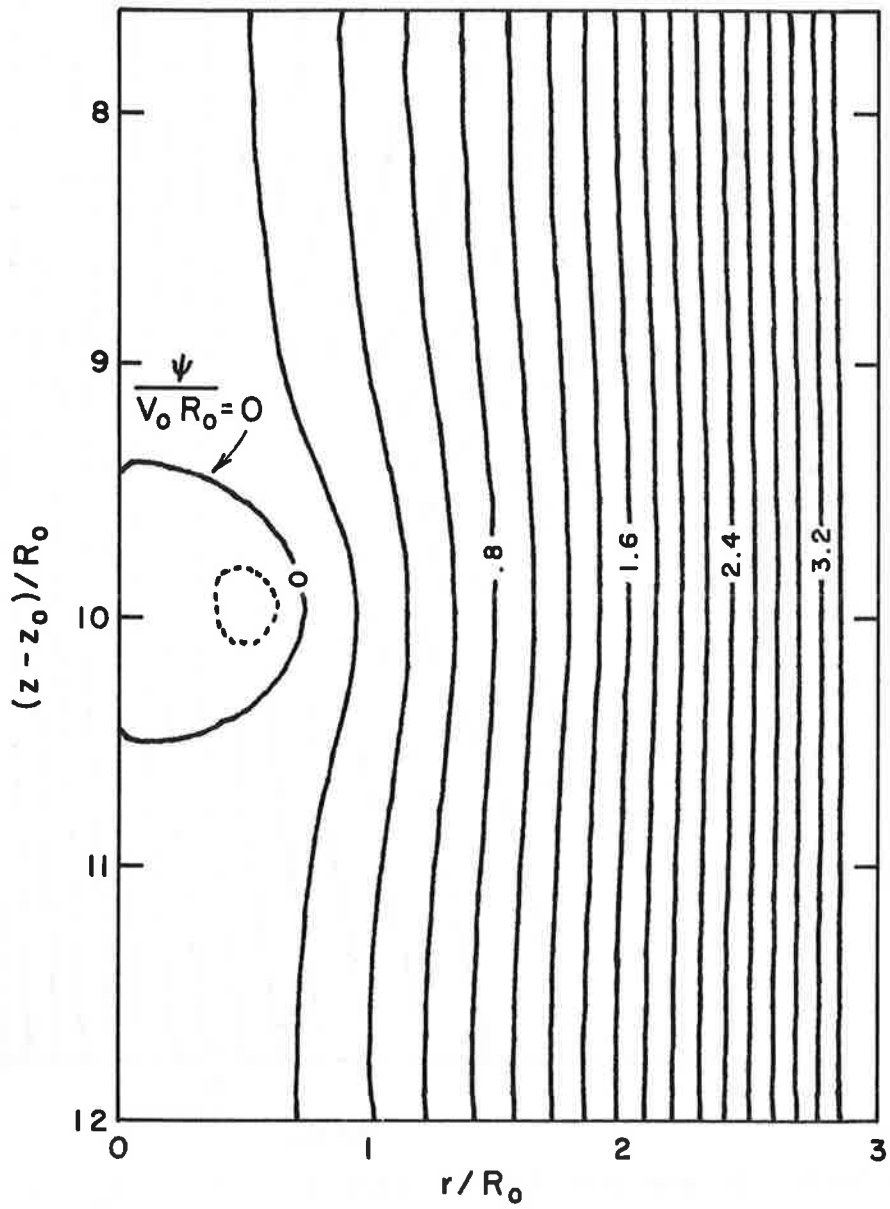

Figure 4-6c. Stream function for case 3. $(z-z_o)/R_o = 8.8$ at $tV_o/R_o = 10.0$. Stream function contours from $\psi = -.2$ to +3.4 at intervals of 0.2.

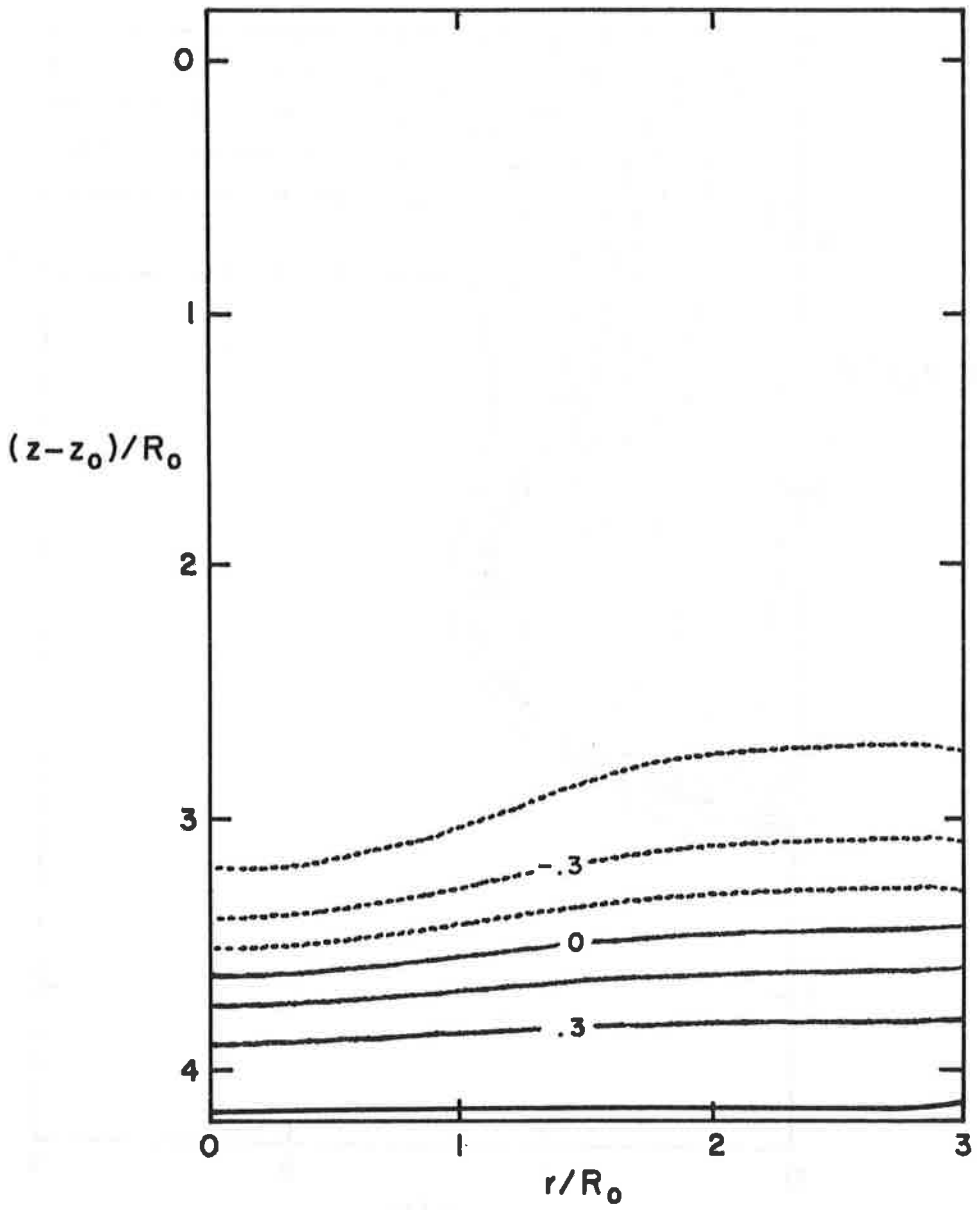

Figure 4-7a. Isopycnals for vortex-ring descent into a density discontinuity, case 3. Ring starting penetration of discontinuity, $tV_o/R_o = 2.0$, $(z-z_o)/R_o = 2.0$. Contours from -0.45 to +0.45 at intervals of 0.15.

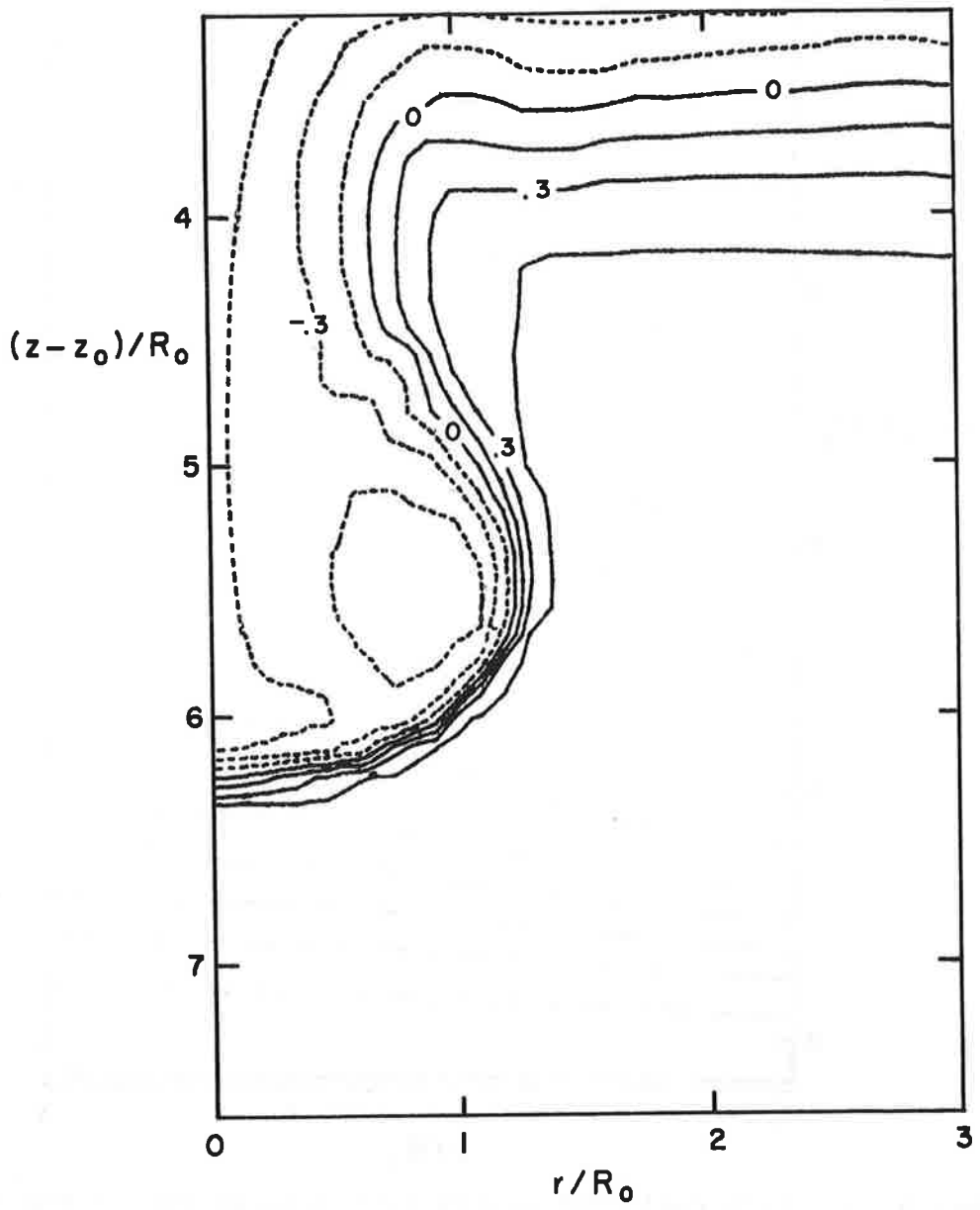

Figure 4-7b. Isopycnals for case 3 after penetration, tV_o/R_o = 6.0, $(z-z_o)/R_o$ = 5.4. Contours from -0.45 to +0.45 at intervals of 0.15.

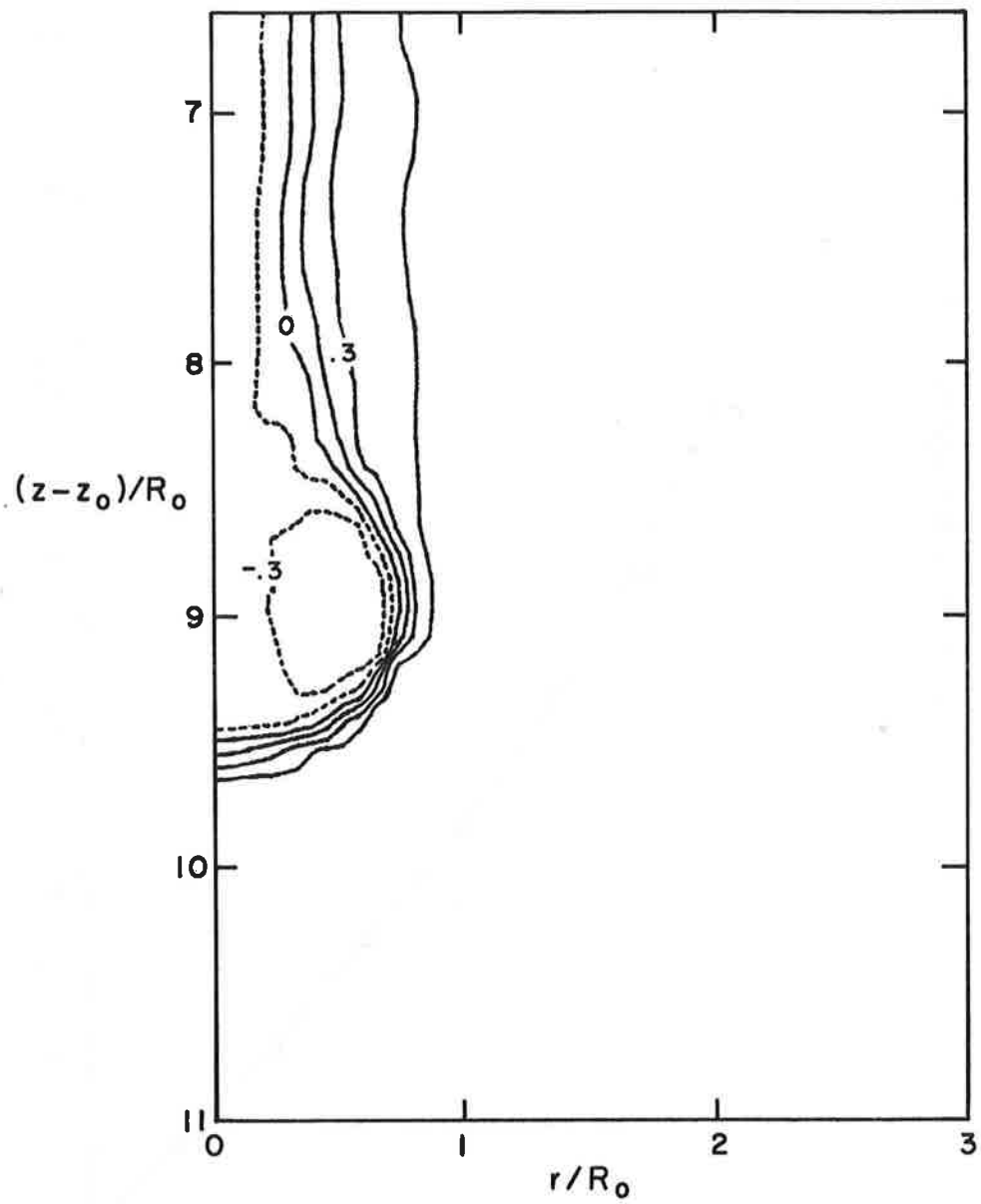

Figure 4.7c. Isopycnals for case 3 at tV_o/R_o = 10.0, $(z-z_o)/R_o$ = 8.8. Contours from -0.45 to +0.45 at intervals of 0.15.

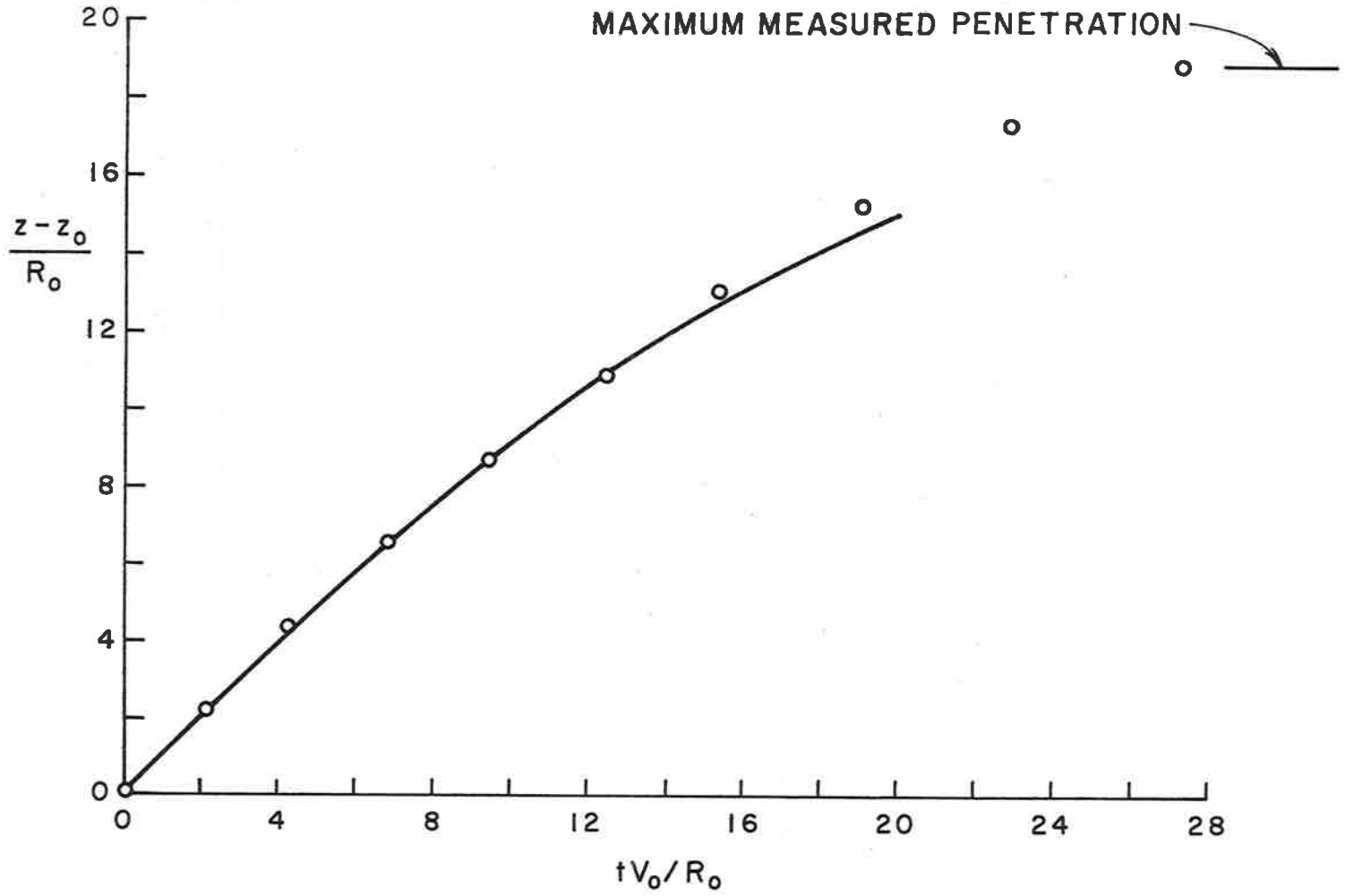

Figure 4-8. Vortex-ring trajectory in a linearly stratified fluid for $Fr_2 = 5.18$ (case 4). ⊙ Data; —axisymetric stratified WAKE code calculation.

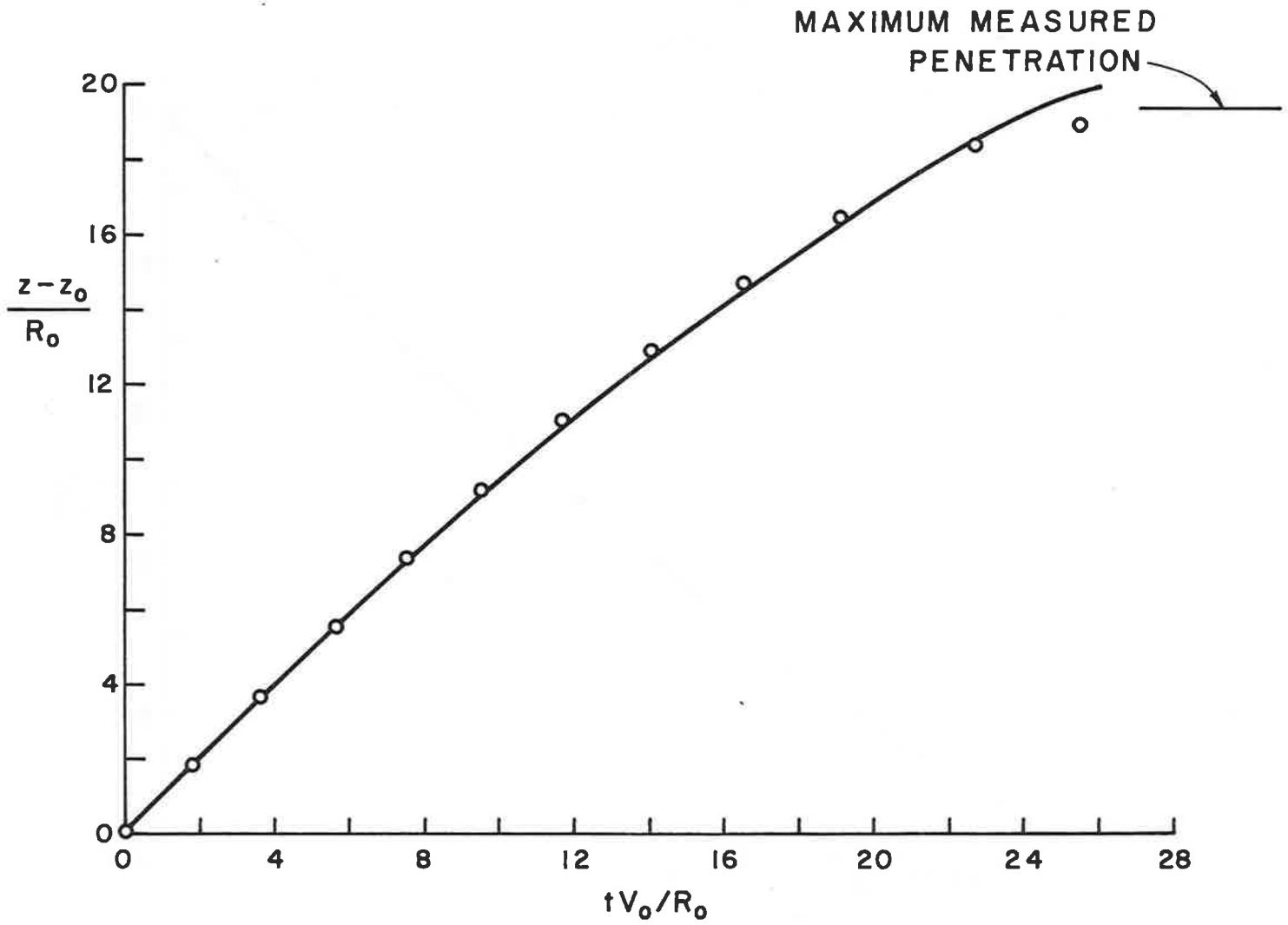

Figure 4-9. Vortex-ring trajectory in a linearly stratified fluid for $Fr_2 = 6.17$ (case 5)
⊙ Data; — axisymmetric stratified WAKE code calculation.

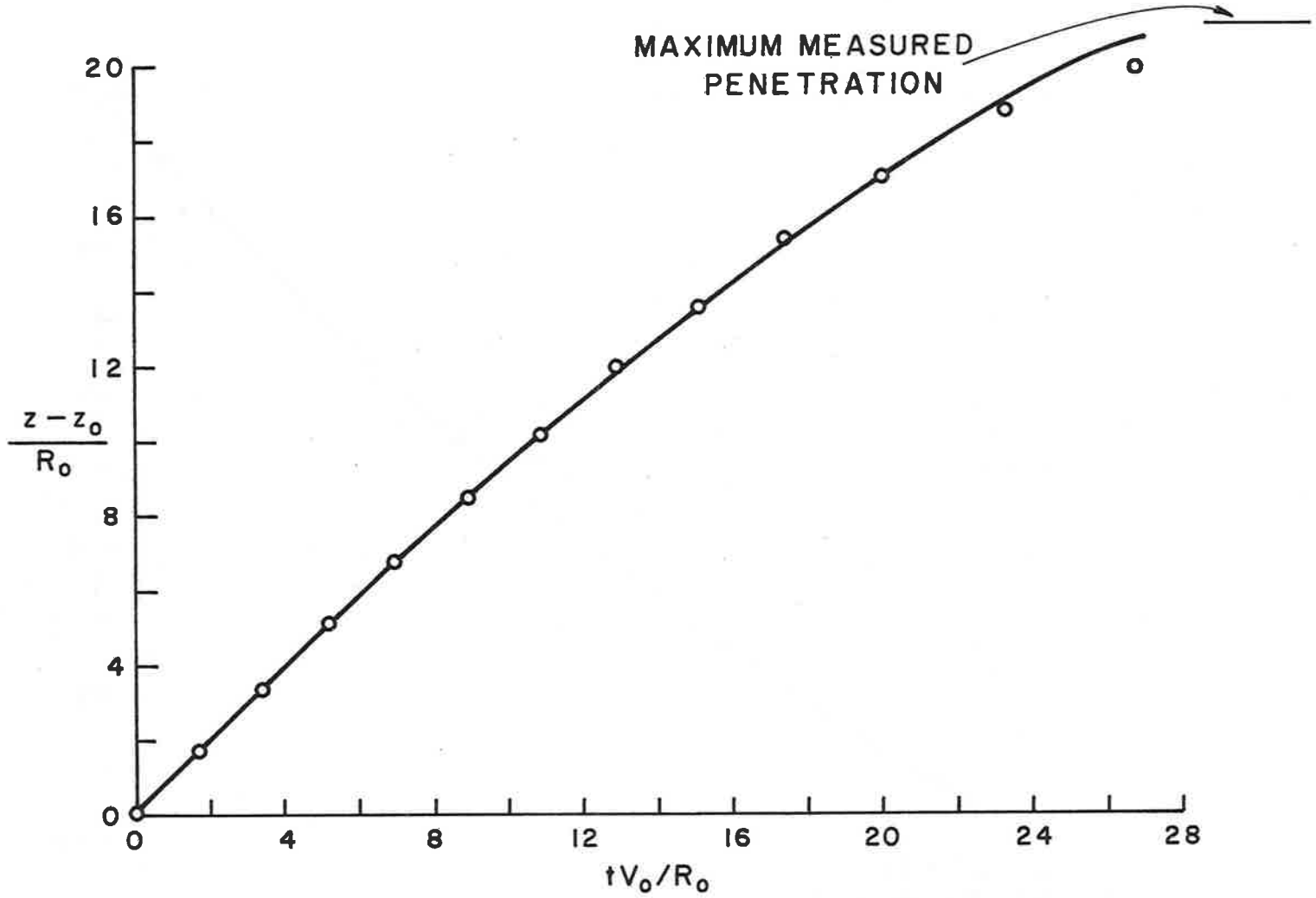

Figure 4-10. Vortex-ring trajectory in a linearly stratified fluid for Fr_2 - 6.57 (case 6)
⊙ Data; — axisymmetric stratified WAKE code calculation.

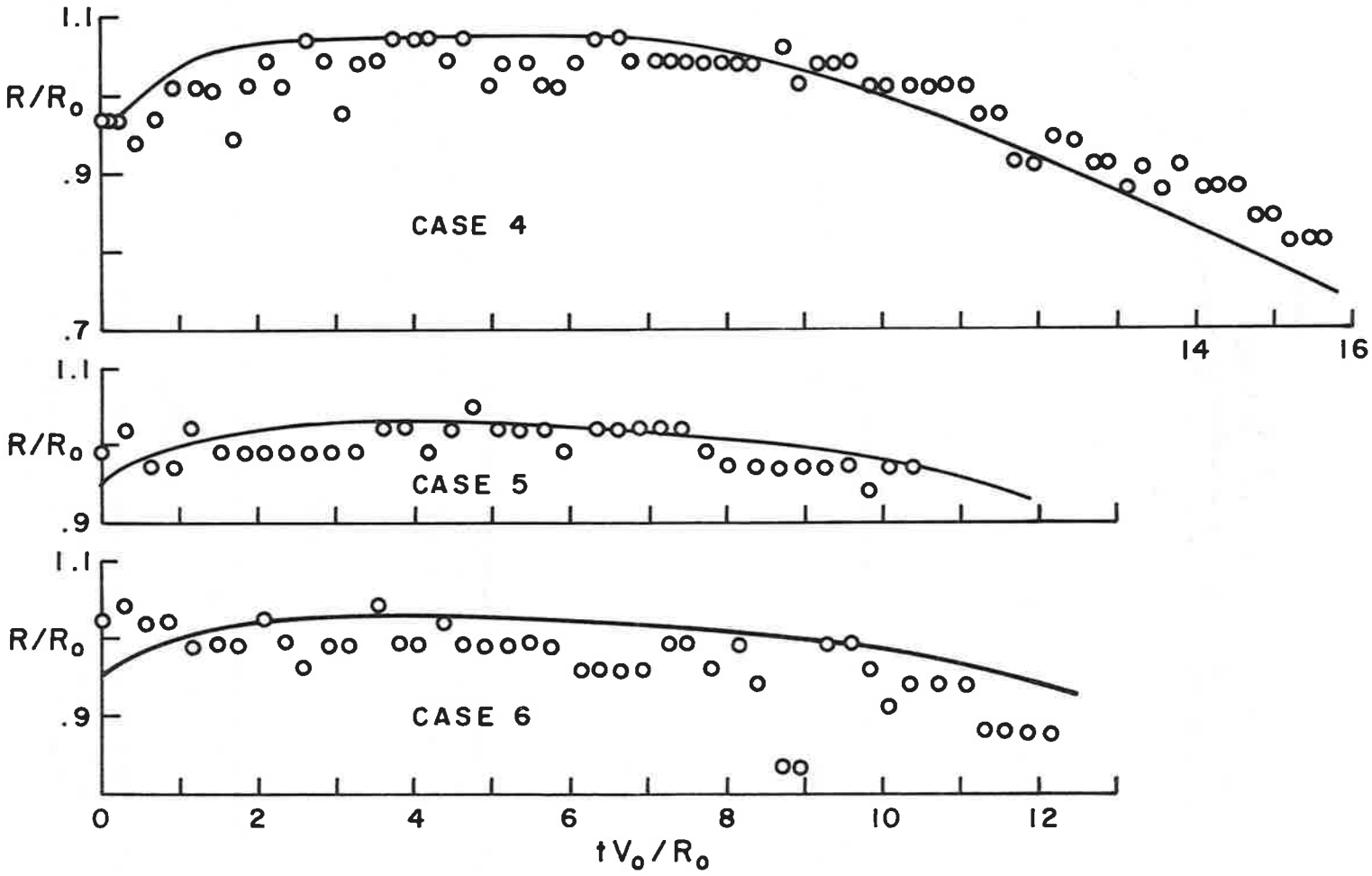

Figure 4-11. Vortex-ring radius history for Fr_2 = 5.18, 6.17, and 6.57 (cases 4, 5 and 6). ⊙ Data; — axisymmetric stratified WAKE code calculation.

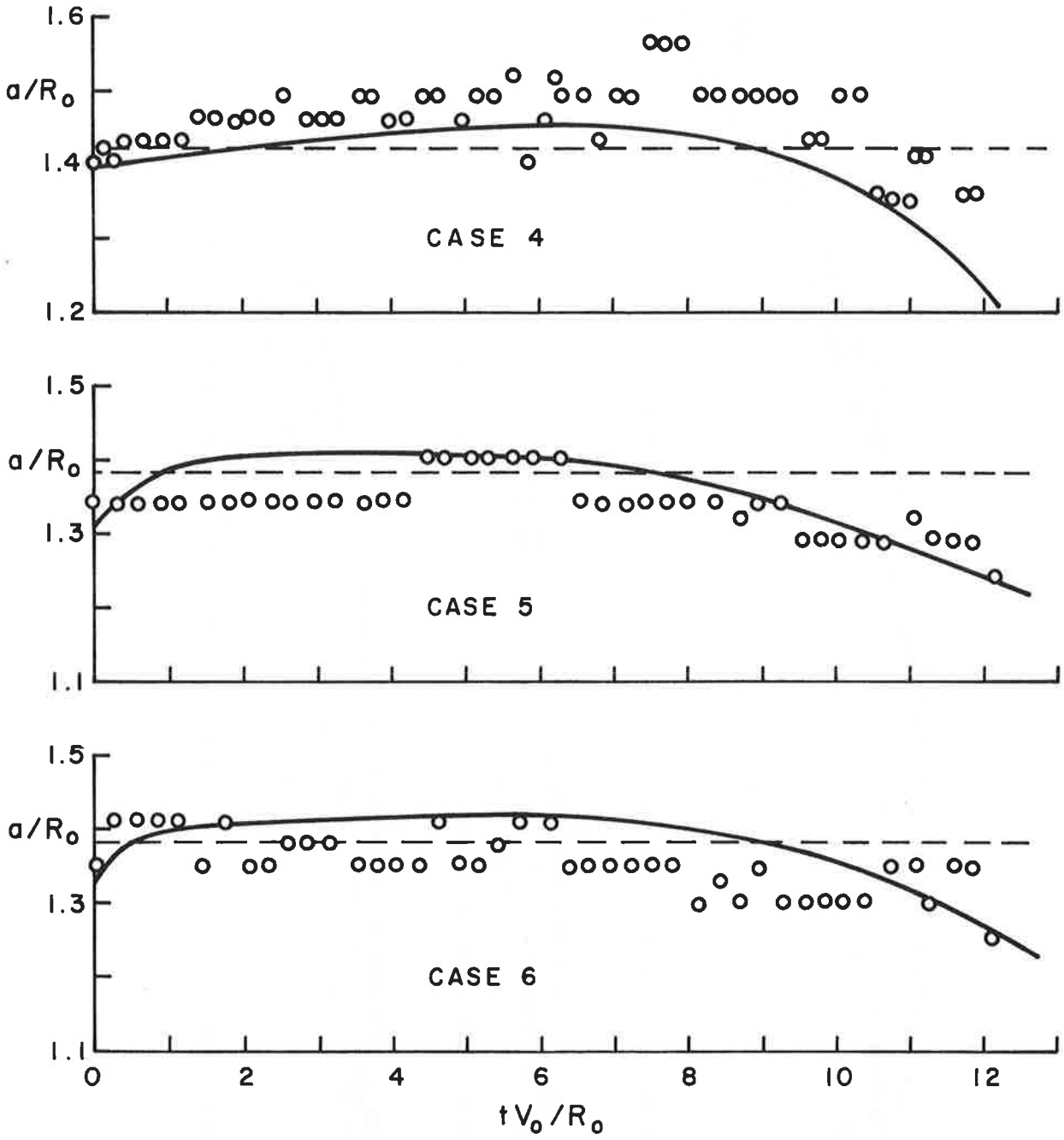

Figure 4-12. Vortex-ring semi-major axis history for Fr_2 = 5.18 , 6.17 and 6.57 (cases 4, 5 and 6). ⊙ Data; — axisymmetric stratified WAKE code calculation; — — — non-stratified constant core vorticity value.

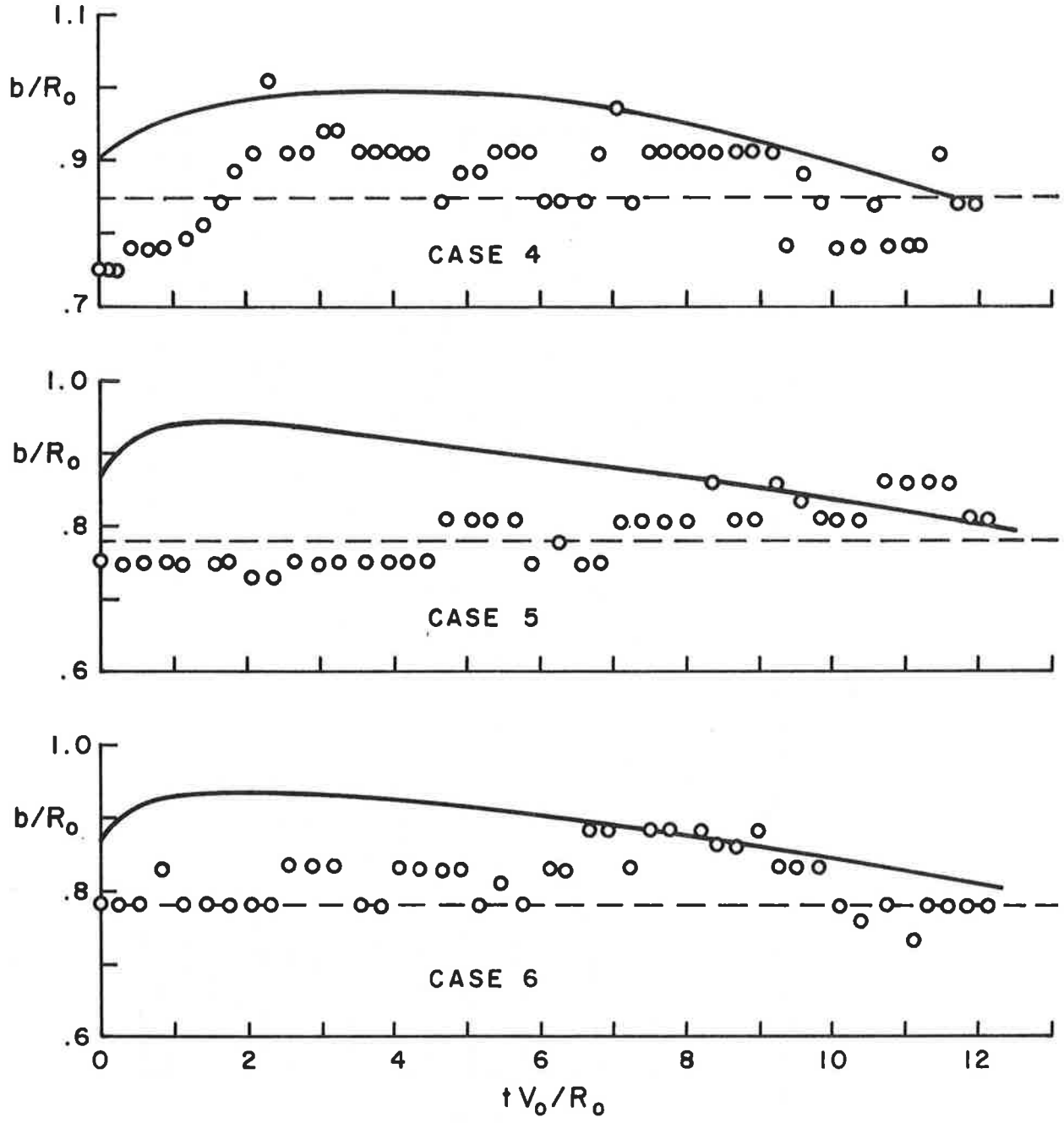

Figure 4-13. Vortex-ring semi-minor axis history for Fr_2 = 5.18, 6.17 and 6.57 (cases 4,5 and 6). ⊙ Data; — axisymmetric stratified WAKE code calculation; — — — non-stratified, constant core vorticity value.

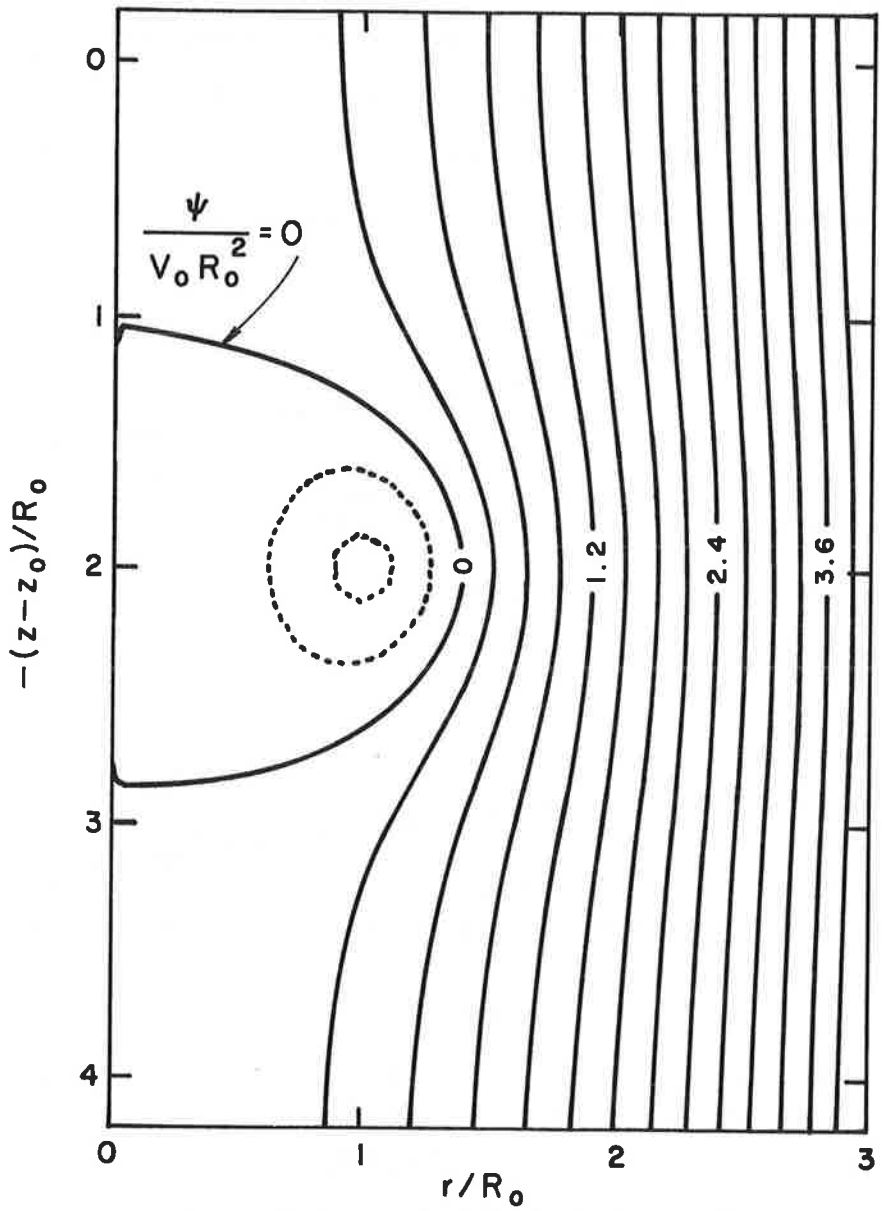

Figure 4-14a. Stream function for vortex ring descending in linear density stratification, case 6. $tV_o/R_o = 2.0$ at $(z-z_o)/R_o = 2.0$.

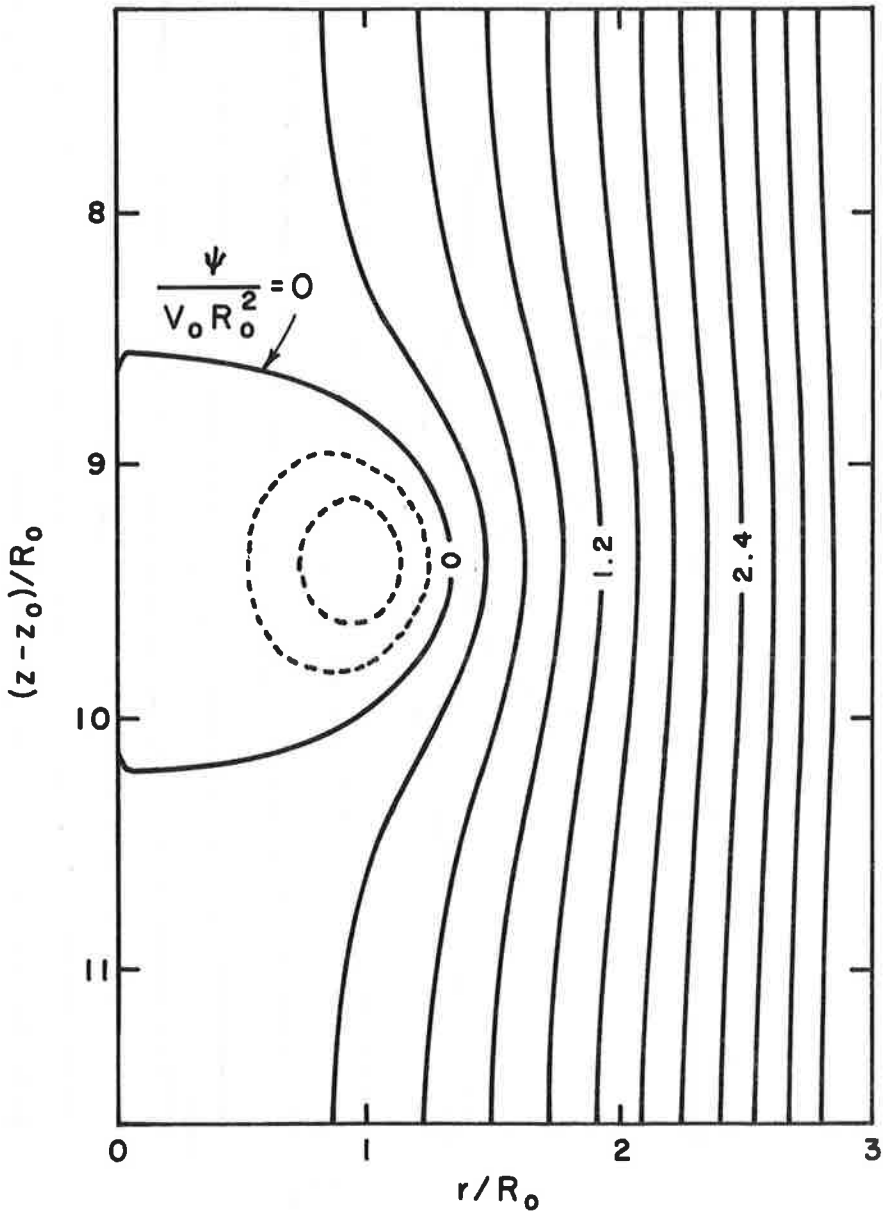

Figure 4-14b. Stream function for case 6 at $tV_o/R_o = 10.0$, $(z-z_o)/R_o = 9.4$.

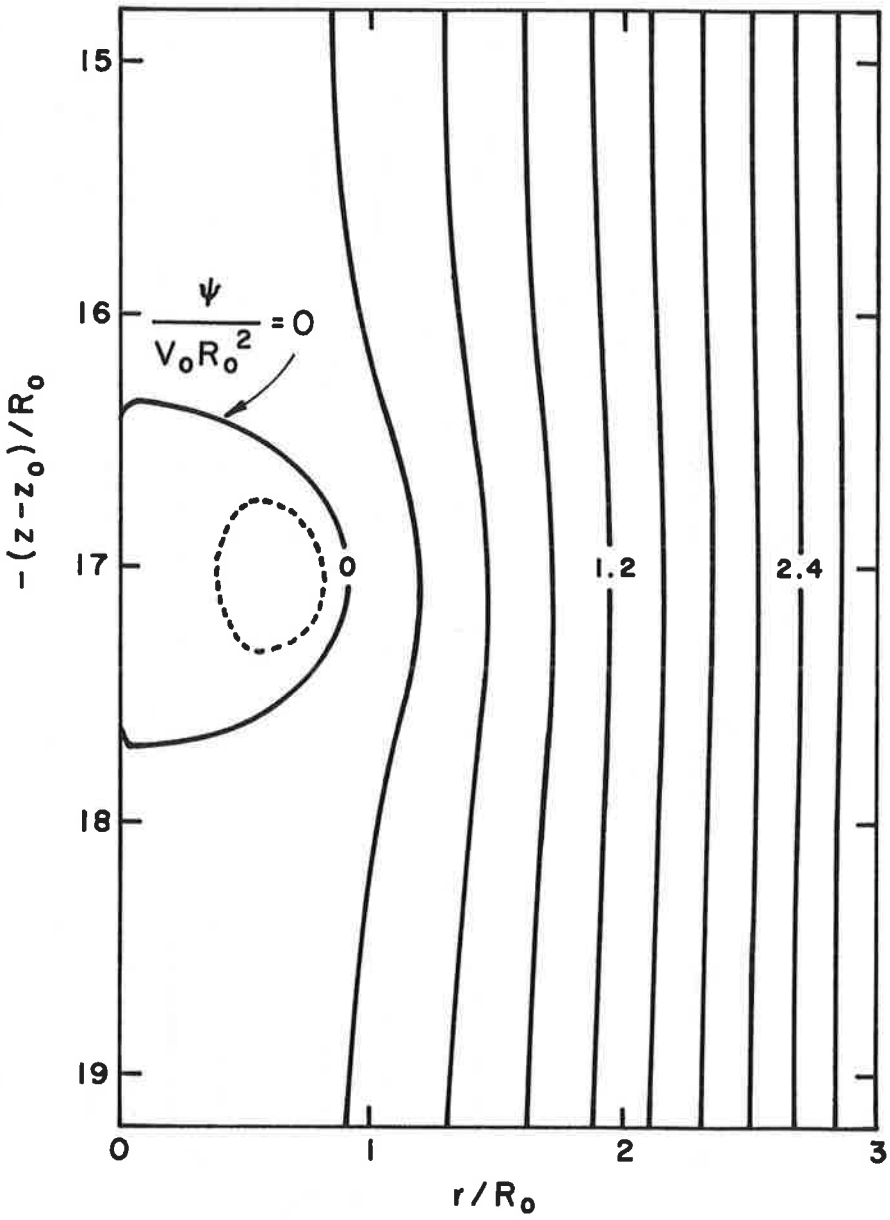

Figure 4-14c. Stream function for case 6 at $tV_o/R_o = 20.0$, $(z-z_o)/R_o = 17.0$.

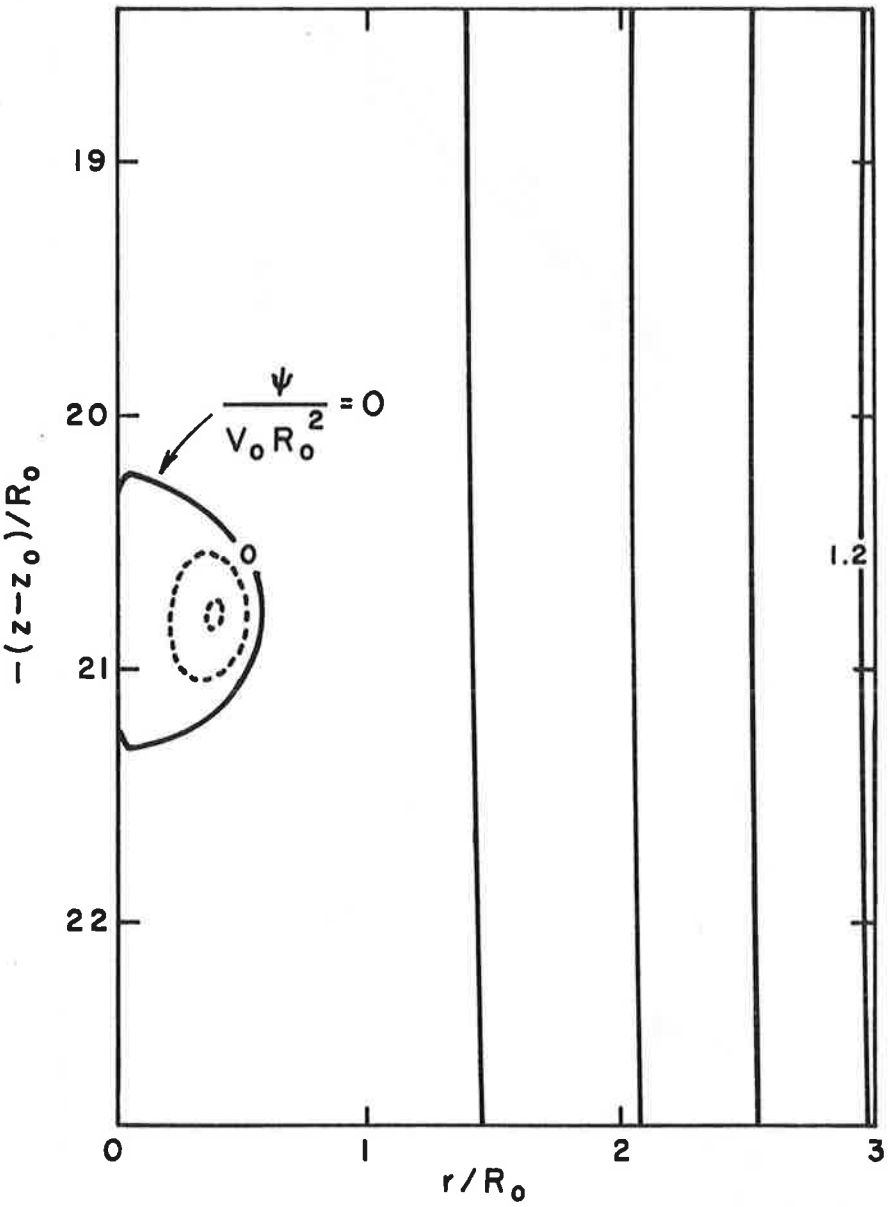

Figure 4-14d. Stream function for case 6 at $tV_o/R_o = 27.0$, $(z-z_o)/R_o = 20.6$.

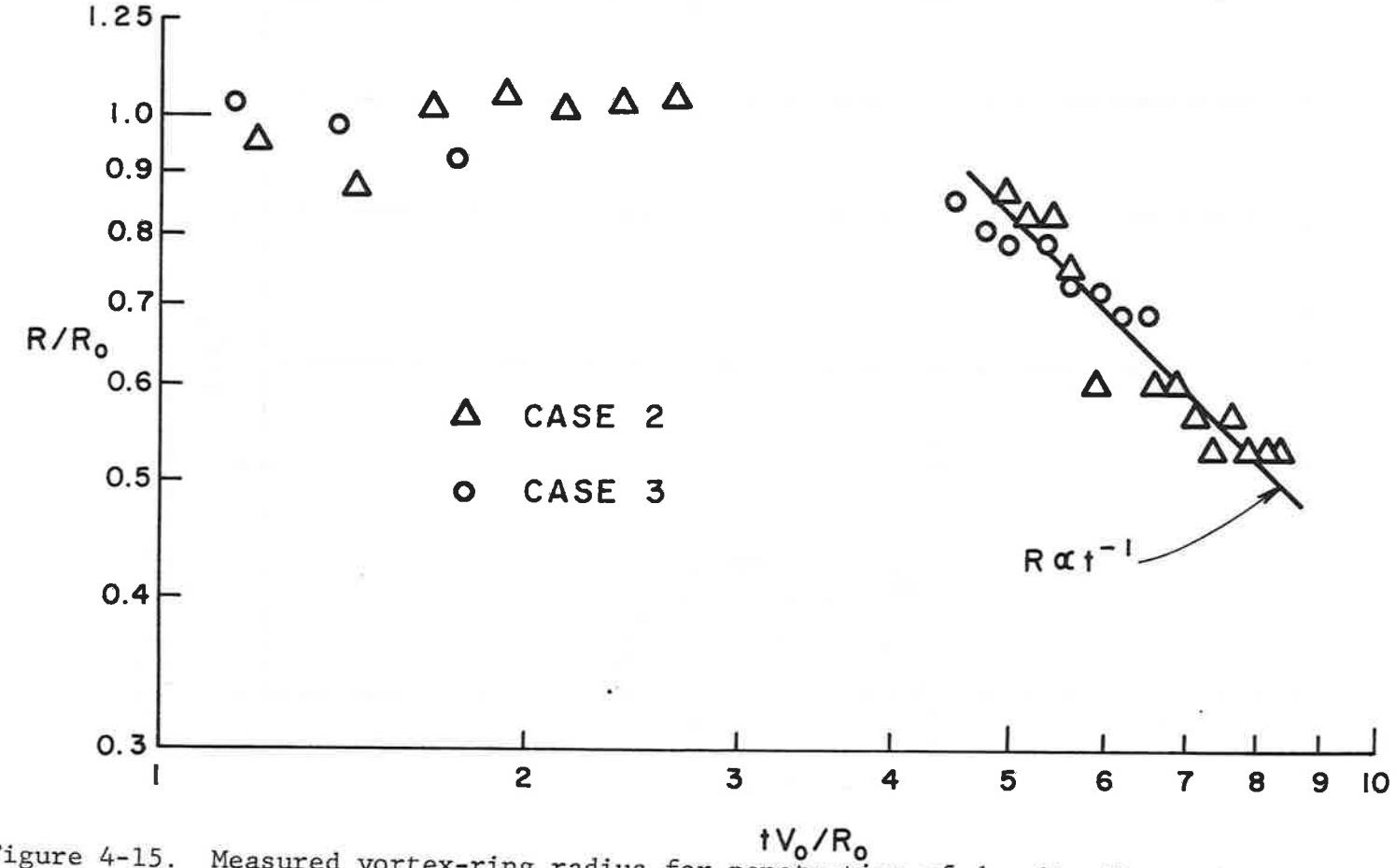

Figure 4-15. Measured vortex-ring radius for penetration of density discontinuity (cases 2 and 3).

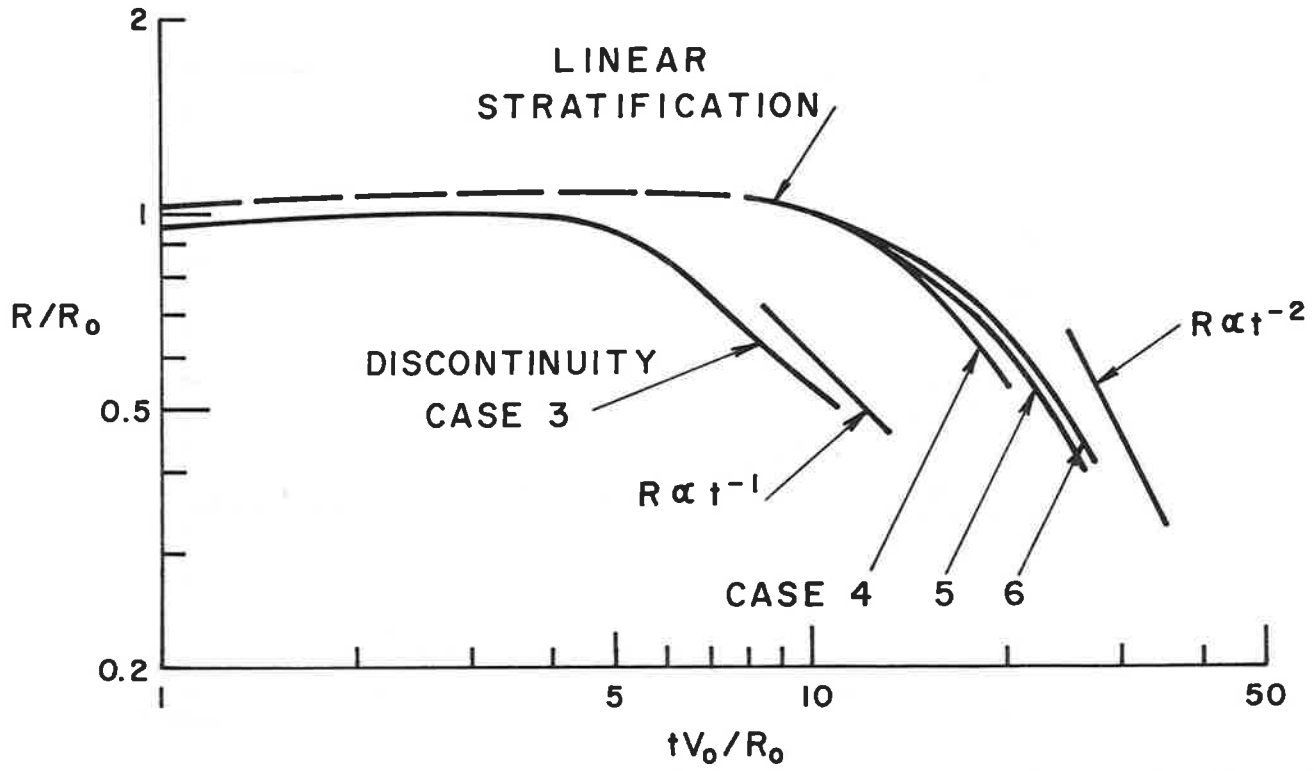

Figure 4-16. Calculated vortex-ring radius for penetration of density discontinuity and in linear stratification.

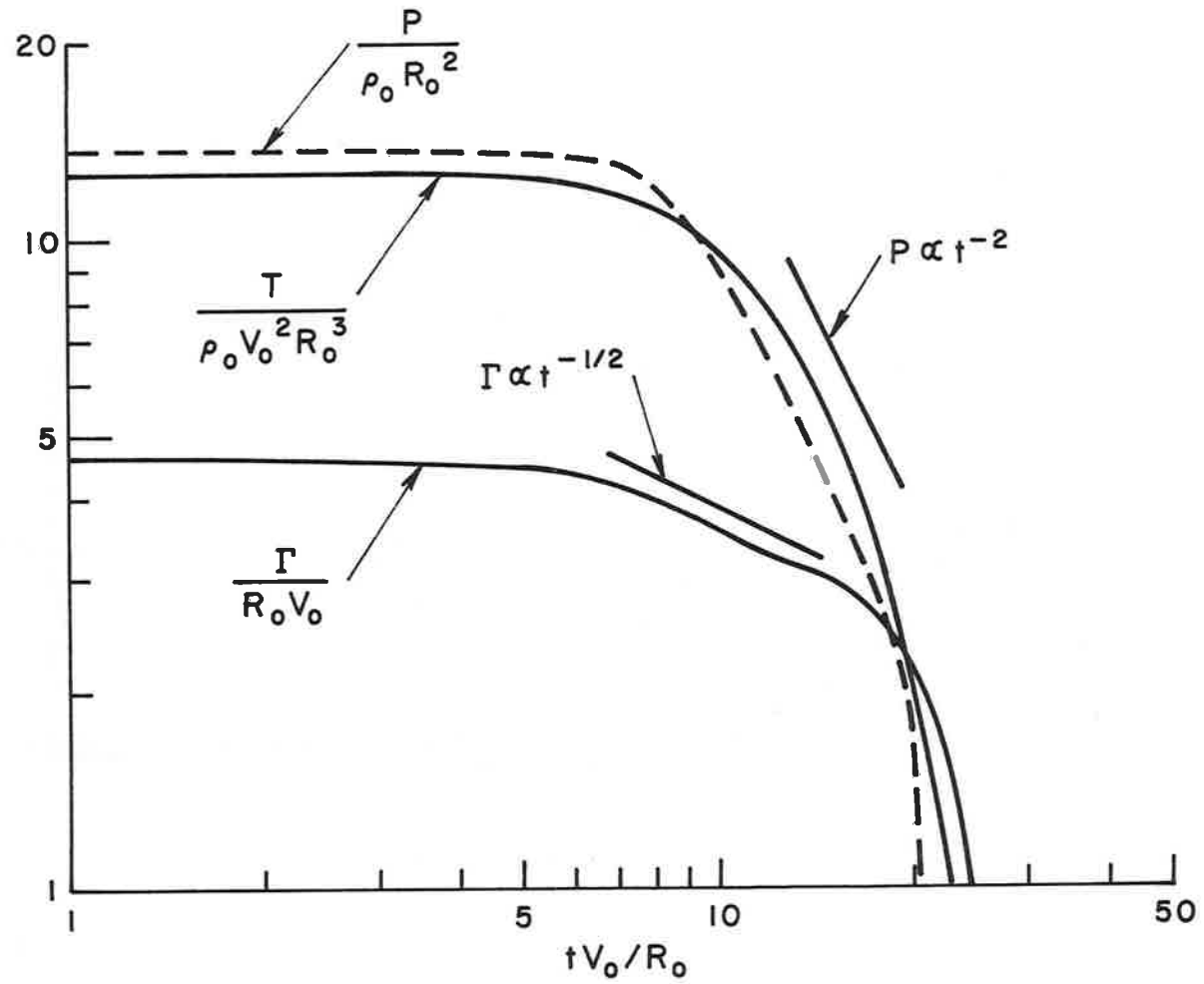

Figure 4-17. Calculated impulse, kinetic energy, and circulation for linear stratification for $Fr_2 = 6.57$ (case 6).

5. COMPARISON OF TWO-DIMENSIONAL WAKE CALCULATIONS WITH FULL-SCALE FLIGHT DATA

5.1 TWO-DIMENSIONAL WAKE CODE

The code validation contained in our vortex ring study provides increased confidence in the two-dimensional results to be compared with flight data. For vortex flows having moderate vorticity gradients, the solution procedure of the two-dimensional equations, which are included in Appendix A, may be identical to that used in solving the axisymmetric equations. However, due to the severity of the vortex wake chosen for the calculations to be presented here, a new technique for calculating strong vortex wakes has been developed. Details of this technique will be presented in following sections.

5.2 DATA SELECTION

To reduce extraneous effects which cannot be included in a numerical calculation, criteria were set up as a guide in selecting the flight case to be studied. A measurement made on a clean aircraft configuration (minimum flaps, no spoilers) in level flight was sought, and calm ambient conditions, e.g., low cross shear and ambient turbulence, were factors considered. The number and quality of measurements made during the test were also major factors in selection. Finally, of course, stable atmospheric stratification was a required condition.

The measurement selected for comparison with our numerical simulation was Run 8 of the 1975 Rosamond Dry Lake tests, made using a Boeing 747 aircraft. A complete description of these tests and data for all runs have been reported by Burnham, et al., Ref. 30. The measurements of vortex characteristics were taken with the aircraft in a variety of flap settings, landing gear and spoiler configurations, and meteorological conditions. Takeoff, level

flight, and landing aircraft attitudes also were varied. A total of 54 passes were flown at altitudes varying from 30- to 244- m. Test instrumentation included a monostatic acoustic system for vortex tracking and strength determination, three anemometer baselines for vortex tracking, and a mobile Laser-Doppler Velocimeter (LDV) for collecting detailed velocity signatures.

5.3 TEST CONDITIONS

The important flight and environmental parameters for Run 8 of the 1975 Rosamond Dry Lake tests is given in Table 5-1, taken from Table 2-3 of Ref. 30. The total circulation of the B-747 aircraft for this test run was reported to be 628 m^2/sec, the initial vortex separation to be 50 m , and the initial descent rate to be 2 m/sec. A total of about 80 sec of time test was recorded for this run.

The measured swirl velocity profile for Run 8 at 11 seconds after passage of the generating aircraft is shown in Figure 5-1, and the associated circulation profile is given in Figure 5-2. The curves through the data are based on a constant vorticity core and a Hoffman-Joubert turbulent vortex circulation profile (Ref. 31), beyond a radius of 1.5 m . At 10.0-m radius, the velocity is assumed to depend upon the inverse radius (zero vorticity).

The swirl velocity as shown in Figure 5-1 represents a severe vortex wake, with a maximum swirl velocity of nearly 17 m/sec occurring at a radius of 2.5 m . To resolve this profile numerically requires mesh points in the computation at less than 1-m intervals. Because we must also resolve the effects of stratification, which are occurring at the edges of the oval more than 25 m from the core region, and to provide a large enough domain to avoid wave interference effects at the computational boundaries, the outer boundary (horizontally) must be placed at least at 75 m from the wake centerline, which because of symmetry constitutes one of the vertical computational boundaries. The WAKE code is presently limited to a 33x40 mesh on our DEC® PDP-11/70 computer, and

TABLE 5-1. FLIGHT PARAMETERS AND METEOROLOGICAL FACTORS OF RUN 8, 1975 ROSAMOND DRY LAKE TESTS (REF.30)

Flight time	0745 PST
Altitude	244 m
Airspeed	77 m/sec
Aircraft weight	244000 kg
Flap setting	30/30 (deg)
Landing gear	Down
Spoilers	None
Thrust (EPR)	1.20
Wind speed	1 m/sec
Wind direction	310 deg
Atmospheric dissipation rate ($\varepsilon^{1/3}$)*	1.4 $cm^{2/3}/sec$
Lapse rate	1 $^{o}C/100$ m
Flight attitude	Level

*At flight altitude.

therefore, a calculation requiring the resolution of a small-scale phenomenon on a large numerical domain is beyond the capabilities of the code, even if a nonuniform grid is employed. If the code were reconfigured to allow more grid points (necessitating a far greater amount of disk I/O), a time step of 0.05 seconds would be needed in order to satisfy the CFL (Courant-Friedrichs-Lewy) condition due to the large swirl velocity. To simulate 70 sec of test time would require approximately 1400 time steps, which would use more than 100 hours of CPU (central processor unit) time on our PDP-11/70, and at least three times as much real time due to the excessive number of disk operations required for such a fine grid.

The feasibility of the computation would be in doubt if the calculation were carried out along traditional lines. A new approach was therefore initiated for the computation as described below.

5.4 VORTEX WAKE CALCULATION BASED ON A SPLITTING TECHNIQUE

From an examination of the data, it was noticed that the decay in the circulation profile was small over most of the test period. It was decided that the departure of the vortex from its initial state was the basis of an improved calculation procedure. The computation would consequently be relieved of supporting the advection of vorticity and turbulence by a purely numerical calculation of the advection velocities.

If the vorticity were written as the sum of the initial vorticity distribution and a time-varying perturbation about the initial state (hence the designation, splitting technique), and substituted into the governing equations, we would obtain equations which may be solved for the time-dependent portion. Perturbation about the initial state does not imply an approximation here in the sense of small variations. The procedure is an exact one and is done to reduce the magnitude of the numerically calculated vorticity and velocities. Depending upon the complexity of the analytical expression selected for the initial vorticity profile, the initial conditions can be represented as closely as we choose.

The benefits gained by this procedure are twofold. First, the analytical vorticity and velocities, which will be large compared to perturbation quantities over most of the calculation time, are invariant with time at each grid point. Numerical noise is therefore reduced considerably. Second, the perturbations are initially zero, and if they are to remain small over the computation lifetime, the perturbation gradients will also be small. This relaxes somewhat the mesh size requirements, opens up the allowable time step, and simultaneously reduces the risk of numerical instability.

To provide a smooth generating function for the initial vorticity, a Gaussian profile is chosen to match the swirl velocity and circulation profiles as closely as possible with this type of distribution. The vorticity used for the calculations is

$$\zeta_o = 14.4 \left[e^{-(r_1/3.7)^2} - e^{-(r_2/3.7)^2} \right] \qquad (5.1)$$

in sec^{-1}, where r_1 is measured from y = 25, z = 0 m, and r_2 from y = -25, z = 0 m. The swirl velocity and circulation profile derived from this vorticity are compared with data in Figures 5-3 and 5-4. These profiles do not represent the measured velocity and circulation as closely as the profiles of Figures 5-1 and 5-2. They are generated by three different vorticity functions over the radius of the vortex, and introduce discontinuous derivatives at two regions of the calculation. The Gaussian profile is used to avoid this possible source of numerical instability. Note that, since we are calculating the perturbation vorticity, it should be possible to use a generating function which is only approximately equal to the actual profile. If our calculation does indeed simulate the physics of the vortex flow, the generating function plus perturbation should evolve toward the measured vortex profiles as the computation proceeds.

To accommodate the perturbation procedure, the mean vorticity equation in Cartesian coordinates may be written in the following form:

$$\frac{\partial \zeta'}{\partial t} + (v_o + v') \frac{\partial \zeta'}{\partial y} + (w_o + w') \frac{\partial \zeta'}{\partial z}$$

$$= -v_o \frac{\partial \zeta_o}{\partial y} - w_o \frac{\partial \zeta_o}{\partial z} - \frac{g}{\Theta_o} \frac{\partial \Theta}{\partial y} - \frac{\partial^2}{\partial z^2} \langle vw \rangle$$

$$- \frac{\partial^2}{\partial y \partial z} (\langle vv \rangle - \langle ww \rangle) + \frac{\partial^2}{\partial y^2} \langle vw \rangle$$

$$+ \nu \nabla^2 (\zeta_o + \zeta') \quad , \tag{5.2}$$

where the zero subscript here denotes the analytically derived velocities due to the initial vorticity field. The perturbation vorticity and velocities are denoted by primes. The perturbation stream function is calculated from

$$\nabla^2 \psi' = -\zeta' \quad , \tag{5.3}$$

and

$$v' = -\frac{\partial \psi'}{\partial z} \quad , \tag{5.4a}$$

$$w' = \frac{\partial \psi'}{\partial y} \quad . \tag{5.4b}$$

The vortices were kept in the center of the computational domain by an algorithm which traced the maximum total vorticity $\zeta = \zeta_o + \zeta'$, and kept this at $z = 0$, by adding an appropriate vertical washing velocity into the calculation.

The perturbation and initial velocities entered into the calculation of the turbulence correlations in both the advection terms and the velocity gradient terms. The advection terms in the Reynolds stress equations were treated as shown above for the vorticity equation. The velocity gradients in the production terms of the turbulence equations were written as the sum of the analytically derived gradients of the initial velocity and the numerically calculated gradients of the perturbation velocities. A shortwave filter algorithm (Sheng, Ref. 32) was used to control

numerical noise on the perturbation vorticity and turbulence velocity correlations. However, the filter was used only when the criterion on maximum shortwave oscillations (local peaks and curvature) was exceeded in two directions simultaneously.

5.5 AMBIENT STRATIFICATION

The stable ambient stratification at the flight altitude is measured to be 1 ^{o}C/100 m. During descent, a vortex pair compresses, however, at a rate of approximately 1 ^{o}C/100 m if it is assumed the compression is adiabatic. The calculations are performed using potential temperature as the independent variable and the stratification set equal to 2 ^{o}C/100 m. The effective Brunt-Väisälä frequency is therefore

$$N = \left[\frac{g}{\theta_o}\frac{d\theta_o}{dz}\right]^{1/2} = 0.0265 \text{ rad/sec} \quad , \tag{5.5}$$

where $\theta_o = 280$ ^{o}C . Defining the Froude number to be

$$Fr_3 = \frac{\Gamma_o}{2\pi s^2 N} \quad , \tag{5.6}$$

the Froude number for Run 8 at 11 seconds after aircraft passage is equal to 6.03.

5.6 INITIAL AND AMBIENT TURBULENCE

The initial turbulence within the vortices could not be measured. An estimate of the initial turbulence was made by employing the observed time required for smoke entrained in the vortex to diffuse to the edge of the cell, as reported in Ref. 30. This led to an initial turbulence level q of about 1 m^2/sec^2 .

The ambient turbulence may be derived from the measured ambient dissipation rate ε . Based on an assumed ambient turbulence scale of 2.5 m , the ambient turbulence is about 0.03 m^2/sec^2 . This level should not appreciably affect the behavior of the vortices over the time scale of the self-generated turbulence and stratification effects on the vortices.

5.7 TURBULENCE SCALE

The macroscale Λ of the self-generated turbulence is one of the most uncertain variables of the vortex flow phenomenon we are investigating. It is expected that this scale may be controlled by the characteristic dimensions of the flow field, which in this case are three in number: the core radius, the core separation, and the length associated with the gradient of density occurring at the boundary of the cell of recirculating fluid. Generation of the turbulence and the length scale of this turbulence is a function of the core size and the density gradient scale in the respective regions of turbulence production. Using the vortex-ring results as a guide, where $\Lambda/R_o = 0.03$ gives the best results, $\Lambda/s = 0.03$ is used in the present analysis.

5.8 COMPARISON OF WAKE CALCULATIONS WITH DATA

The data reported by Burnham et al. in Ref. 30 included histories of the vortex pair descent velocity and altitude, separation between vortices, maximum tangential velocity, and the vortex circulation and average circulation vs. radius. The average circulation vs. radius was defined in Ref. 30 as

$$\Gamma_{avg} = \frac{1}{r} \int_o^r \Gamma(r)dr \qquad (5.7)$$

The calculated vortex-pair descent velocity and altitude are compared with the measured values in Figures 5-5a and 5-5b, respectively. The agreement between measurement and calculation is excellent. Note that the measured descent velocity and vortex altitude oscillate about a mean which is represented by the calculated values. These oscillations are similar to those that one would expect to see by observing the spiriling motion of one vortex about another. This phenomenon did occur during the tests where inboard flap generated vortices were seen to spiral about and merge with the tip vortices. The period of rotation for this interaction was, however, considerably shorter than 30 seconds, and merging of these vortices occurred about 3 wing spans behind the aircraft.

Note that the calculated tip vortex descent velocity decreases monotonically and does not accelerate as predicted by several previous analyses, see Table 1-1.

Figure 5-6 shows a comparison between the measured and calculated average circulation, defined by Eq.(5.7), at 5-, 10-, and 15-, m radii from the center of the core. Γ_{avg} was calculated using a radially varying $\Gamma(r)$, which in turn was calculated based on an area integration of the vorticity out to radius r. The point $r = 0$ corresponded to the maximum stream function. The integration was carried out in a circle with maximum radius defined by the distance from $r = 0$ to the centerline between the vortices.

The profiles of circulation, $\Gamma(r)$ vs. r, from 11 to 76 sec are presented in Figures 5-7a to 5-7f. The characteristics of the measured circulation and average circulation profiles are represented by the calculations. The initial rate of decrease in Γ and Γ_{avg} is small, increasing gradually to the end of the measurement. The decrease in circulation with radius as the edge of the recirculation cell is approached is due to the countersign vorticity in this region. This decrease is predicted by the calculation, and can be seen in the data.

Figure 5-8 shows a comparison between the measured maximum tangential velocity and the calculated value. Again, the agreement is excellent over most of the data period. Note that, even after the vortex pair has stopped descending, there is still an appreciable swirl velocity in the core. The vortices, therefore, have considerable strength remaining although they have been stopped in their descent by the stratification. This result has been previously found in our atmospheric-wake vortex interaction study described in Ref. 13.

The separation between the vortices is shown in Figure 5-9. The data here extend out only to about 25 sec, when one of the vortices drifts beyond the scanner elevation angle limit. The

separation is calculated to remain nearly unchanged over more than one-half of the descent time, decreasing by more than 10 percent of the initial separation only during the final stages of descent. This decrease in separation is more than found previously, see Bilanin et al., Ref. 13. The vortex studied there is an initially more diffuse, aged vortex, while the present one is in a much earlier stage. The aged vortex is dominated by turbulent diffusion in and about the core region. Turbulence production in the center of the core of the measured vortex is suppressed by the centrifugal effects of the swirling flow, and turbulence there is due only to that diffused inward or due to axial gradients of velocity. During the time in which stratification effects are occurring, the present vortices are dominated by the turbulence in the cell boundary region. Figures 5-10a to 5-10d are contour plots of the vorticity in the core region, and show a very slow decay over most of the test period. Note that the vertical coordinate z in these and following figures is measured from the vortex pair altitude at 11 sec after passage of the aircraft, 220 m.

Figure 5-11 shows contours of the calculated vorticity at 65 sec in the core region, with contour intervals of 3 sec^{-1}, and in the diffuse region containing the countersign, stratification generated vorticity, with intervals of 0.05 sec^{-1}. Although small in value locally, the large extent of the countersign vorticity is sufficient to stop the descent of the primary vorticity in and around the cores. A calculation of the descent velocity based on the strength and centroid of the primary and countersign vorticity at 65 sec predicts a descent velocity of 0.9 m/sec. The actual mean descent velocity of the numerical calculation is 0.4 m/sec. This disparity is due to the very diffuse extent of the countersign vorticity, and a simple, concentrated vorticity argument cannot be used accurately. The simplified calculation does, however, predict a decrease in vortex-descent velocity and not an increase as occurs if only the core separation is used as a basis for the calculation.

The balance between the primary and countersign vorticity can be appreciated by seeing their variation with time, Figure 5-12, which is plotted non-dimensionally. The total circulation Γ decreases by nearly one-half, a consequence of the countersign circulation Γ_c. The circulation of the primary vortex, $\Gamma_p = \Gamma - \Gamma_c$, remains high however. Note that Γ_c is nearly linear in time for this vortex. Also shown in Figure 5-12 are T, the total kinetic energy of both vortices, which is initially equal to that of an elliptically loaded wing, and P, the impulse. There appears to be no simple time dependence for either the energy or the impluse.

The calculated streamline patterns at 11, 39, 55, and 65 sec are shown in Figures 5-13a through 5-13d, respectively. The recirculation cell area decreases gradually toward the end of descent, again in agreement with our previous findings reported in Ref. 13.

The last figures, 5-14a to 5-14c, are contour plots of q^2 at 18, 39, and 55 sec, respectively, showing the development of the turbulence field with time. The level of turbulence is a maximum in a ring of approximately 6-m radius, decreasing to 10 percent of this maximum at the center of the core. After the field has developed, it remains remarkably constant with time due to the very tight, stable core structure. The maximum velocity associated with the turbulence is approximately 10 percent of the maximum swirl velocity.

No temperature measurements were made for the tests analyzed here. Most notable about the calculated temperature field was the uniformity of temperature throughout the recirculation cell. The potential temperature of the cell remained very nearly at its initial value, indicating only very slight entrainment of ambient fluid during descent.

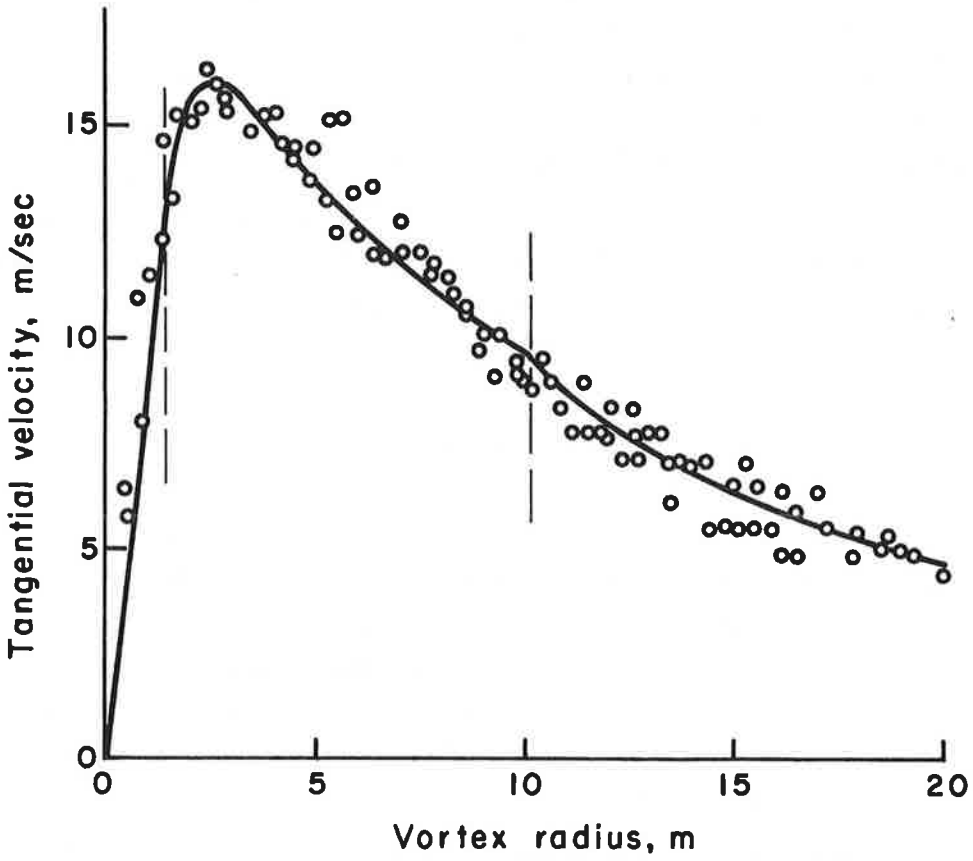

Figure 5-1. Measured Boeing 747 vortex swirl velocity vs. radius at 11 sec after aircraft passage and analytical representation based on constant vorticity core ($r < 1.5$m), Hoffman-Joubert turbulent profile ($1.5 < r < 10$m), and irrotational velocity profile ($r > 10$m).

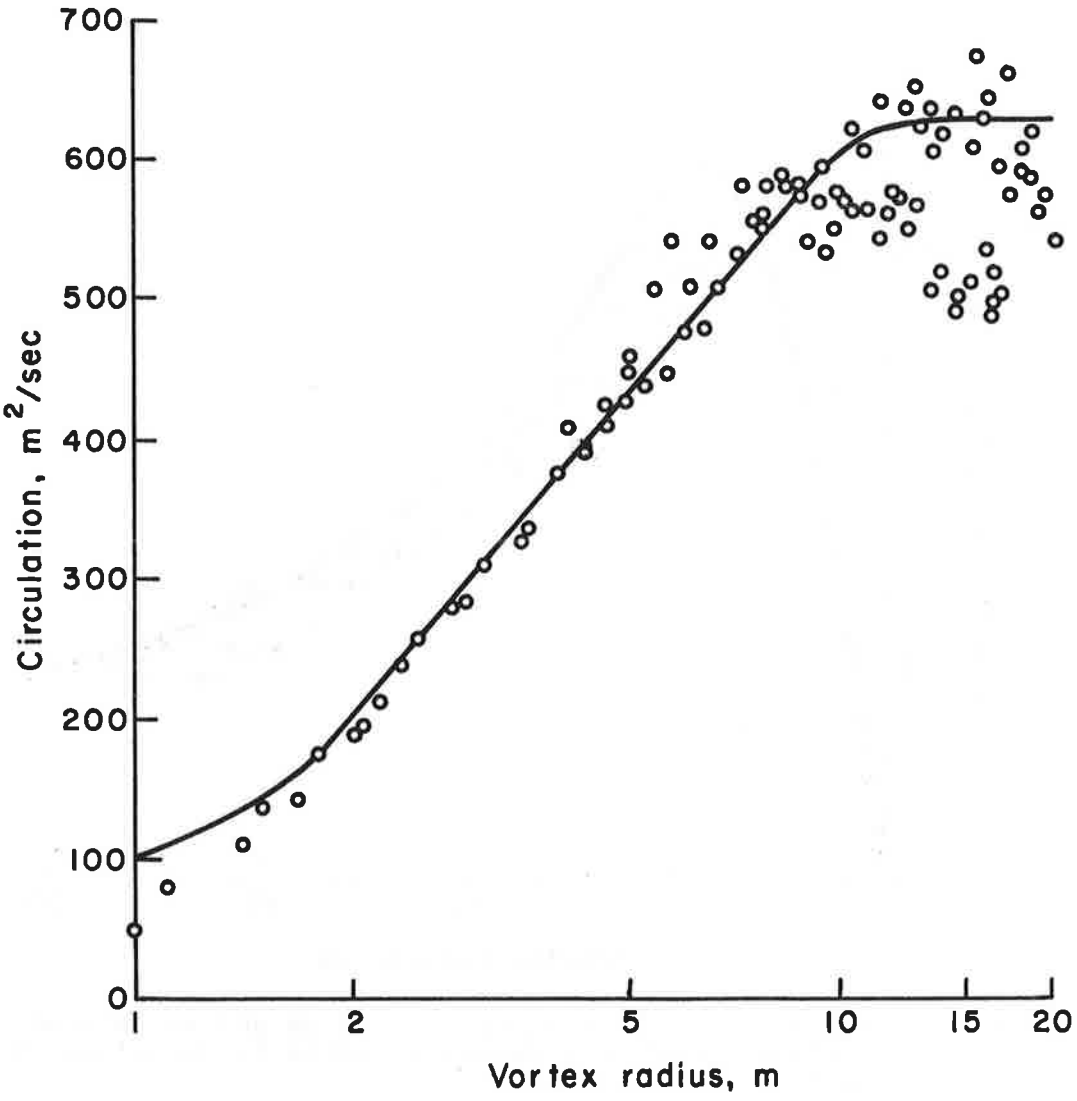

Figure 5-2. Measured and analytical circulation profile vs. radius at 11 sec.

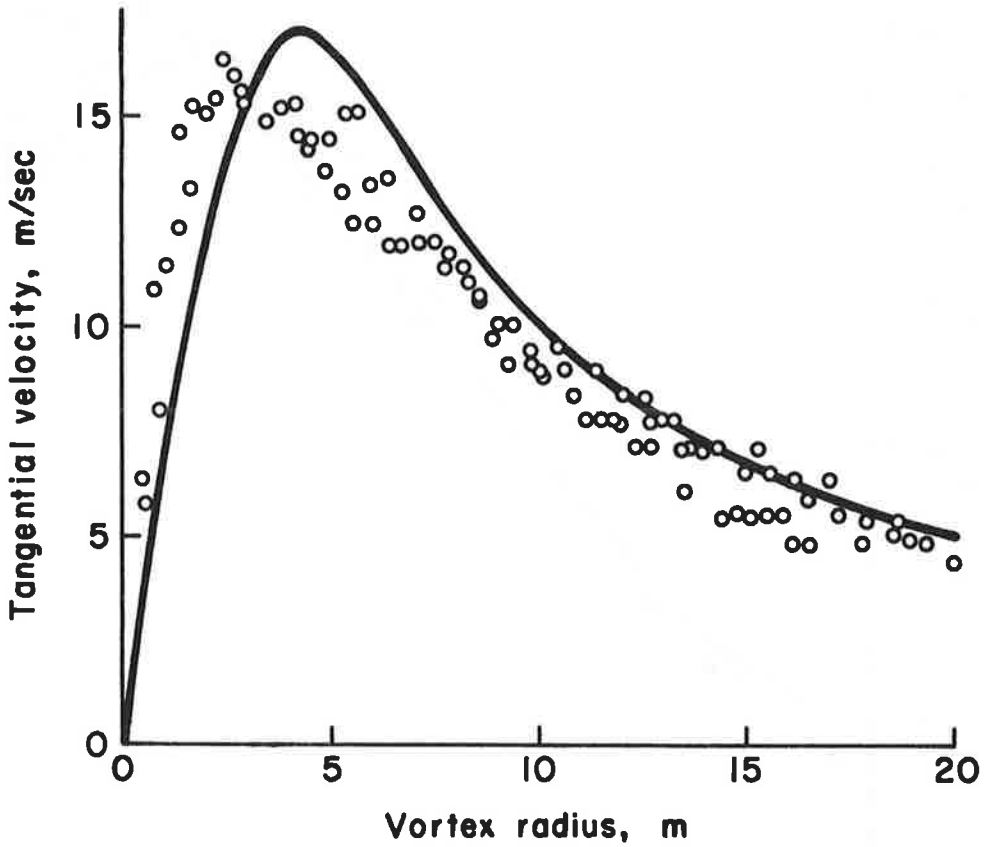

Figure 5-3. Measured swirl velocity vs. radius and analytical profile based on a Gaussian vorticity distribution at 11 sec.

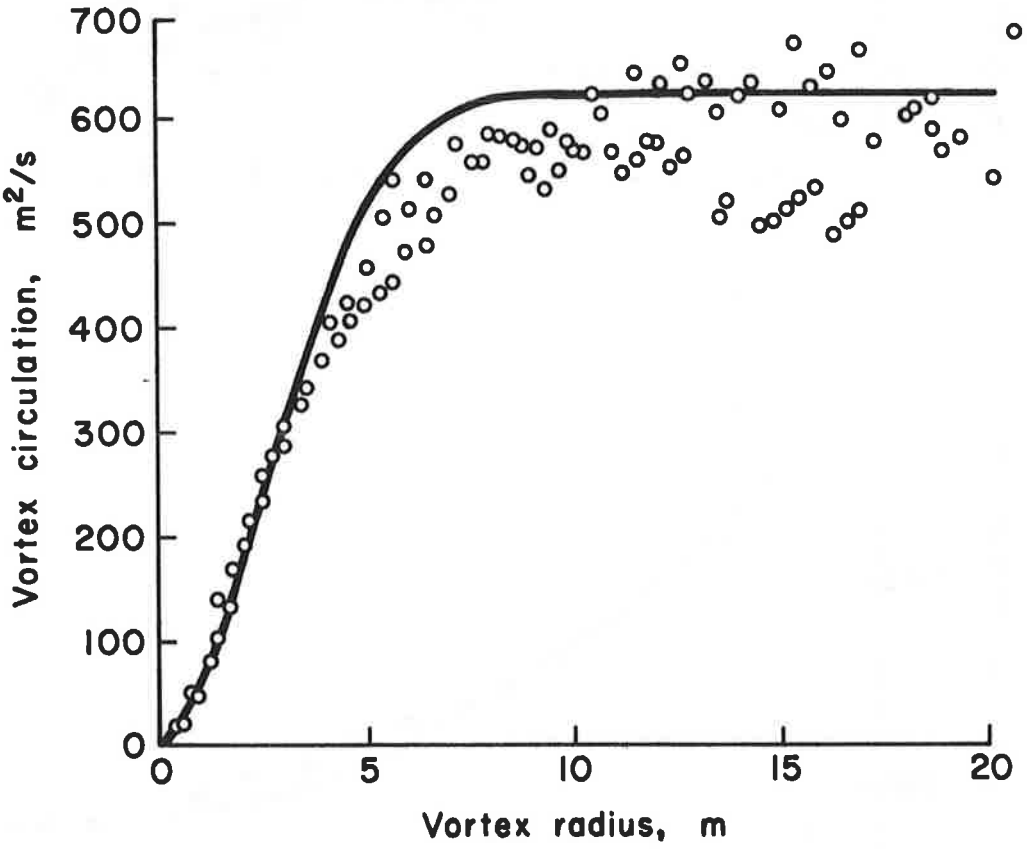

Figure 5-4. Measured circulation distribution and analytical profile based on a Gaussian vorticity distribution at 11 sec.

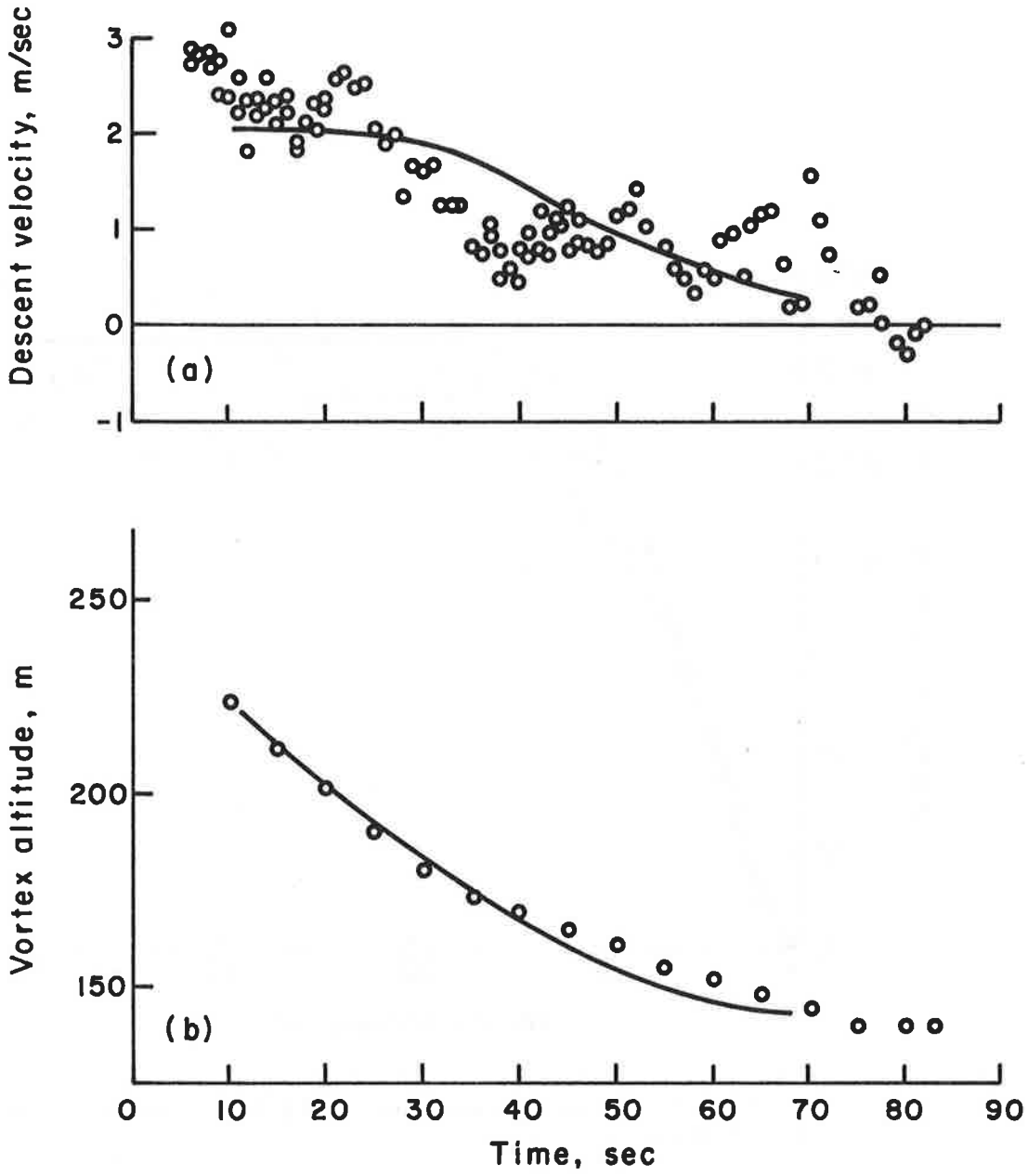

Figure 5-5. Comparison between measured and calculated vortex descent velocity (a) and altitude (b) vs. time.

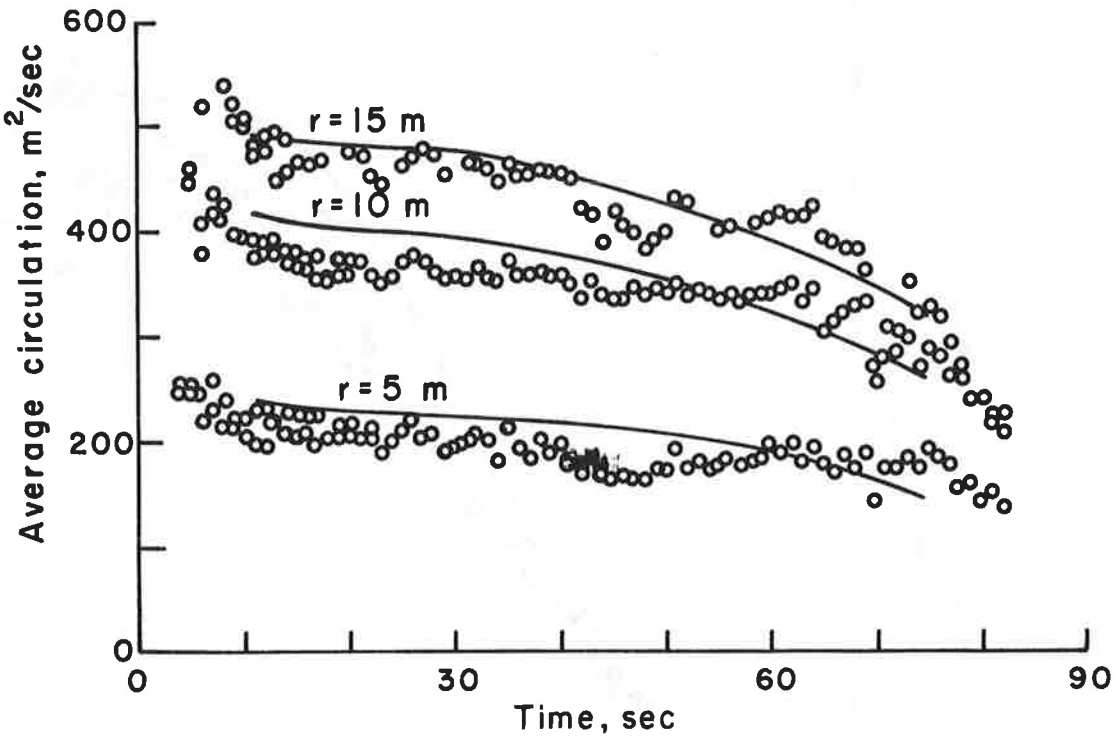

Figure 5-6. Comparison between measured and calculated average circulation vs. time at 5-, 10-, and 15-m radius from vortex center.

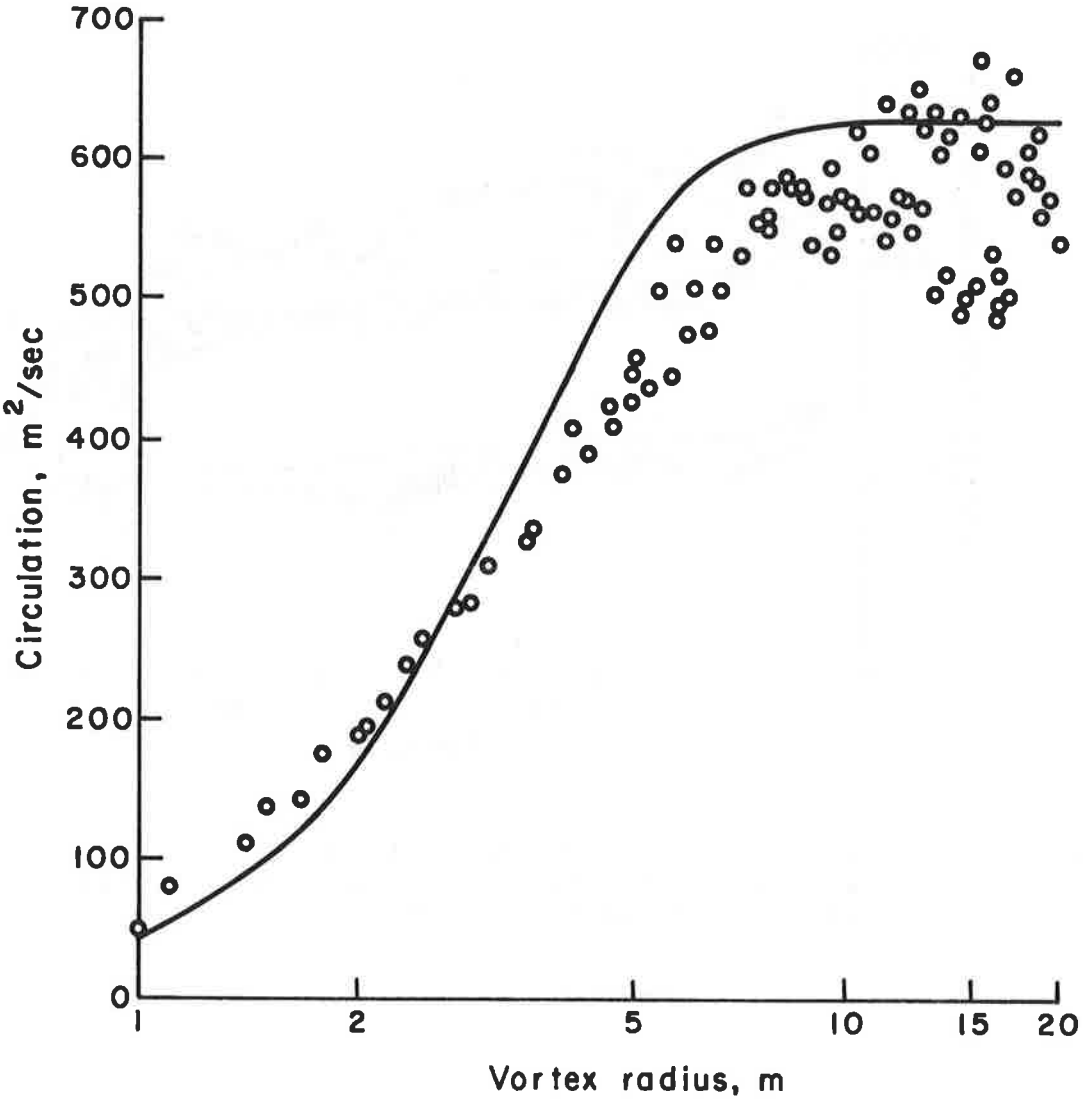

Figure 5-7a. Comparison between measured and calculated initial circulation at 11 sec after aircraft passage.

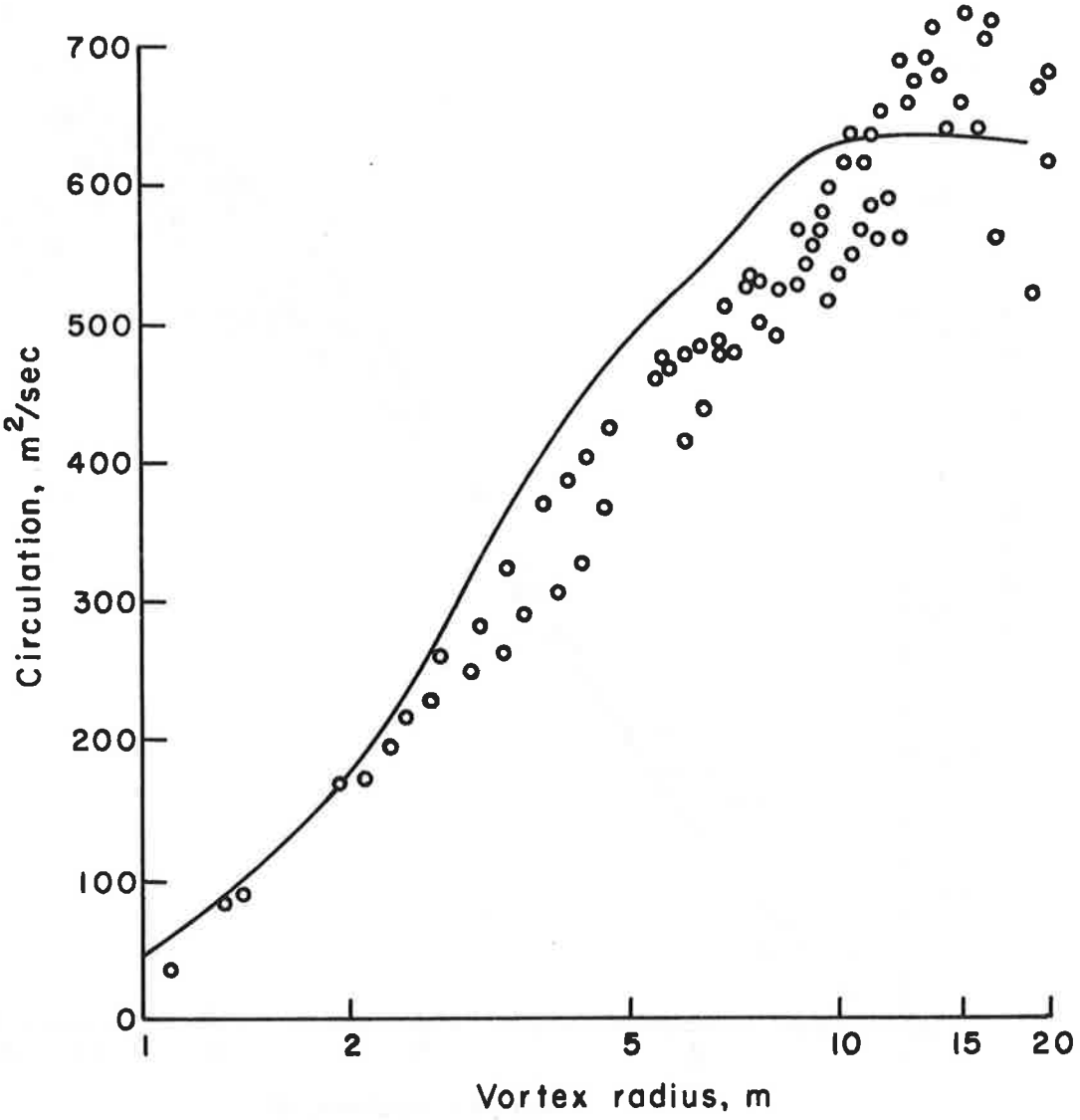

Figure 5-7b. Comparison between measured and calculated circulation at 18 sec after aircraft passage.

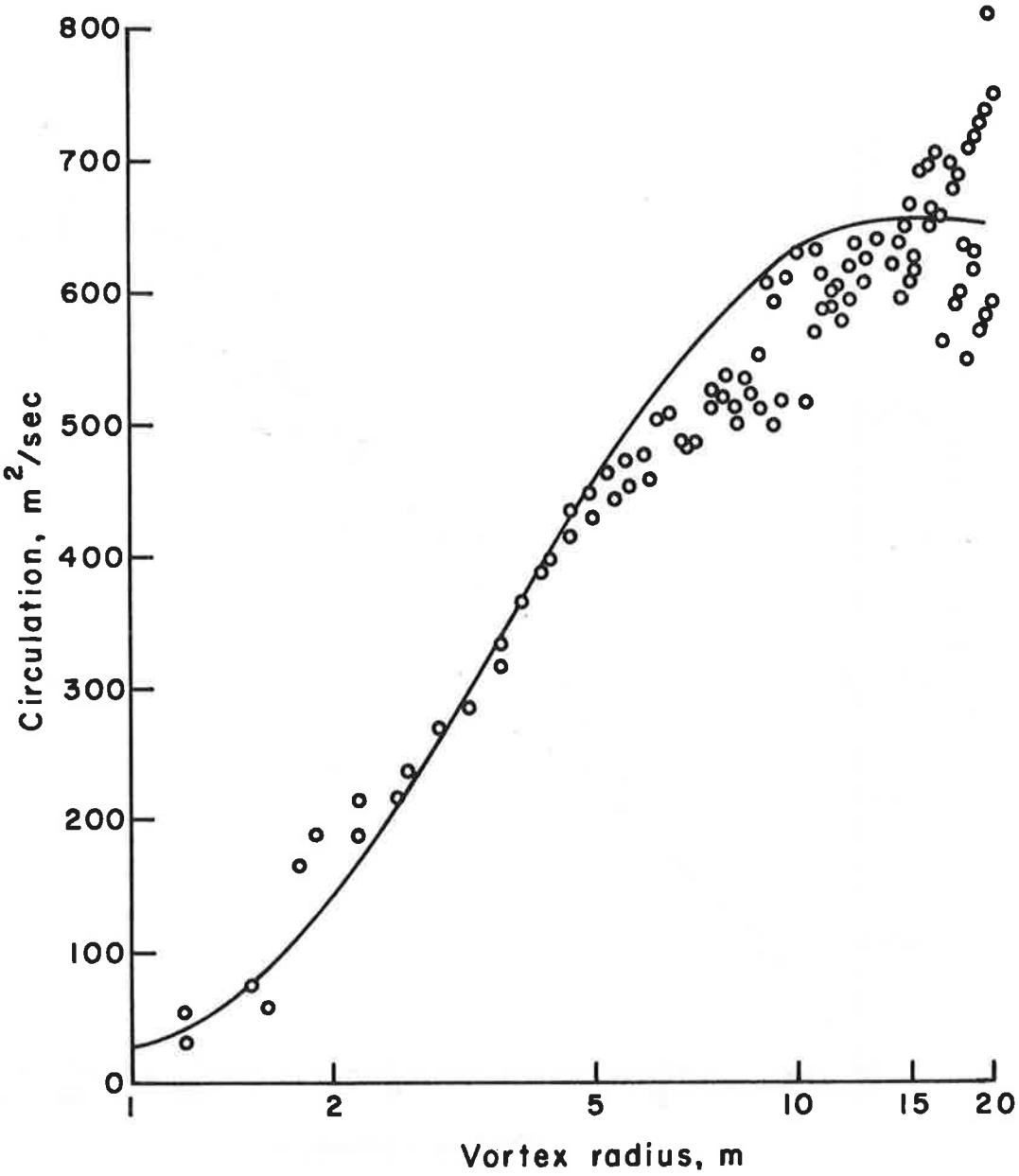

Figure 5-7c. Comparison between measured and calculated circulation at 25 sec after aircraft passage.

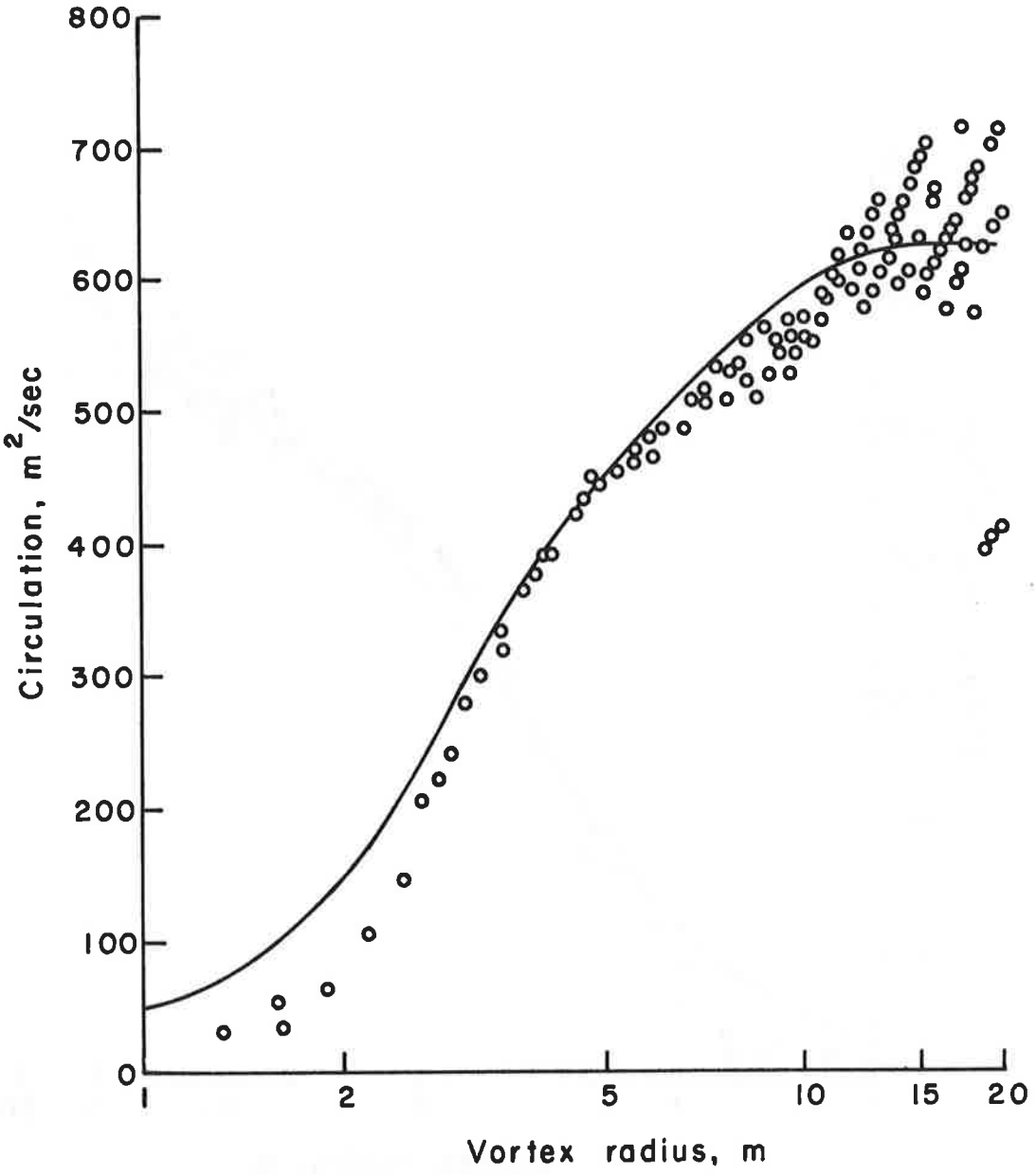

Figure 5-7d. Comparison between measured and calculated circulation at 39 sec after aircraft passage.

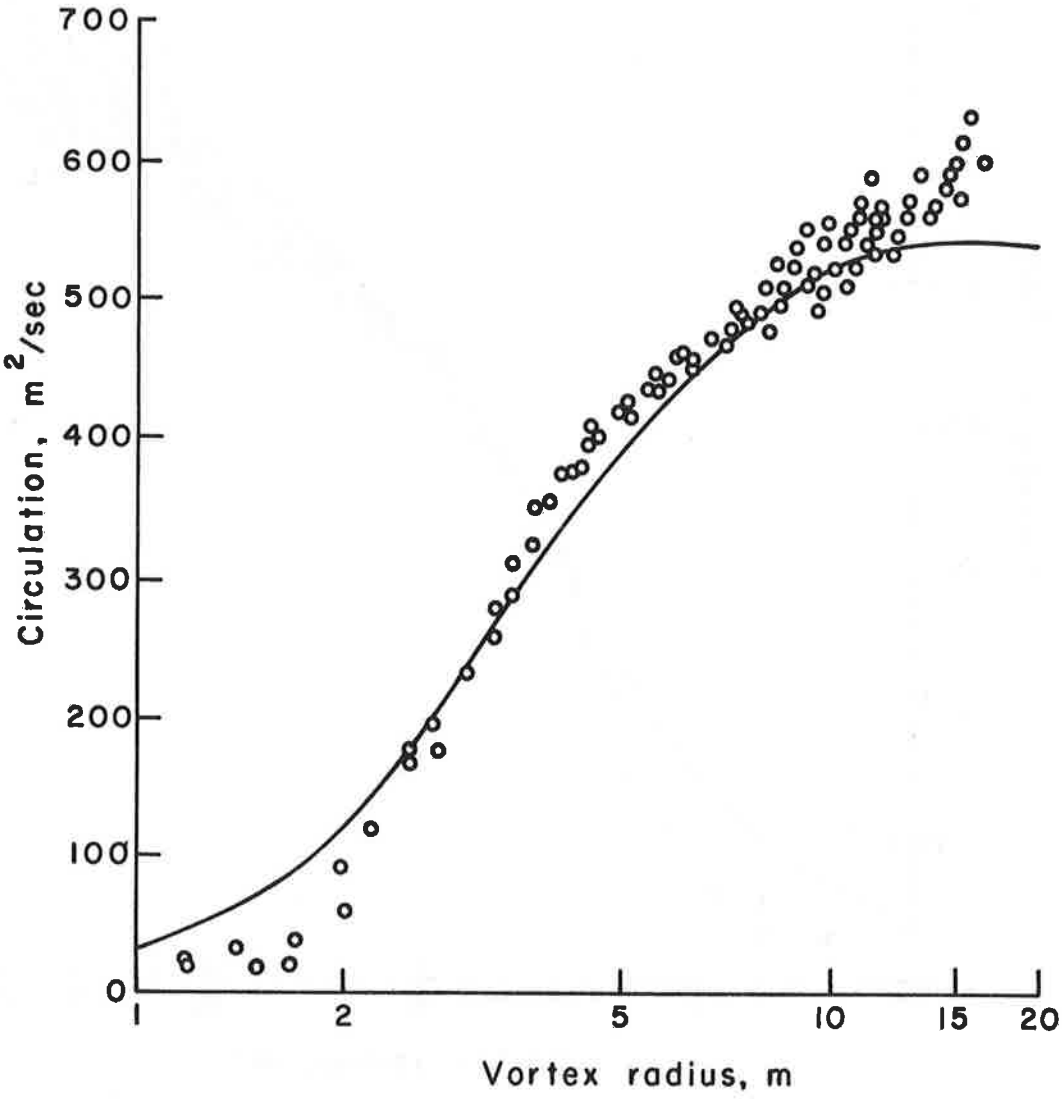

Figure 5-7e. Comparison between measured and calculated circulation at 55 sec after aircraft passage.

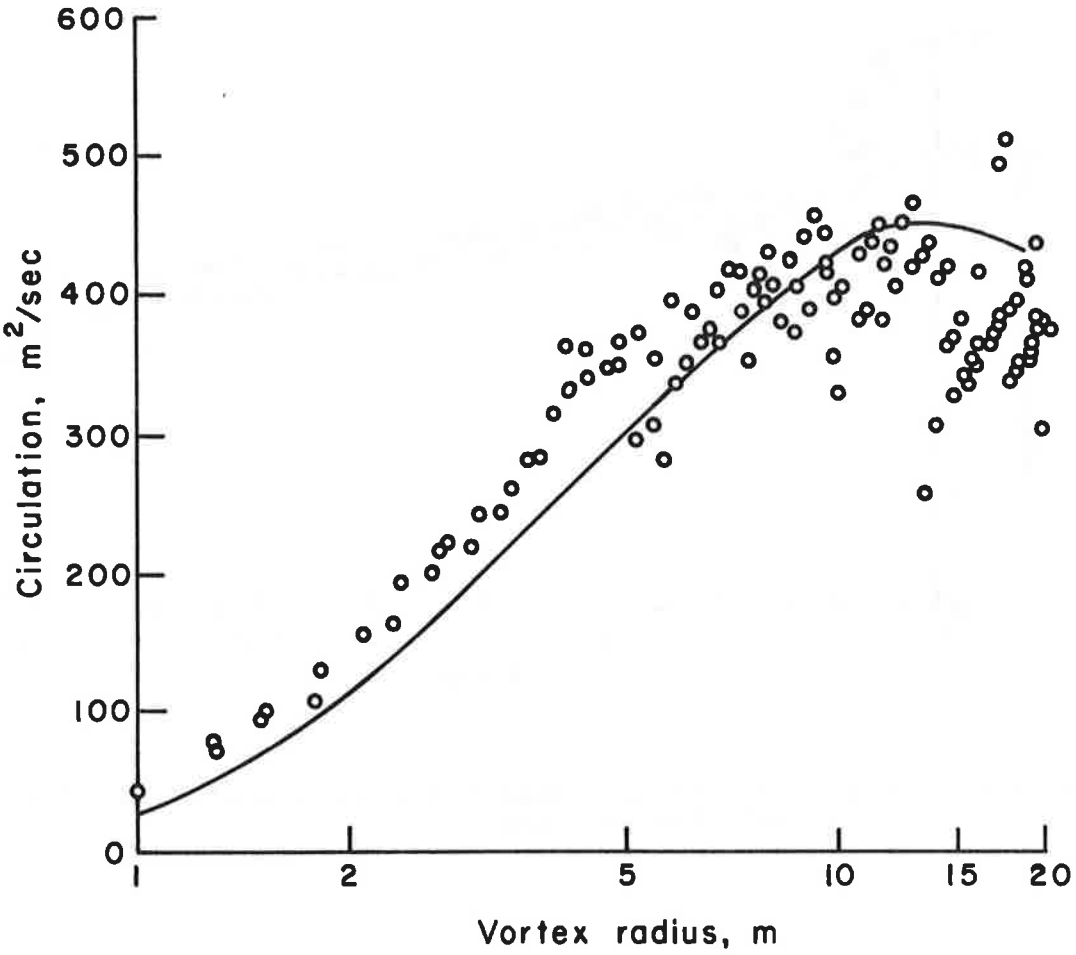

Figure 5-7f. Comparison between measured and calculated circulation at 76 sec after aircraft passage.

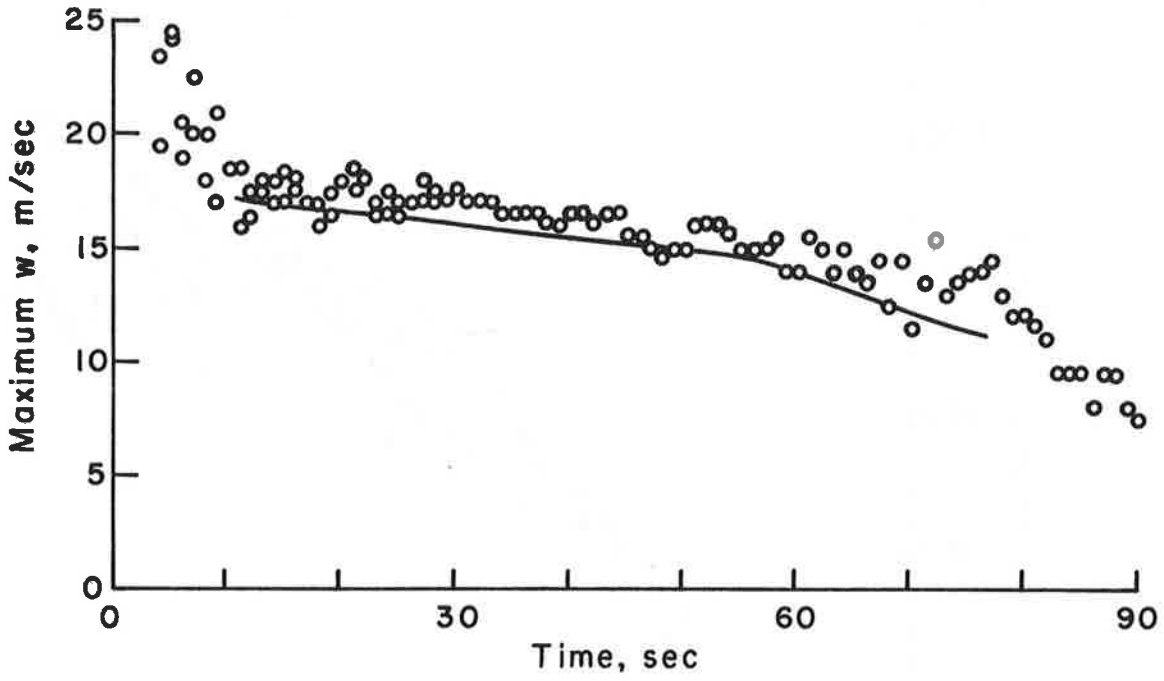

Figure 5-8. Comaprison between measured and calculated maximum swirl velocity vs. time.

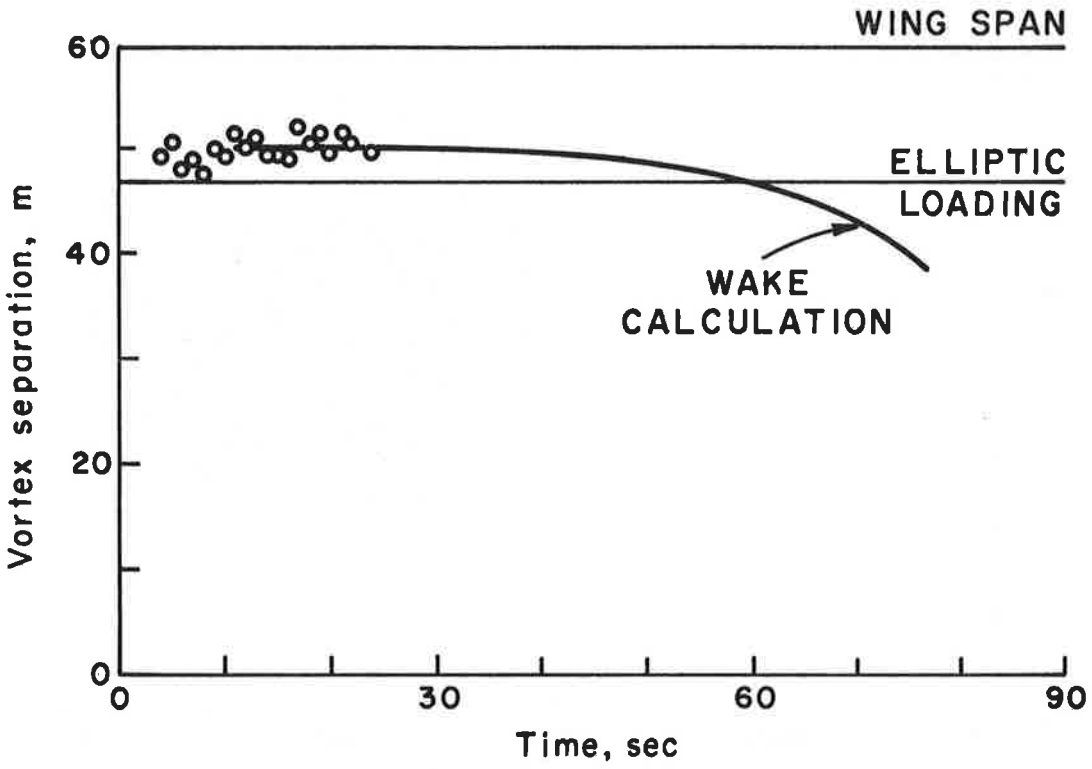

Figure 5-9. Measured and calculated vortex-pair separation vs. time.

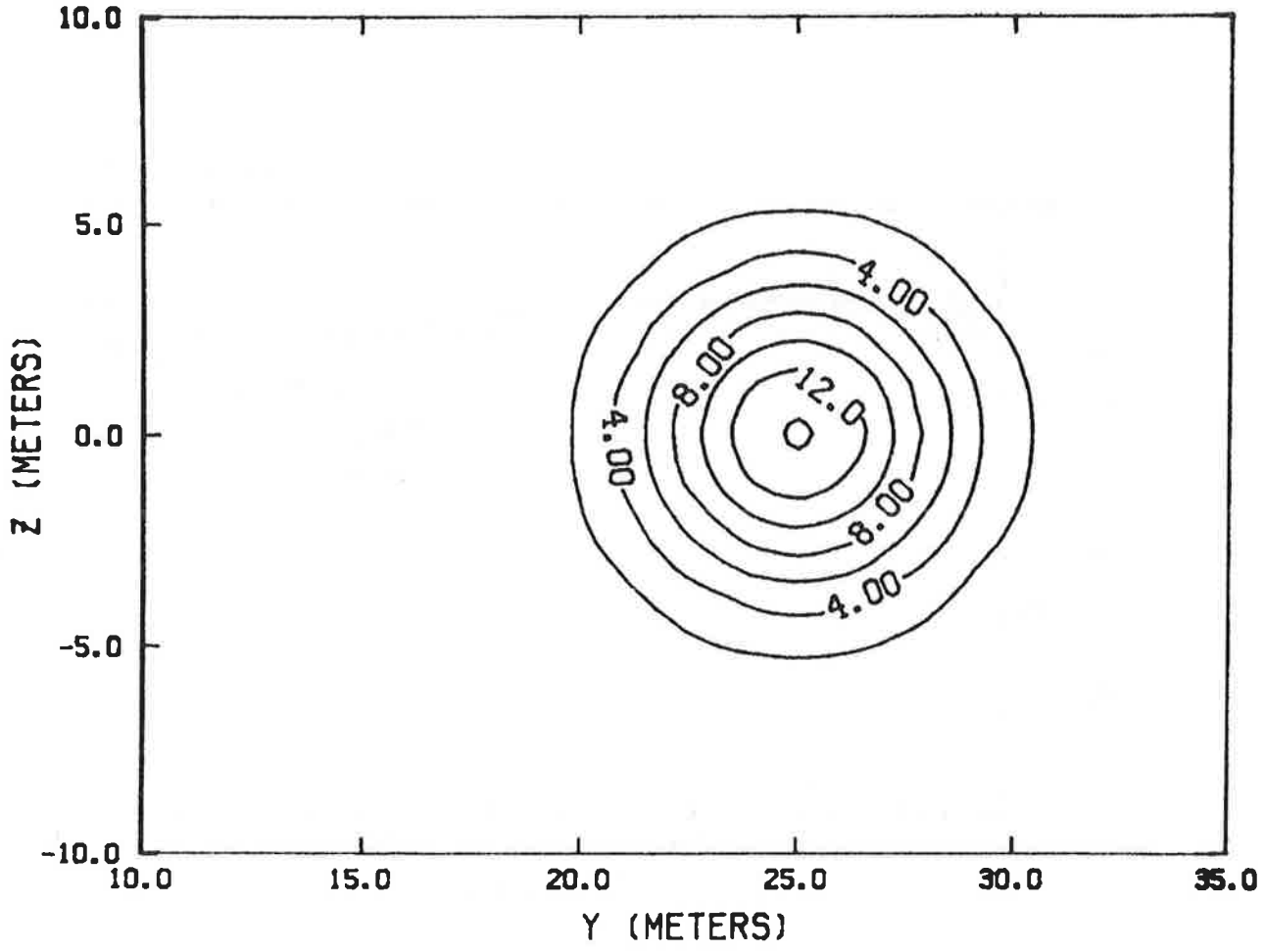

Figure 5-10a. Contours of vorticity in the core region at 11 sec. Contour interval 2 sec^{-1}.

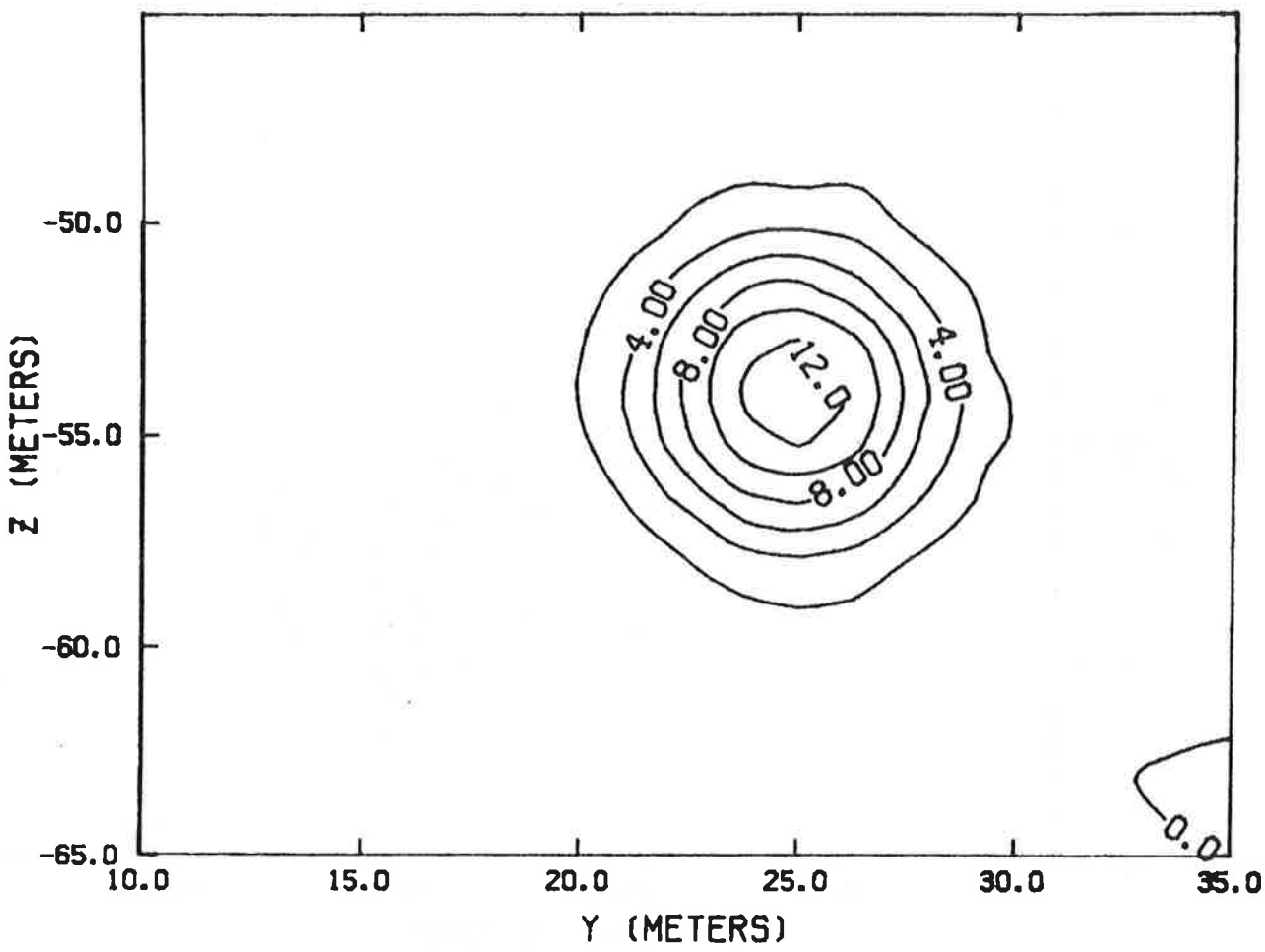

Figure 5-10b. Contours of vorticity in the core region at 39 sec. Contour interval 2 sec^{-1}.

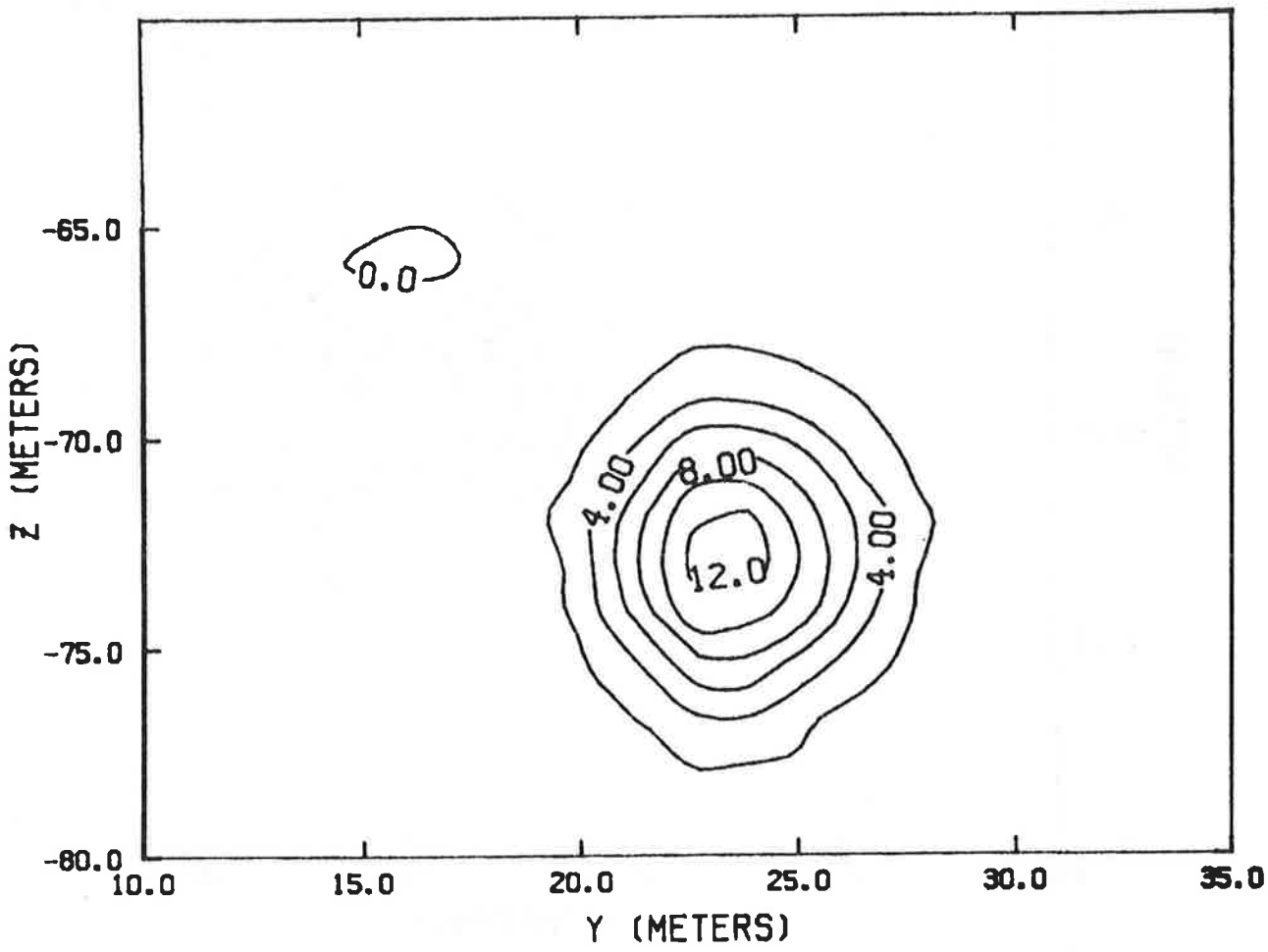

Figure 5-10c. Contours of vorticity in the core region at 55 sec. Contour interval 2 sec^{-1}.

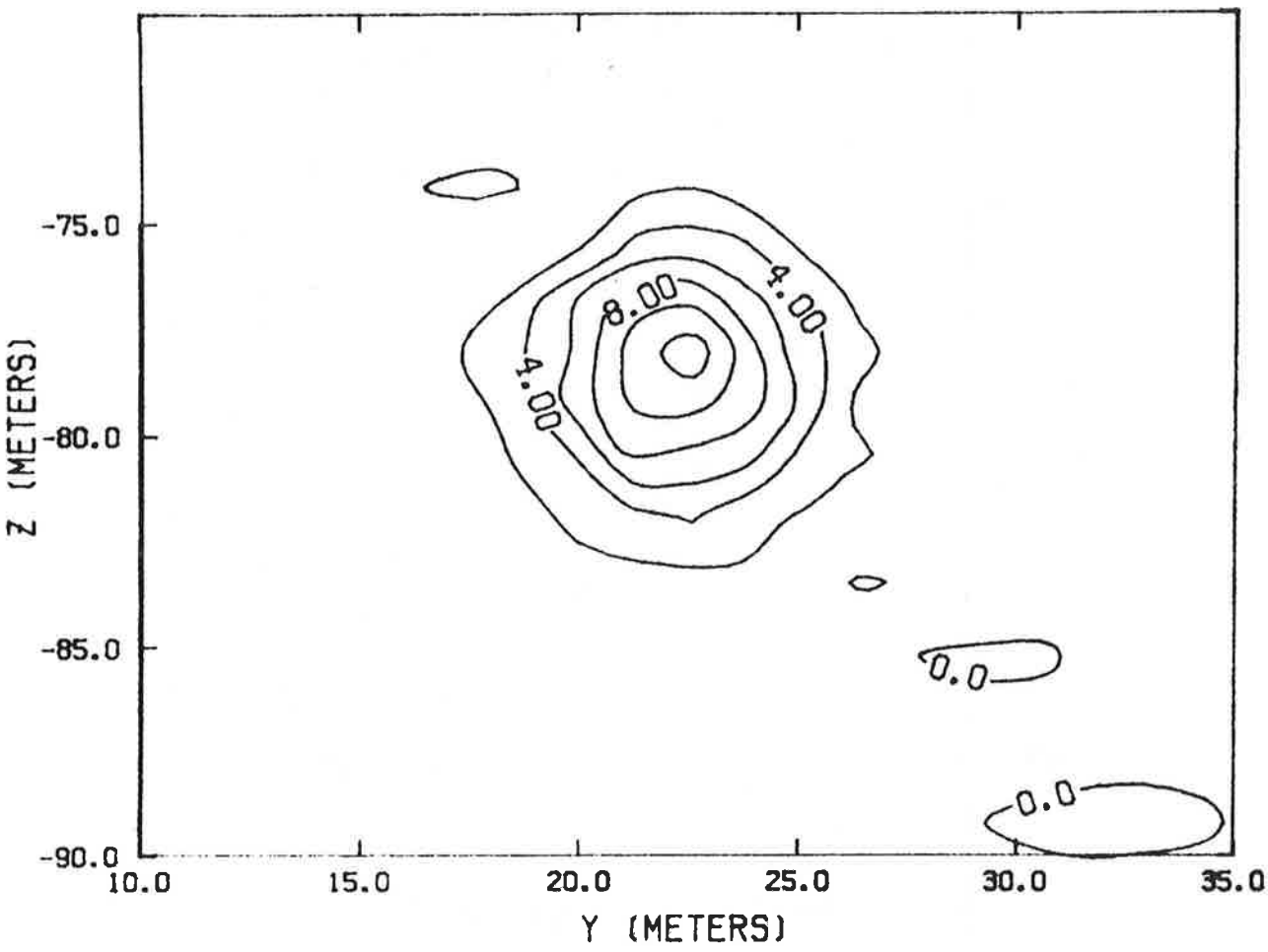

Figure 5-10d. Contours of vorticity in the core region at 65 sec. Contour interval 2 sec^{-1}.

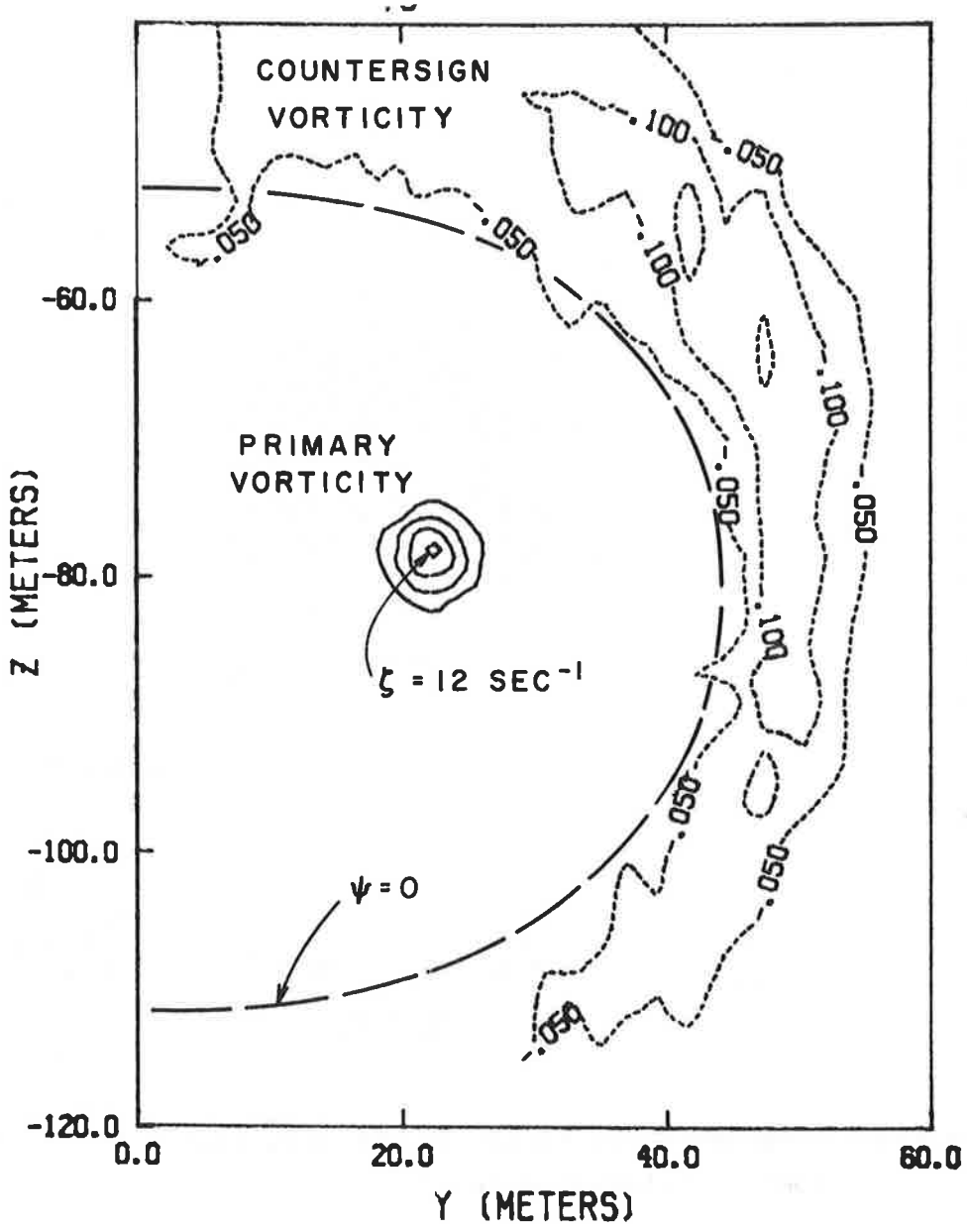

Figure 5-11. Contours of primary and countersign vorticity at 65 sec. Contour interval equal to 3.0 sec^{-1} for primary vorticity (——), and 0.05 sec^{-1} countersign vorticity (----).

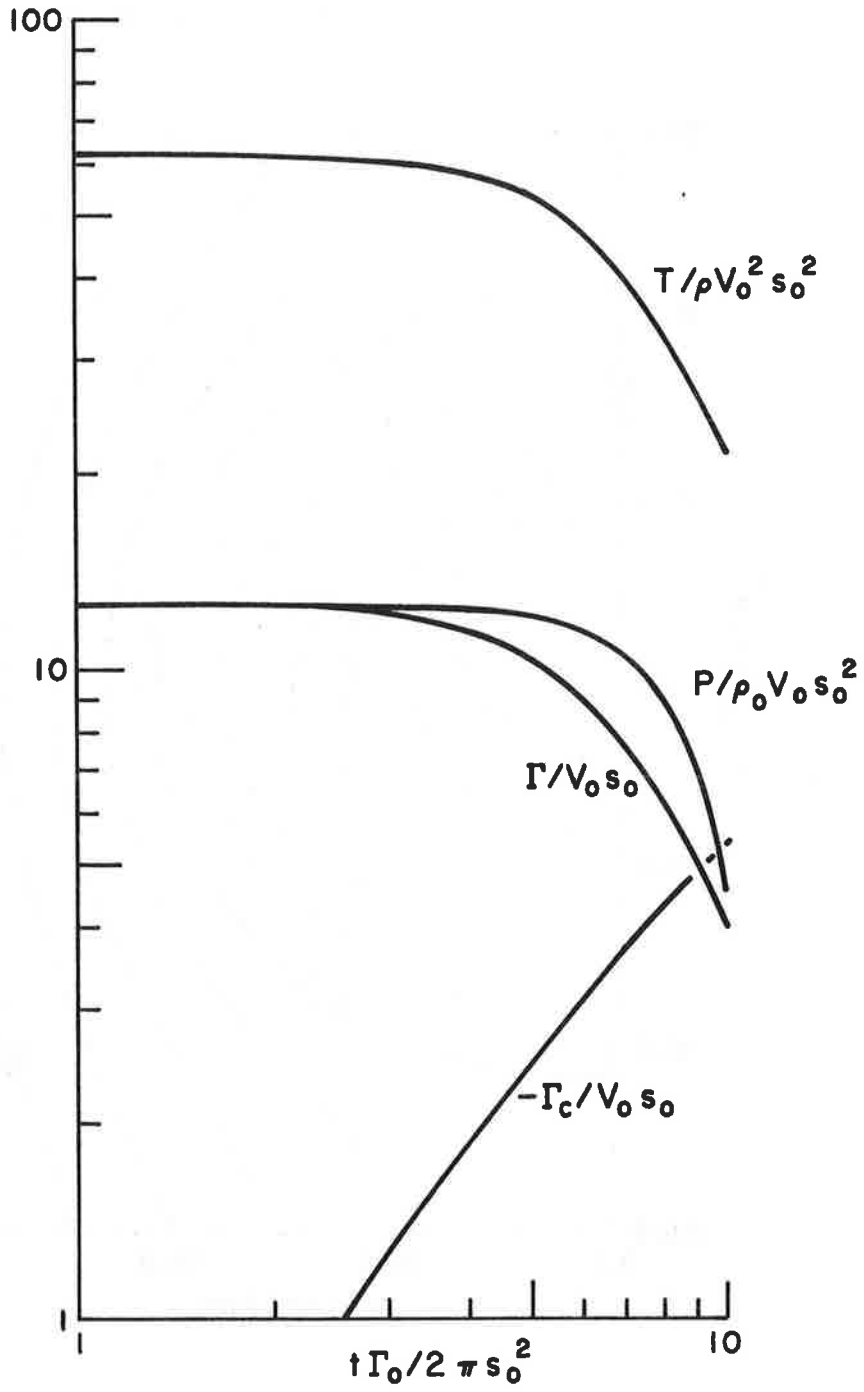

Figure 5-12. Calculated non-dimensional kinetic energy, impulse, total circulation, and integrated countersign vorticity, Γ_c.

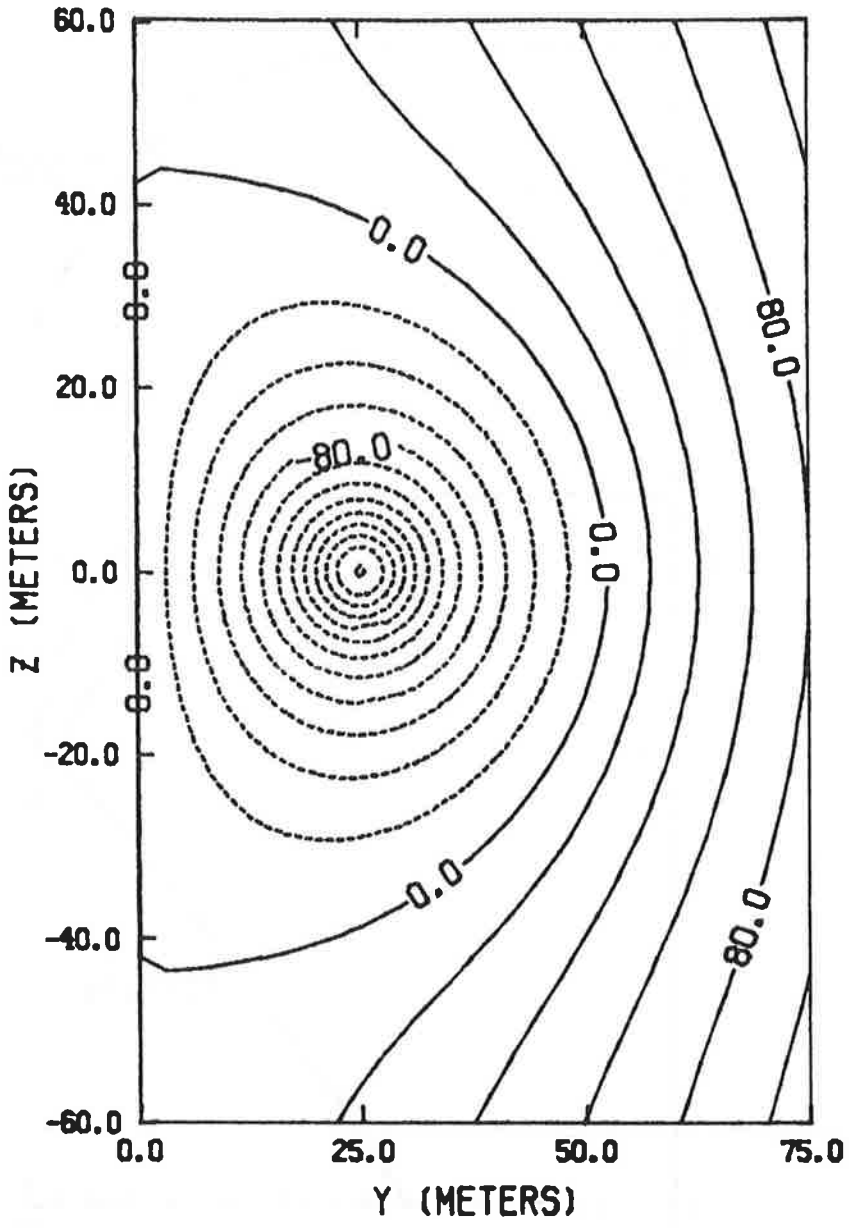

Figure 5-13a. Streamline pattern at 11 sec. Contour interval of 20 m^2/sec. Descent velocity = 2.0 m/sec.

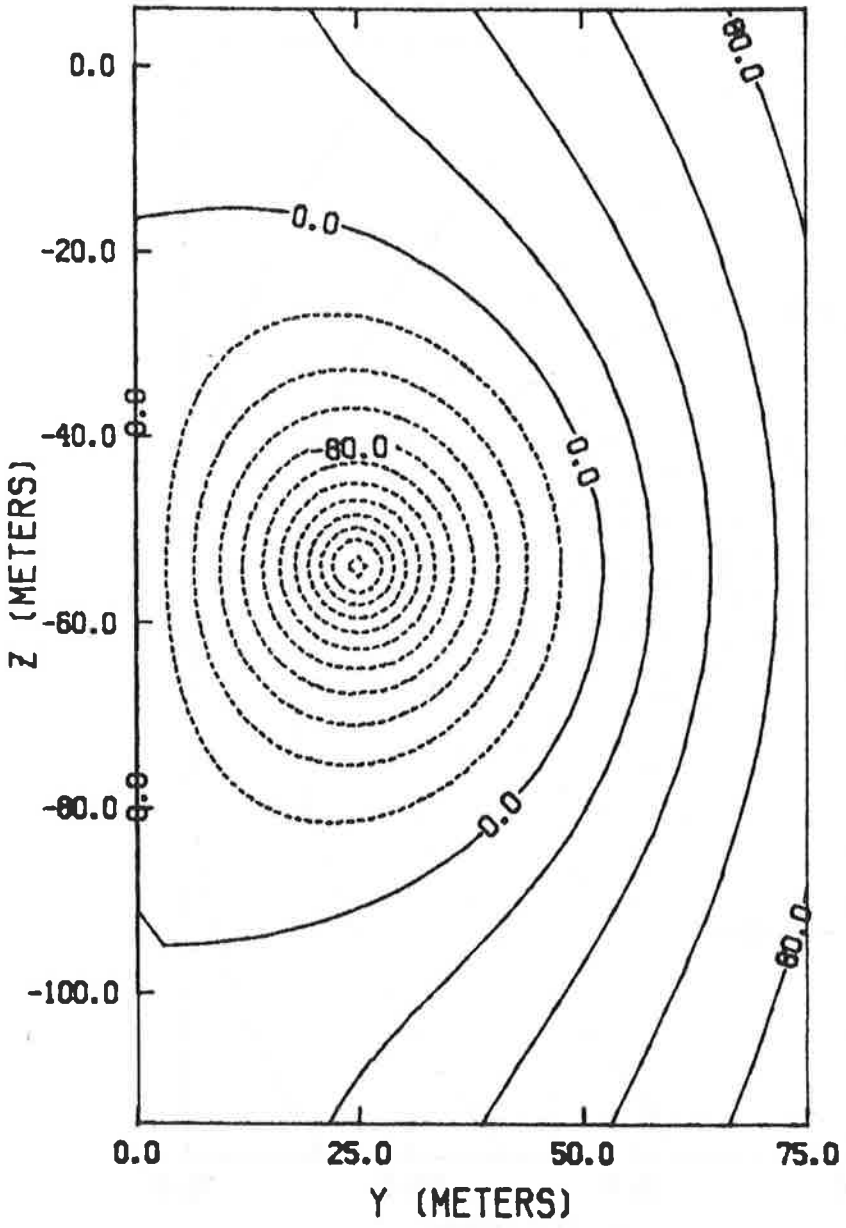

Figure 5-13b. Streamline pattern at 39 sec. Contour interval of 20 m^2/sec. Descent velocity = 1.96 m/sec.

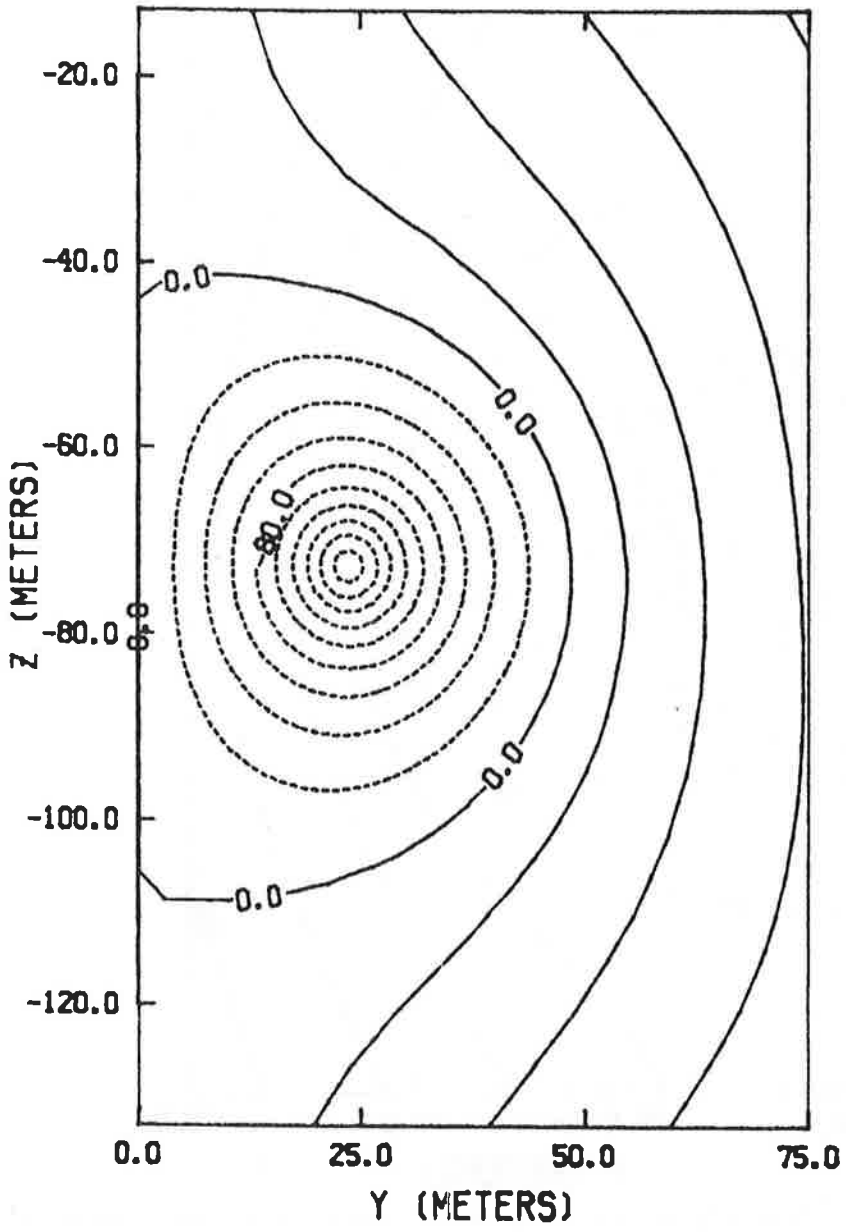

Figure 5-13c. Streamline pattern at 55 sec. Contour interval of 20 m^2/sec. Descent velocity = 0.76 m/sec.

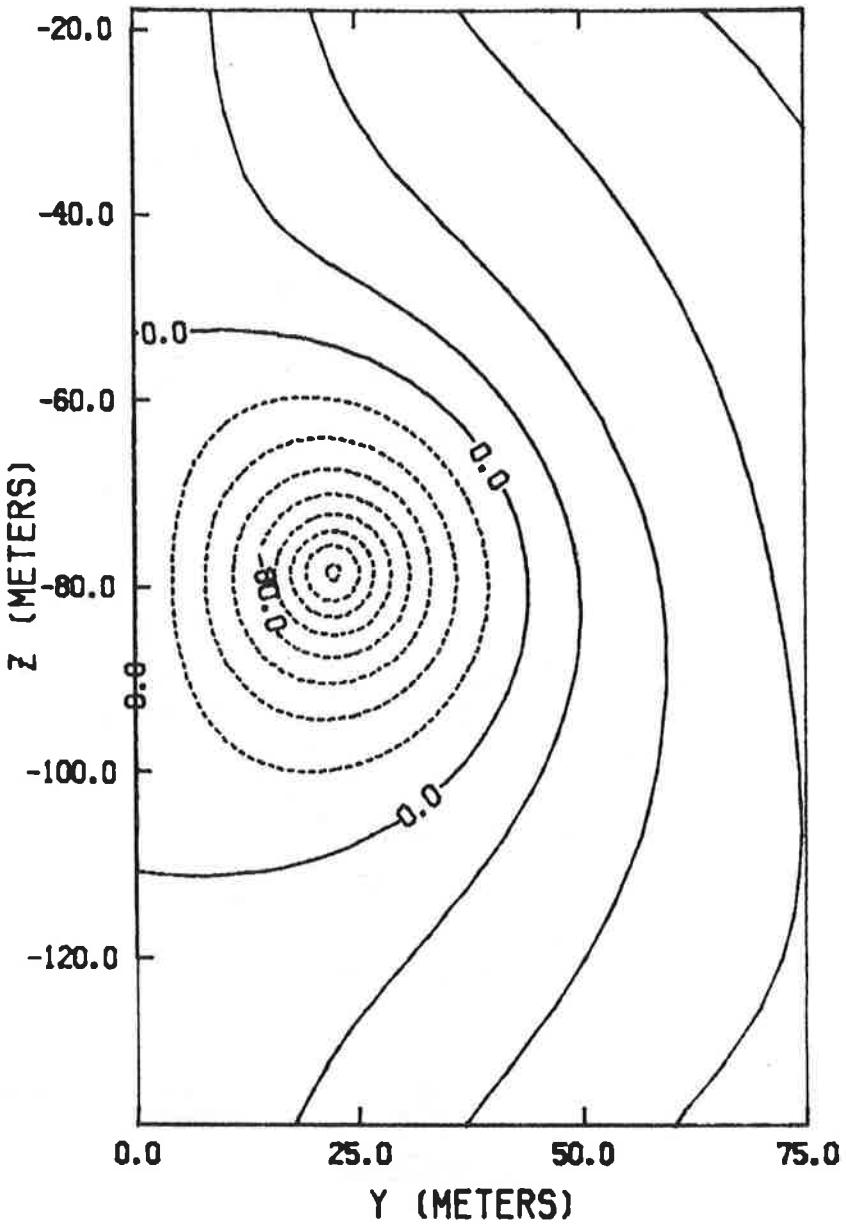

Figure 5-13d. Streamline pattern at 65 sec. Contour interval of 20 m^2/sec. Descent velocity = 0.4 m/sec.

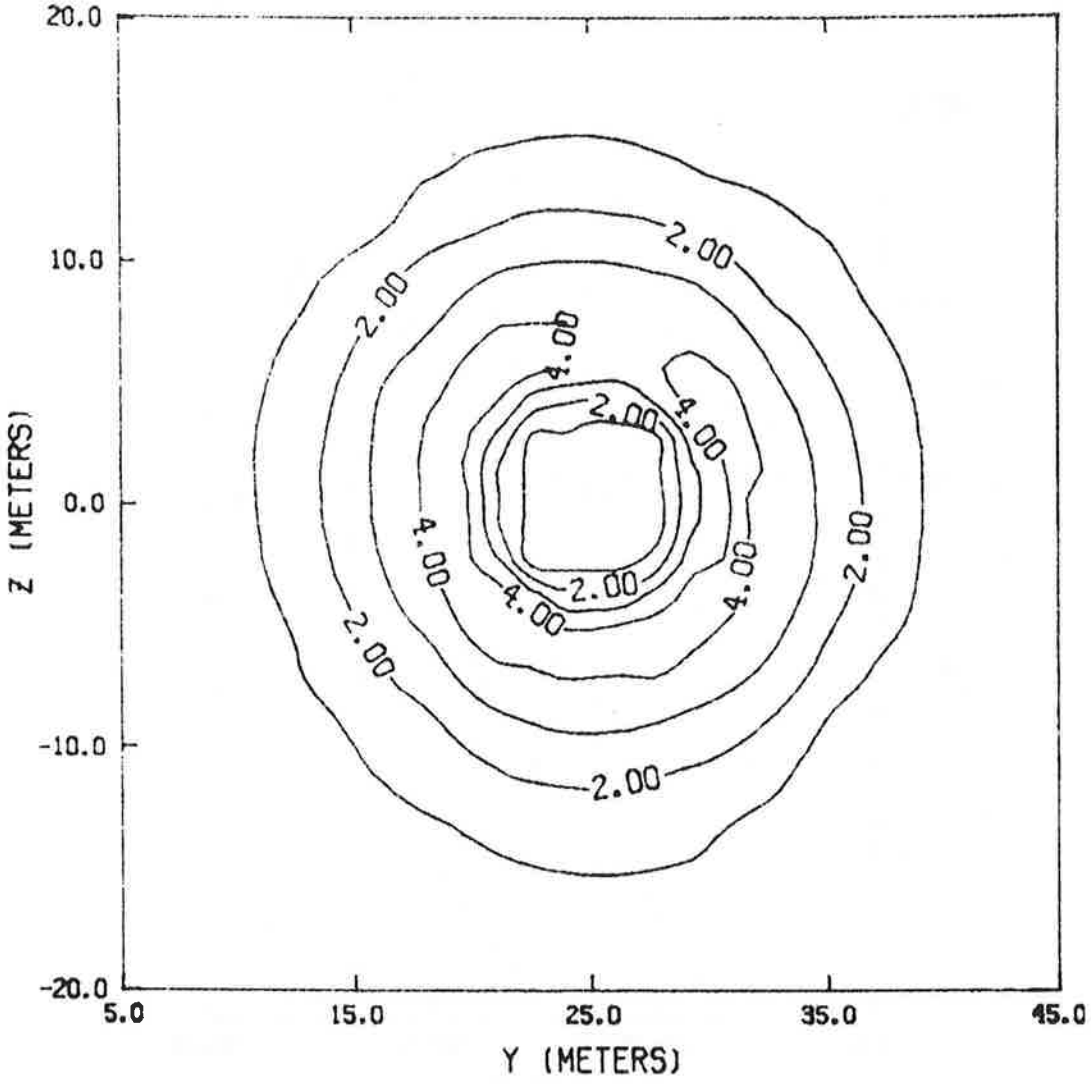

Figure 5-14a. Contours of turbulence at 18 sec. Contour interval 1 m^2/sec^2.

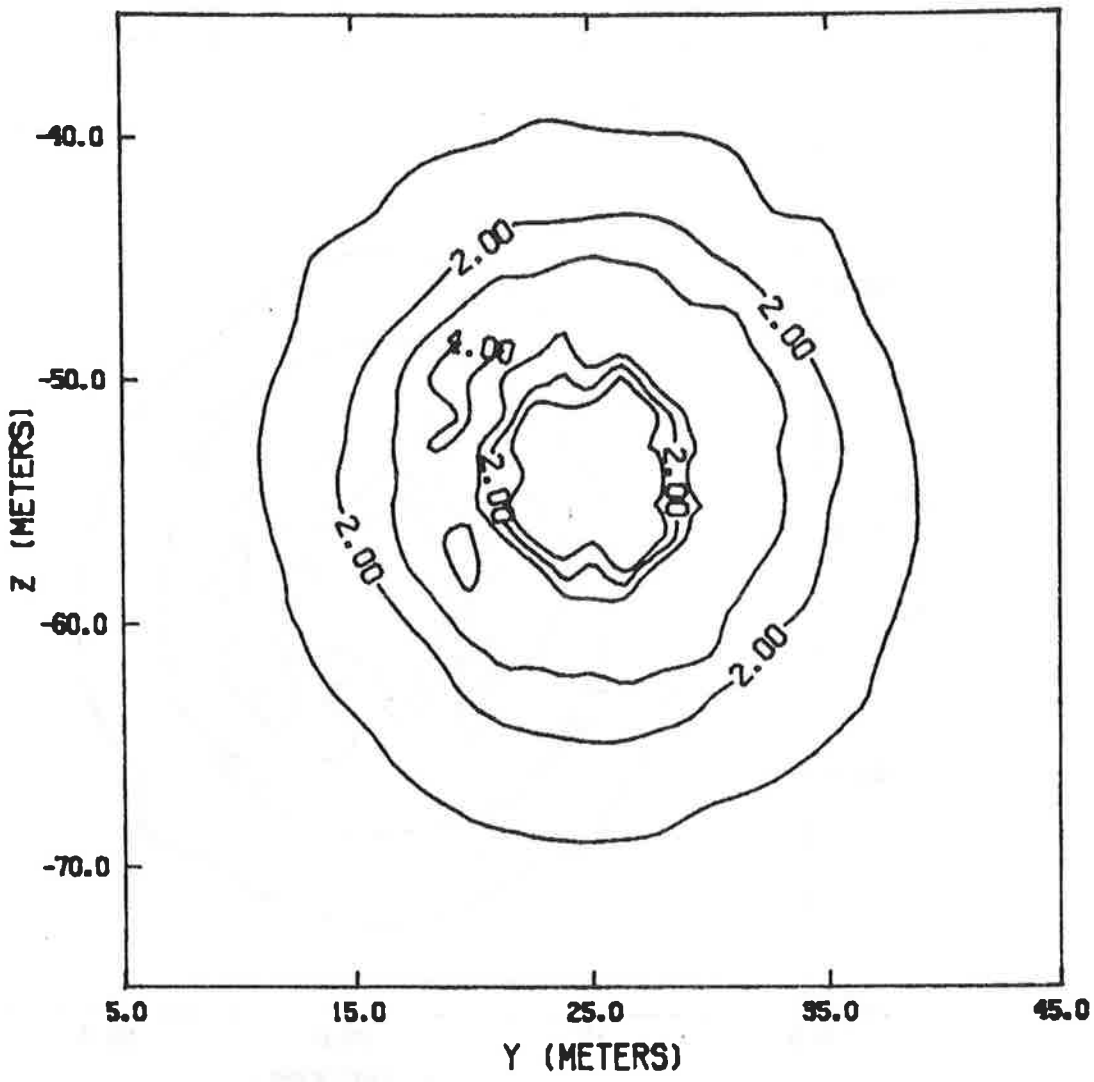

Figure 5-14b. Contours of turbulence at 39 sec. Contour interval 1 m^2/sec^2.

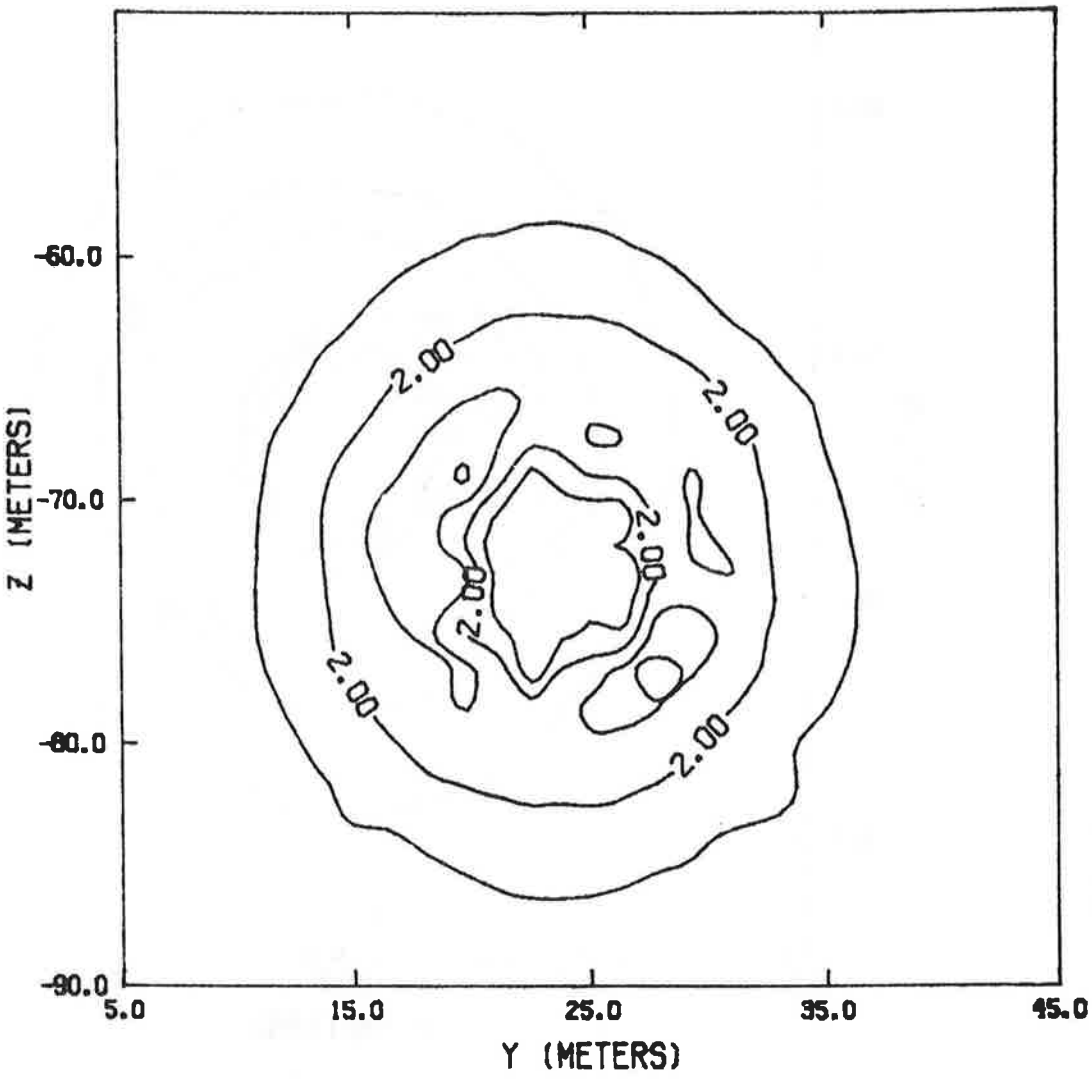

Figure 5-14c. Contours of turbulence at 55 sec. Contour interval 1 m^2/sec^2.

6. DISCUSSION AND CONCLUSIONS

6.1 DISCUSSION

In this study, we have closely simulated the behavior of a turbulent vortex descending in a stable density stratification, showing agreement between the calculated and observed behavior.

What we find is a very strong, tight vortex which decays slowly during descent, and which has appreciable strength after it has stopped descending. This investigation suggests that the core vorticity structure remains well ordered throughout most of the descent, while the vorticity within the core is slowly diffused outward due to a ring of turbulence surrounding the core. The turbulence reaches a peak at a point about twice the radius of maximum tangential velocity. A portion of the vorticity diffused away from the core is annihilated by countersign vorticity generated at the boundary of the recirculation cell, part of which is itself diffused inward toward the core by the turbulence generated at the cell boundary. The countersign vorticity remains small, less than 1 percent of the magnitude of the maximum core vorticity, because it is being continually diffused into the cell or swept out of the vicinity of the cell by descent. Although the level of the countersign vorticity is small, the area of the wake containing it reaches an area comparable with that of the recirculation cell. The location of the countersign vorticity is primarily above and outboard of the cores. This will tend to drive the cores together, which is seen in Figure 5-9, but the net effect of the strength and location of the countersign vorticity with respect to the cores is to halt descent. The circulation of the countersign vorticity reaches a magnitude of nearly 50 percent of the circulation of the initial primary vorticity, while the primary vorticity is reduced by only about 20 percent below its initial value at the end of descent. The cores, then, remain very strong, and a vortex pair cannot be assumed to have dissipated when it stops descending.

The turbulence near the center of the core is repressed due to the stability of the flow in this region, and remains small over the descent time time of the pair. It reaches a level of only 10 percent of the peak value outside the core, accounting for the persistence of the vortices. However, the rate of annihilation of vorticity, and the extent and strength of the countersign vorticity, are direct consequences of the turbulent diffusion process.

The effect of stable atmospheric stratification, then, is found to halt descent, but not necessarily to completely disorganize the vortex pair. Increasing the stable stratification would decrease the total descent distance, although no quantitative statement is possible here since we have analyzed a single stratification condition. In Ref. 13 the descent distances of vortices having considerably less strength than analyzed here were found to be directly proportional to Froude number. This may not be indicative of the behavior of stronger vortices, however.

6.2 CONCLUSIONS

The results of this study may be summarized as follows:

a) Turbulence effects must be accounted for to arrive at an accurate picture of vortex-pair behavior in a stratified flow.

b) Unalleviated vortices remain strong during descent due to suppression of turbulence within their cores.

c) The vortices stop descending due to a diffuse region of stratification-produced countersign vorticity primarily outboard and above the cores.

d) The core separation does not control the descent velocity to the extent predicted by several previous investigators.

APPENDIX A
SECOND-ORDER CLOSURE MODELED EQUATIONS

A.1. EQUATIONS IN AXISYMMETRIC COORDINATES

The modeled axisymmetric equations of motion for the mean variables and turbulent correlations (denoted by < >) may be written as follows. The tilde indicates variables that have normalized by r to insure analyticity at $r = 0$.

$$\frac{D\tilde{\zeta}}{Dt} = \frac{1}{r}\frac{g}{\rho_o}\frac{\partial \rho}{\partial r} - \frac{1}{r}\frac{\partial}{\partial r}\left\{\frac{\partial \langle uu\rangle}{\partial z} - \frac{1}{r}\frac{\partial}{\partial r}\, r^2\langle \tilde{u}\tilde{w}\rangle\right\} - \frac{\partial}{\partial z}$$

$$\left\{\frac{\partial \langle \widetilde{uw}\rangle}{\partial z} - \frac{1}{r}\frac{\partial \langle ww\rangle}{\partial r} + \frac{1}{r^2}\left(\langle uu\rangle - \langle vv\rangle\right)\right\}$$

$$+ \nu\left\{\frac{1}{r}\frac{\partial}{\partial r}\, r\,\frac{\partial \tilde{\zeta}}{\partial r} + \frac{\partial^2}{\partial z^2}\,\tilde{\zeta} + \frac{2}{r}\frac{\partial \tilde{\zeta}}{\partial r}\right\} \quad . \tag{A.1}$$

$$\frac{D\rho}{Dt} = -\frac{1}{r}\frac{\partial}{\partial r}\left(r^2\langle \widetilde{u\rho}\rangle\right) - \frac{\partial}{\partial z}\langle w\rho\rangle + \nu\left\{\frac{1}{r}\frac{\partial}{\partial r}\, r\,\frac{\partial \rho}{\partial r} + \frac{\partial}{\partial z}\frac{\partial \rho}{\partial z}\right\} . \tag{A.2}$$

$$\frac{D\langle uu\rangle}{Dt} = -2r\langle uu\rangle\frac{\partial \tilde{u}}{\partial r} - 2r^2\langle \widetilde{uw}\rangle\frac{\partial \tilde{u}}{\partial z} - 2\langle uu\rangle\,\tilde{u} - \frac{q}{\Lambda}\left[\langle uu\rangle - \frac{q^3}{3}\right]$$

$$- \frac{2bq^3}{3\Lambda} + L(\langle uu\rangle) - \frac{2}{r^2}\left(\nu + v_c q\Lambda\right)\left(\langle uu\rangle - \langle vv\rangle\right)$$

$$- \frac{2a\nu}{\Lambda^2}\langle uu\rangle \quad . \tag{A.3}$$

$$\frac{D(\langle uu\rangle - \langle vv\rangle)}{Dt} = -2r\langle uu\rangle \frac{\partial \tilde{u}}{\partial r} - 2r^2\langle \widetilde{uw}\rangle \frac{\partial \tilde{u}}{\partial z} - \left\{\frac{4}{r^2}(\nu + v_c q\Lambda) + 2\tilde{u} + \frac{q}{\Lambda} + \frac{2a\nu}{\Lambda^2}\right\}(\langle uu\rangle - \langle vv\rangle) + L(\langle uu\rangle - \langle vv\rangle) \quad . \tag{A.4}$$

$$\frac{D\langle ww\rangle}{Dt} = -2r\langle \widetilde{uw}\rangle \frac{\partial w}{\partial r} - 2\langle ww\rangle \frac{\partial w}{\partial z} - \frac{q}{\Lambda}\left[\langle ww\rangle - \frac{q^2}{3}\right] - \frac{2a\nu}{\Lambda^2}\langle ww\rangle - \frac{2bq^3}{3\Lambda} - \frac{2g}{\rho_o}\langle w\rho\rangle + L(\langle ww\rangle) \quad . \tag{A.5}$$

$$\frac{D\langle uv\rangle}{Dt} = -2\langle uv\rangle \tilde{u} - r\langle uv\rangle \frac{\partial \tilde{u}}{\partial r} - r^2\langle \widetilde{vw}\rangle \frac{\partial \tilde{u}}{\partial z} - \frac{q}{\Lambda}\langle uv\rangle + L(\langle uv\rangle) - \frac{2a\nu}{\Lambda^2}\langle uv\rangle - \frac{4}{r^2}(\nu + v_c q\Lambda)\langle uv\rangle \quad . \tag{A.6}$$

$$\frac{D\langle \widetilde{uw}\rangle}{Dt} = -\frac{\langle uu\rangle}{r}\frac{\partial w}{\partial r} - \langle ww\rangle \frac{\partial \tilde{u}}{\partial z} - \frac{q}{\Lambda}\langle \widetilde{uw}\rangle - \frac{g}{\rho_o}\langle \widetilde{u\rho}\rangle + L(\langle \widetilde{uw}\rangle) - \frac{2a\nu}{\Lambda^2}\langle \widetilde{uw}\rangle + \frac{1}{r}\frac{\partial}{\partial r}\left\{\nu + v_c q\Lambda\ \langle \widetilde{uw}\rangle\right\} + \frac{(\nu + v_c q\Lambda)}{r}\frac{\partial\langle \widetilde{uw}\rangle}{\partial r} \quad . \tag{A.7}$$

$$\frac{D\widetilde{<vw>}}{Dt} = - 2\widetilde{<vw>}\,\tilde{u} - \frac{<uv>}{r}\frac{\partial w}{\partial r} - \widetilde{<vw>}\frac{\partial w}{\partial z} - \frac{q}{\Lambda}\widetilde{<vw>} - \frac{g}{\rho_o}\widetilde{<v\rho>}$$

$$+ L(\widetilde{<vw>} - \frac{2a\nu}{\Lambda^2}\widetilde{<vw>} + \frac{1}{r}\frac{\partial}{\partial r}\left\{(\nu + v_c q\Lambda)\ \widetilde{<vw>}\right\}$$

$$+ \frac{(\nu + v_c q\Lambda)}{r}\frac{\partial\widetilde{<vw>}}{\partial r} \quad . \tag{A.8}$$

$$\frac{D\widetilde{<u\rho>}}{Dt} = - \frac{\widetilde{<u\rho>}}{r}\frac{\partial r^2\tilde{u}}{\partial r} - <w\rho>\frac{\partial\tilde{u}}{\partial z} - \frac{<uu>}{r}\frac{\partial\rho}{\partial r} - \widetilde{<uw>}\frac{\partial\rho}{\partial z} - \frac{Aq}{\Lambda}\widetilde{<u\rho>}$$

$$+ L(\widetilde{<u\rho>}) + \frac{1}{r}\frac{\partial}{\partial r}\left\{(\nu + v_c q\Lambda)\ \widetilde{<u\rho>}\right\} +$$

$$\frac{(\nu + v_c q\Lambda)}{r} \qquad \frac{\partial\widetilde{<u\rho>}}{\partial r} - \frac{a\nu\widetilde{<u\rho>}}{\Lambda^2} \quad . \tag{A.9}$$

$$\frac{D\widetilde{<v\rho>}}{Dt} = - 2\widetilde{<v\rho>}\,\tilde{u} - \frac{<uv>}{r}\frac{\partial\rho}{\partial r} - \widetilde{<vw>}\frac{\partial\rho}{\partial z} - \frac{Aq}{\Lambda}\widetilde{<v\rho>} + L(\widetilde{<v\rho>})$$

$$- \frac{a\nu\widetilde{<v\rho>}}{\Lambda^2} + \frac{1}{r}\frac{\partial}{\partial r}\left\{(\nu + v_c q\Lambda)\ \widetilde{<v\rho>}\right\} +$$

$$\frac{(\nu + v_c q\Lambda)}{r} \quad \frac{\partial\widetilde{<v\rho>}}{\partial r} \quad . \tag{A.10}$$

$$\frac{D<w\rho>}{Dt} = - r\widetilde{<u\rho>}\frac{\partial w}{\partial r} - <w\rho>\frac{\partial w}{\partial z} - r\widetilde{<uw>}\frac{\partial\rho}{\partial r} - <ww>\frac{\partial\rho}{\partial z} - \frac{g}{\rho_o}<\rho^2>$$

$$- \frac{Aq}{\Lambda}<w\rho> + L(<w\rho>) - \frac{a\nu<w\rho>}{\Lambda^2} \quad . \tag{A.11}$$

$$\frac{D\langle\rho^2\rangle}{Dt} = -2r\langle\widetilde{u\rho}\rangle \frac{\partial\rho}{\partial r} - 2\langle w\rho\rangle \frac{\partial\rho}{\partial z} - \frac{2bsq}{\Lambda}\langle\rho^2\rangle + L(\langle\rho^2\rangle)$$

$$- \frac{2as\nu\langle\rho^2\rangle}{\Lambda^2} \quad . \tag{A.12}$$

$$\frac{Dq^2}{Dt} = -2r\langle uv\rangle \frac{\partial\tilde{u}}{\partial r} - 2r^2\langle\widetilde{uw}\rangle \frac{\partial\tilde{u}}{\partial z} - 2\langle uu\rangle \tilde{u} - 2\langle\widetilde{vv}\rangle \tilde{u}$$

$$- 2r\langle\widetilde{uw}\rangle \frac{\partial w}{\partial r} - 2\langle ww\rangle \frac{\partial w}{\partial z} - \frac{2g}{\rho}\langle w\rho\rangle - \frac{2bq^3}{\Lambda}$$

$$+ L(q^2) - \frac{2a\nu}{\Lambda^2} q^2 \quad . \tag{A.13}$$

$$\frac{D\Lambda}{Dt} = -s_1 \frac{\Lambda}{q^2}\left[r\langle uu\rangle \frac{\partial\tilde{u}}{\partial r} + r^2\langle\widetilde{uw}\rangle \frac{\partial\tilde{u}}{\partial z} + (\langle uu\rangle + \langle vv\rangle)\tilde{u} \right.$$

$$\left. + r\langle\widetilde{uw}\rangle \frac{\partial w}{\partial r} + \langle ww\rangle \frac{\partial w}{\partial z}\right] - \frac{s_2\nu\Lambda}{\lambda^2} + L(\Lambda)$$

$$- \frac{s_3}{q}\left[\left(\frac{\partial q\Lambda}{\partial r}\right)^2 + \left(\frac{\partial q\Lambda}{\partial z}\right)^2\right] - s_4 \frac{\Lambda}{q^2}\frac{g}{\ell_o}\langle w\rho\rangle, \tag{A.14}$$

where

$$\lambda^2 = \frac{\Lambda^2}{(a + bq\Lambda/\nu)} \quad , \tag{A.15}$$

$$q^2 = \langle uu\rangle + \langle vv\rangle + \langle ww\rangle \quad , \tag{A.16}$$

$$\frac{D(\ )}{Dt} = \frac{\partial(\ )}{\partial t} + \frac{1}{r}\frac{\partial}{\partial r}\left\{r^2\tilde{u}(\ )\right\} + \frac{\partial}{\partial z}\left\{w(\ )\right\} \quad , \tag{A.17}$$

$$L(\ ) = \frac{1}{r}\frac{\partial}{\partial r}\left\{ r v_c q\Lambda \frac{\partial(\ )}{\partial r}\right\} + \frac{\partial}{\partial z}\left\{ v_c q\Lambda \frac{\partial(\ )}{\partial z}\right\} . \quad (A.18)$$

$\tilde{u}$ and w are found by solving the Poisson equation for the stream function ψ

$$\frac{\partial^2\psi}{\partial r^2} - \frac{1}{r}\frac{\partial\psi}{\partial r} + \frac{\partial^2\psi}{\partial z^2} = - r^2\tilde{\zeta} \quad , \quad (A.19)$$

where

$$\tilde{\zeta} = \frac{\partial\tilde{u}}{\partial z} - \frac{1}{r}\frac{\partial w}{\partial r} \quad , \quad (A.20)$$

$$\tilde{u} = - \frac{1}{r^2}\frac{\partial\psi}{\partial z} \qquad w = \frac{1}{r}\frac{\partial\psi}{\partial r} \quad . \quad (A.21a,b)$$

The modeling constants are assigned the values: $v_c = 0.3$; $A = 0.75$; $a = 2.5$; $b = 0.125$; $s = 1.8$; $s_1 = -0.35$; $s_2 = -0.6$ $s_3 = 0.375$ and $s_4 = 0.8$.

A.2 EQUATIONS IN CARTESIAN COORDINATES

In Cartesian coordinates, the equations for the two-dimensional WAKE calculations are written as follows:

$$\frac{D\zeta}{Dt} = - \frac{g}{\Theta_o} \frac{\partial \Theta}{\partial y} - \frac{\partial^2}{\partial z^2} \langle vw \rangle - \frac{\partial^2}{\partial y \partial z} (\langle vv \rangle - \langle ww \rangle)$$

$$+ \frac{\partial^2}{\partial y^2} \langle vw \rangle + \nu \nabla^2 \zeta \quad , \tag{A.22}$$

$$\frac{D\Theta}{Dt} = - \frac{\partial \langle v\theta \rangle}{\partial y} - \frac{\partial \langle w\theta \rangle}{\partial z} + \nu \nabla^2 \Theta \quad , \tag{A.23}$$

$$\frac{DU}{Dt} = - \frac{\partial \langle uv \rangle}{\partial y} - \frac{\partial \langle uw \rangle}{\partial z} + \nu \nabla^2 U \quad , \tag{A.24}$$

$$\frac{D\langle uu \rangle}{Dt} = - 2\langle uv \rangle \frac{\partial u}{\partial y} - 2\langle uw \rangle \frac{\partial u}{\partial z} + L(\langle uu \rangle)$$

$$- \frac{q}{\Lambda} \left(\langle uu \rangle - \frac{q^2}{3} \right) - \frac{2bq^3}{3\Lambda} \quad , \tag{A.25}$$

$$\frac{D\langle vv \rangle}{Dt} = - 2\langle vw \rangle \frac{\partial v}{\partial z} - 2\langle vv \rangle \frac{\partial v}{\partial y} + L(\langle vv \rangle)$$

$$- \frac{q}{\Lambda} \left(\langle vv \rangle - \frac{q^2}{3} \right) - \frac{2bq^3}{3\Lambda} \quad , \tag{A.26}$$

$$\frac{D\langle ww\rangle}{Dt} = -2\langle vw\rangle \frac{\partial w}{\partial y} - 2\langle ww\rangle \frac{\partial w}{\partial z} + \frac{2g}{\Theta_o}\langle w\theta\rangle$$

$$+ L(\langle ww\rangle) - \frac{q}{\Lambda}\left(\langle ww\rangle - \frac{q^2}{3}\right)$$

$$- \frac{2bq^3}{3\Lambda} \quad , \tag{A.27}$$

$$\frac{D\langle uv\rangle}{Dt} = -\langle vv\rangle \frac{\partial u}{\partial y} - \langle uv\rangle \frac{\partial v}{\partial y} - \langle vw\rangle \frac{\partial u}{\partial z}$$

$$- \langle uw\rangle \frac{\partial v}{\partial z} + L(\langle uv\rangle) - \frac{q}{\Lambda}\langle uv\rangle \quad , \tag{A.28}$$

$$\frac{D\langle uw\rangle}{Dt} = -\langle uv\rangle \frac{\partial w}{\partial y} - \langle uw\rangle \frac{\partial w}{\partial z} - \langle vw\rangle \frac{\partial u}{\partial y}$$

$$- \langle ww\rangle \frac{\partial u}{\partial z} + \frac{g}{\Theta_o}\langle u\theta\rangle + L(\langle uw\rangle)$$

$$- \frac{q}{\Lambda}\langle uw\rangle \quad , \tag{A.29}$$

$$\frac{D\langle vw\rangle}{Dt} = -\langle vv\rangle \frac{\partial w}{\partial y} - \langle ww\rangle \frac{\partial v}{\partial z} + \frac{g}{\Theta_o}\langle v\theta\rangle$$

$$+ L(\langle vw\rangle) - \frac{q}{\Lambda}\langle vw\rangle \quad , \tag{A.30}$$

$$\frac{D\langle u\theta\rangle}{Dt} = - \langle uv\rangle \frac{\partial \Theta}{\partial y} - \langle uw\rangle \frac{\partial \Theta}{\partial z} - \langle v\theta\rangle \frac{\partial u}{\partial y}$$

$$- \langle w\theta\rangle \frac{\partial u}{\partial z} + L(\langle u\theta\rangle) - \frac{Aq}{\Lambda} \langle u\theta\rangle \quad , \qquad (A.31)$$

$$\frac{D\langle v\theta\rangle}{Dt} = - \langle vv\rangle \frac{\partial \Theta}{\partial y} - \langle vw\rangle \frac{\partial \Theta}{\partial z} - \langle w\theta\rangle \frac{\partial v}{\partial z}$$

$$- \langle v\theta\rangle \frac{\partial v}{\partial y} + L(\langle v\theta\rangle) - \frac{Aq}{\Lambda} \langle v\theta\rangle \quad , \qquad (A.32)$$

$$\frac{D\langle w\theta\rangle}{Dt} = - \langle vw\rangle \frac{\partial \Theta}{\partial y} - \langle ww\rangle \frac{\partial \Theta}{\partial z} - \langle v\theta\rangle \frac{\partial w}{\partial y}$$

$$- \langle w\theta\rangle \frac{\partial w}{\partial z} + L(\langle w\theta\rangle) - \frac{Aq}{\Lambda} \langle w\theta\rangle$$

$$+ \frac{g}{\Theta_o} \langle \theta^2\rangle \quad , \qquad (A.33)$$

$$\frac{D\langle \theta^2\rangle}{Dt} = - 2\langle v\theta\rangle \frac{\partial \Theta}{\partial y} - 2\langle w\theta\rangle \frac{\partial \Theta}{\partial z} + L(\langle \theta^2\rangle)$$

$$- \frac{2bsq}{\Lambda} \langle \theta^2\rangle \quad , \qquad (A.34)$$

$$\frac{D\Lambda}{Dt} = - s_1 \frac{\Lambda}{q^2} \left[\langle uv \rangle \frac{\partial u}{\partial y} + \langle uw \rangle \frac{\partial u}{\partial z} + \langle vv \rangle \frac{\partial v}{\partial y} + \langle vw \rangle \frac{\partial v}{\partial z} + \langle vw \rangle \frac{\partial w}{\partial y} + \langle ww \rangle \frac{\partial w}{\partial z} \right] - s_2 bq + L(\Lambda) - \frac{s_3}{q} \left[\left(\frac{\partial q\Lambda}{\partial y} \right)^2 + \left(\frac{\partial q\Lambda}{\partial z} \right)^2 \right] + \frac{s_4 \Lambda}{q^2} \frac{g}{\Theta_o} \langle w\theta \rangle \quad , \tag{A.35}$$

where

$$q^2 = \langle uu \rangle + \langle vv \rangle + \langle ww \rangle \quad , \tag{A.36}$$

and

$$\frac{D(\ )}{Dt} = \frac{\partial(\ )}{\partial t} + \frac{\partial}{\partial y} [v(\ )] + \frac{\partial}{\partial z} [w(\ )] \quad , \tag{A.37}$$

$$L(\ ) = \frac{\partial}{\partial y} \left[(q\Lambda v_c + \nu) \frac{\partial(\ )}{\partial y} \right] + \frac{\partial}{\partial z} \left[(q\Lambda v_c + \nu) \frac{\partial(\ )}{\partial z} \right] . \tag{A.38}$$

v and w are found by solving the Poisson equation for ψ

$$\frac{\partial^2 \psi}{\partial y^2} + \frac{\partial^2 \psi}{\partial z^2} = - \zeta \quad , \tag{A.39}$$

with

$$v = -\frac{\partial \psi}{\partial z} \qquad w = \frac{\partial \psi}{\partial y} \quad . \tag{A.40a,b}$$

The model constants have the same value as in the axisymmetric equations.

APPENDIX B

VORTEX-RING NUMERICAL BOUNDARY CONDITIONS

In Reference 23, Bilanin et al. devised a new technique to specify computational boundary conditions when vorticity is not extensively distributed throughout an infinite two-dimensional fluid. This same technique has been employed to obtain the numerical boundary condition on the stream function for the incompressible axisymmetric case. Consider the axisymmetric vorticity distribution ζ of Figure B1 at time t. The stream function ψ is computed from

$$r \frac{\partial}{\partial r}\left(\frac{1}{r} \frac{\partial \psi}{\partial r}\right) + \frac{\partial^2 \psi}{\partial z^2} = - r\zeta(r,z,t) \quad . \tag{B.1}$$

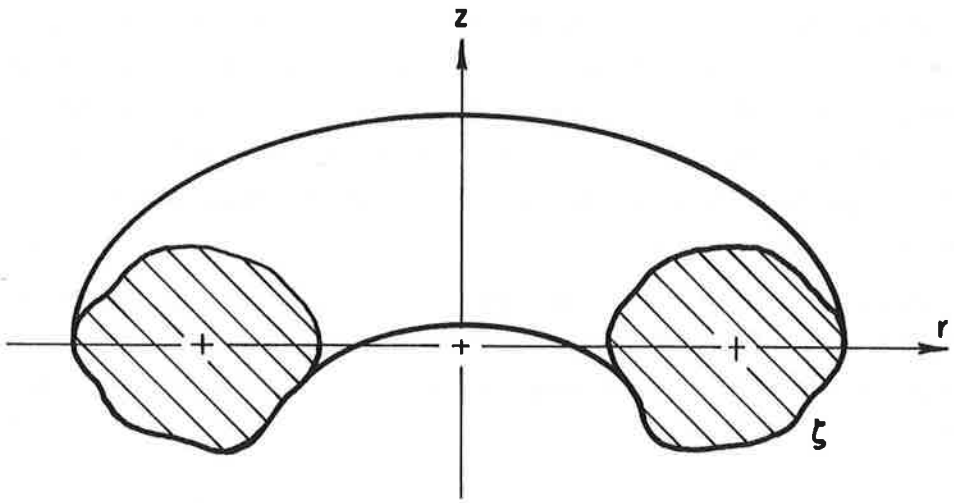

Figure B1. Representation of vorticity distribution.

The solution to this equation may be written

$$\psi(r,z,t) = \frac{r}{4\pi}\int_{-\infty}^{\infty}\int_{0}^{\infty}\int_{0}^{2\pi} \frac{\zeta(r',z',t)r'\cos\theta \; dr'dz'd\theta}{[(z-z')^2 + r^2 + r'^2 - 2rr'\cos\theta]^{\frac{1}{2}}} \quad , \tag{B.2}$$

where the denominator of the integrand is the length s between a point at (r,z) and that at (r',z), and $1/(4\pi s)$ is the appropriate Green's function. θ is the included polar angle between these points.

The radial and axial velocities are obtained from

$$v = -\frac{1}{r}\frac{\partial\psi}{\partial z} \quad , \tag{B.3a}$$

$$w = \frac{1}{r}\frac{\partial\psi}{\partial r} \quad . \tag{B.3b}$$

Although the integral defining ψ could be carried out to determine the stream function on the computational boundary, a computation grid containing JxK points would require approximately $3(J+K)/2$ integrations over three-dimensional space. This would be prohibitive in terms of computer time, and we took an alternative approach.

Selecting our numerical computational boundaries so that they are away from and surround the region containing vorticity, Eq. (B.2) may be approximated by expanding for $r >> r'$ $z >> z'$, resulting in

$$\psi(r,z,t) = \frac{R^2}{4R_s^3}\sum_{m=0}^{\infty}\sum_{n=0}^{\infty} I_{mn}G_{mn} \tag{B.4}$$

where

$$I_{mn} = \int_{-\infty}^{\infty} \int_{0}^{\infty} r'^{n+2} \, z'^{m} \, \zeta(r',z',t) dr'dz' \quad , \tag{B.5}$$

$$R_s^2 = r^2 + z^2 \quad , \tag{B.6}$$

and

$$G_{00} = 1 \quad , \tag{B.7a}$$

$$G_{01} = 0 \quad , \tag{B.7b}$$

$$G_{10} = \frac{3z}{R_s^2} \quad , \tag{B.7c}$$

$$G_{11} = 0 \quad , \tag{B.7d}$$

$$G_{02} = -\frac{3}{2r_s^2}\left[1 - \frac{5}{4}\left(\frac{r}{R}\right)^2\right] \quad , \tag{B.7e}$$

$$G_{20} = -\frac{3}{2r_s^2}\left[1 - 5\left(\frac{z}{R}\right)^2\right] \quad , \tag{B.7f}$$

$$\cdots \quad .$$

The integers m and n must be sufficiently large to give the desired resolution of the farfield. Our work in two-dimensional vortex flows suggests that n and m need be no larger than 2. Since the velocity decreases as the inverse of r in two-dimensional flow, while decreasing as r^{-3} in the axisymmetric case, the accuracy of the expansion for the latter case will be greater at any given value of R_s for m and n equal to 2.

Given this approximation for the stream function, it is possible to develop a farfield density to supply boundary conditions for a linearly stratified flow. Since the vortex ring

perturbs the density field, the inflow density at z_- is not precisely a linear function of z. In steady-flow coordinates the velocity along streamlines is reduced below the self-induced ring velocity, V, and approaches V as $R_2 \to \infty$. Referring to Figure B2,

$$\frac{\Delta z}{dt} = V - w \quad , \tag{B.8}$$

and

$$\frac{d\Delta z}{dz} = \frac{d\Delta z}{dt}\Big/\frac{dz}{dt} = 1 - \frac{w}{V} \quad , \tag{B.9}$$

to first order in w/V for $w/V \simeq 1$. Then

$$\Delta z = \int_{-\infty}^{z} \left(1 - \frac{w}{V}\right) dz \quad . \tag{B.10}$$

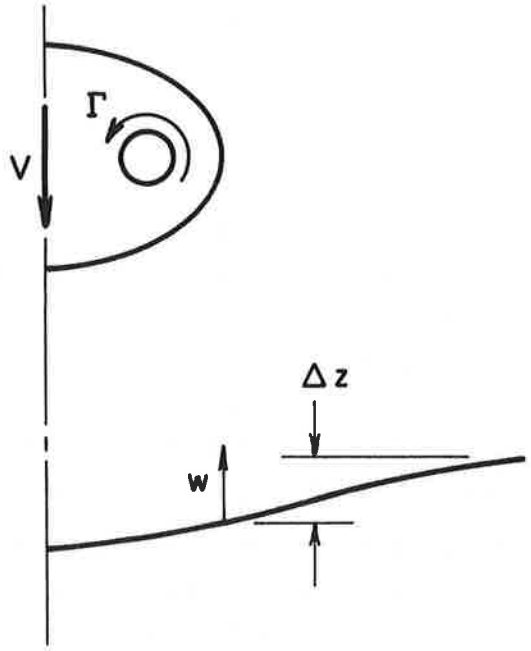

Figure B2. Effect of descending vortex ring on isopycnals.

For a linear stratification,

$$\Delta\rho = \Delta z \frac{d\rho_o}{dz} \quad . \tag{B.11}$$

Normalizing $\Delta\rho$ by $R_o\frac{d\rho_o}{dz}$, and z by R_o gives

$$\Delta\rho = \int_{-\infty}^{z} \left[1 - \frac{w}{V}\right] dz \quad . \tag{B.12}$$

w is given by

$$w = \frac{1}{r}\frac{\partial\psi}{\partial r} \quad , \tag{B.13}$$

and therefore,

$$\Delta\rho = -\frac{1}{Vr}\int_{-\infty}^{\infty}\frac{\partial\psi}{\partial r}\, dz \quad , \tag{B.14}$$

and using Eq. (B.4),

$$\Delta\rho = \sum_{m=0}^{\infty}\sum_{n=0}^{\infty}\frac{I_{mn}}{vr}\int_{-\infty}^{z}\frac{\partial G_{mn}}{\partial r}\, dz \quad . \tag{B.15}$$

If we write this as

$$\Delta\rho = \sum_{m=0}^{\infty}\sum_{n=0}^{\infty}\frac{I_{mn}}{v} H_{mn} \quad , \tag{B.16}$$

the functions H_{mn} for m and n up to 2 are given by

$$H_{00} = \frac{z}{4R_s^3} \quad , \tag{B.17a}$$

$$H_{01} = 0 \quad , \tag{B.17b}$$

$$H_{10} = \frac{(2z^2-r)}{4R_s^3} \quad , \tag{B.17c}$$

$$H_{11} = 0 \quad , \tag{B.17d}$$

$$H_{02} = \frac{15z}{32R_s^7} \quad , \tag{B.17e}$$

$$H_{20} = \frac{3z(2z^2-3r^2)}{8R_s^7} \quad . \tag{B.17f}$$

APPENDIX C
REPORT OF NEW TECHNOLOGY

The work under this contract has contributed to increased understanding of aircraft wake vortex behavior in stable stratification, as well as to providing confidence in numerical simulation techniques in the prediction of turbulent vortex pairs and vortex rings in stratified fluids.

APPENDIX D

REFERENCES

1. Bliss, D.B.: "The Dynamics of Curved Rotational Vortex Lines," M.S. Thesis, MIT, Cambridge MA, 1970.

2. Saffman, P.G.: "The Velocity of Viscous Vortex Rings," *Stud. in Appl. Math.*, Vol. XLIX, No. 4, pp. 371-380, December 1970.

3. Fraenkel, L.E.: "On Steady Vortex Rings of Small Cross Section in an Ideal Fluid," *Proc. Roy. Soc.*, Ser. A, Vol. 316, pp. 29-62, 1970.

4. Widnall, S.E.: "The Structure and Dynamics of Vortex Filaments," *Ann. Rev. of Fluid Mech.*, Vol. 7, pp. 141-165, 1975.

5. Costen, R.C.: "Drift of Buoyant Wing-Tip Vortices," *J. of Aircraft*, Vol. 9, No. 6, pp. 406-412, June 1972.

6. Kuhn, G.D. and J.N. Nielsen: "Analytical Studies of Aircraft Trailing Vortices," AIAA Paper 72-42, 1972.

7. Saffman, P.G.: "The Motion of a Vortex Pair in a Stratified Atmosphere," *Stud. in Appl. Math.*, Vol. II, No. 2, pp. 107-119, June 1972.

8. Scorer, R.S. and L.J. Davenport: "Contrails and Aircraft Downwash," *J. Fluid Mech.*, Vol. 43, part 3, pp. 451-464, 1970.

9. Tombach, I.H.: "Transport of a Vortex Wake in A Stably Stratified Atmosphere," *Aircraft Wake Turbulence and its Detection*, Plenum Press, New York, pp. 41-56, 1971.

10. Tulin, M.P. and J. Shwartz: "The Motion of Turbulent Vortex Pairs in Homogeneous and Density Stratified Media," Hydronautics, Inc. Technical Report No. 231-15, AD 723-184, 1971.

11. Crow, S.C.: "Motion of a Vortex Pair in a Stably Stratified Fluid," Poseidon Research Report No. 1, May 1974.

12. Narain, J.P. and M.S. Uberoi: "The Motion of a Trailing Vortex Wake in a Stratified Medium," *Atmospheric Environment*, Vol 8, pp. 459-473, 1974.

13. Bilanin, A.J., J.E. Hirsh, M.E. Teske, and A.M. Hecht: "Atmospheric-Wake Vortex Interaction," NASA Report No. 145336, A.R.A.P. Report No. 331, April 1978.

14. Turner, J.S.: "A Comparison Between Buoyant Vortex Rings and Vortex Pairs," *J. Fluid Mech.*, Vol. 7, part 3, pp. 419-432, 1960.

15. Linden, P.F.: "The Interaction of a Vortex Ring With a Sharp Density Interface: A Model for Turbulent Entrainment," *J. Fluid Mech.*, Vol. 60, part 3, pp. 467-480, 1973

16. Maxworthy, T.: "Some Experimental Studies of Vortex Rings," *J. Fluid Mech.*, Vol. 81, part 3, pp. 465-495, 1977.

17. Maxworthy, T.: "The Structure and Stability of Vortex Rings," *J. Fluid Mech.*, Vol. 51, part 1, pp. 15-32, 1972.

18. Maxworthy, T.: "Turbulent Vortex Rings," *J. Fluid Mech.*, Vol. 64, Part 2, pp. 227-239, 1974.

19. Donaldson, C.duP.: "Atmospheric Turbulence and Dispersal of Atmospheric Pollutants," *Proceedings of the Workshop on Micrometerology*, (D.A. Haugen, Ed.). Am. Meteor. Soc. Science Press, pp. 313-390, 1973.

20. Lewellen, W.S.: "Use of Invariant Modeling," *Handbook of Turbulence*, Plenum Press, pp. 237-280, 1977. See also Lewellen, W.S. and Teske, M.E.: "Turbulence Modeling and its Application to Atmospheric Diffusion," EPA-600/4-75-016b, 1976.

21. Lewellen, W.S., M.E. Teske, and C. duP. Donaldson: "Variable Density Flows Computed by a Second-Order Closure Description of Turbulence," *AIAA J.*, Vol. 14, pp. 382-387, 1976.

22. Lewellen, W.S., M.E. Teske, and C. duP. Donaldson: "Turbulent Wakes in a Stratified Fluid - Part I: Model Development, Verification and Sensitivity to Initial Conditions," A.R.A.P. Report No. 22, August 1974.

23. Bilanin, A.J., M.E. Teske, and G.G. Williamson: "Vortex Interaction and Decay in Aircraft Wakes," *AIAA J.*, Vol. 15, No. 2, pp. 250-260, 1977.

24. Bilanin, A.J., M.E. Teske, and J.E. Hirsh: "Neutral Atmospheric Effects on the Dissipation of Aircraft Vortex Wakes," *AIAA J.*, Vol. 16, No. 9, pp. 956-961, 1978.

25. Lewellen, W.S. and M.E. Teske: "Turbulent Transport Model of Low-Level Winds in a Tornado," presented at the 10th American Meteorological Society Conference on Severe Local Storms, Denver, October 1977.

26. Oster, G.: "Density Gradients," *Sci. Am.*, Vol. 213, No. 2, pp. 70-76, 1965.

27. Boris, J.P. and D.L. Book: "Flux-Corrected Transport III. Minimal-Error FCT Algorithms," *J. of Comput. Phys.*, Vol. 20, pp. 397-431, 1976.

28. Swartztrauber, P. and R. Sweet: "Efficient Fortran Subprograms of Elliptic Partial Differential Equations," NCAR-TN/IA-109, 1976.

29. Arakawa, A.: "Numerical Simulation of Large Scale Atmospheric Motions in Numerical Solution of Field Problems in Continuum Physics," *SIAM-AMS Proc.*, Vol. II, pp. 24-40, 1970.

30. Burnham, D.C., J.N. Hallock, I.H. Tombach, M.R. Brashears, and M.R. Barber: "Ground-Based Measurements of the Wake Vortex Characteristics of a B-747 Aircraft in Various Configurations," Report No. FAA-RD-78-146, December 1978.

31. Hoffmann, E.R., and P.N. Joubert: "Turbulent Line Vortices," *J. of Fluid Mech.*, Vol. 16, Part 3, pp. 395-411, July 1963.

32. Sheng, Y.P., H. Segur, and W.S. Lewellen: "Application of a Spatial Smoothing Scheme to Control Short-wave Numerical Oscillations, Aeronautical Research Associates of Princeton, Inc., Tech. Memo. No. 78-8, October 1978.

250 copies

U.S. DEPARTMENT OF TRANSPORTATION
RESEARCH AND SPECIAL PROGRAMS ADMINISTRATION
TRANSPORTATION SYSTEMS CENTER
KENDALL SQUARE, CAMBRIDGE, MA. 02142

OFFICIAL BUSINESS
PENALTY FOR PRIVATE USE, $300

POSTAGE AND FEES PAID
U.S. DEPARTMENT OF TRANSPORTATION
513